CNR-INFM Research Center on Bose-Einstein Condensation
Università degli Studi di Trento

Tesi di Dottorato di Ricerca in Fisica

Fermi Mixtures: Effects of Engineered Confinements

Ingrid Bausmerth

Supervisors
Prof. Sandro Stringari
Dr. Alessio Recati

Referees
Prof. Frédéric Chevy
Dr. Stefano Giorgini
Dr. Andrea Trombettoni

November 2009

On ne reçoit pas la sagesse, il faut la découvrir soi-même après un trajet que personne ne peut faire pour nous, ne peut nous épargner, car elle est un point de vue sur les choses.

A la recherche du temps perdu

Marcel Proust

This thesis is based on the following work

- **Destroying Superfluidity by Rotating a Fermi Gas at Unitarity**

  I. Bausmerth, A. Recati, S. Stringari

  Physical Review Letters **100**, 070401 (2008)

- **Unitary Fermi Gas under Adiabatic Rotation**

  I. Bausmerth, A. Recati, S. Stringari

  Physical Review A **78**, 063603 (2008)

- **Chandrasekhar-Clogston limit and Phase Separation in Fermi Mixtures at Unitarity**

  I. Bausmerth, A. Recati, S. Stringari

  Physical Review A **79**, 043622 (2009)

Contents

1 Introduction

The major breakthrough in the research of ultracold atomic quantum gases was in 1995, when experimentalists for the first time were able to cool a dilute vapor of alkali-metal atoms to such low temperatures that a Bose-Einstein condensate (BEC) [1–3] could be observed. In Fig. 1.1 (a) we report the characteristic absorption image of a cloud of bosonic atoms undergoing the BEC transition.

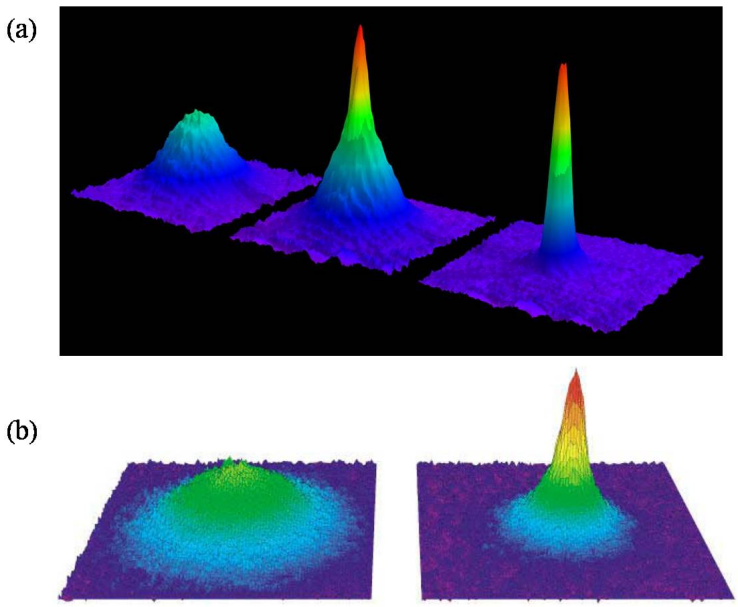

Figure 1.1: (a) Absorption image of Bose-Einstein condensate of $\sim 7 \times 10^5$ sodium atoms. Shown is absorption vs. two spatial dimensions. The Bose-Einstein condensate is characterized by its slow expansion observed after 6 msec time-of-flight. The left picture shows an expanding cloud cooled to just above the transition point; middle: just after the condensate appeared; right: after further evaporative cooling has left an almost pure condensate. The temperature T_c at the transition point is 2 μK [4]. (b) Time-of-flight absorption image of a molecular Bose-Einstein condensate of ^{6}Li atoms. The distribution shows the characteristic peak around zero momentum, hence the bimodal momentum distribution of a condensate plus a thermal cloud [5, 6].

This achievement together with the tunability of the interaction between atoms via Fano-Feshbach resonances [7–9] and the inclusion of optical lattices triggered

an impressive amount of experimental and theoretical work in the field of Bose-Einstein condensates or, more generally, in the field of cold gases [4, 10–13]. The lines of research go from the studies of superfluid features such as quantized vortices [14–16] and the hydrodynamic nature of collective modes [17, 18], to Josephson-like effects [19, 20] and the observation of interferences of coherent matter waves [21], to realizing the superfluid to Mott-insulator transition [22] in these ultracold atomic quantum systems, just to name a few.

The possibility to Bose-condense a gas, a procedure which previously seemed inaccessible, spawned the quest for ultracold Fermi gases, and entailed the realization of the first degenerate trapped Fermi gas in 1999 [23].

Although the relevant temperature scale to achieve quantum degeneracy for both bosons and fermions is of the order of $T_{deg} \propto n^{2/3}$, where n is the gas density, quantum statistics give rise to a significantly different behaviour at the degeneracy temperature. While bosonic gases such as ^{87}Rb or ^{7}Li undergo the phase transition to a Bose-Einstein condensate, a noninteracting Fermi gas of e.g. ^{6}Li or ^{40}K atoms exhibits a smooth crossover between a classical and a quantum behaviour.

In rarefied and ultracold gases only two-body collisions at low energy are relevant. The main contribution to the interparticle scattering comes from states with an $\ell = 0$ component of the angular momentum, i.e. the s-wave states (see, e.g., [24]). Interactions in these cold systems are hence characterized by a single parameter, the s-wave scattering length a_s, which is independent of the details of the two-body potential [10, 11, 25, 26].

In systems of identical fermions however s-wave scattering is excluded due to the asymmetry of the wave function, and since p-wave interaction ($\ell = 1$) is very weak, polarized fermions can interact only if they are in different spin states.

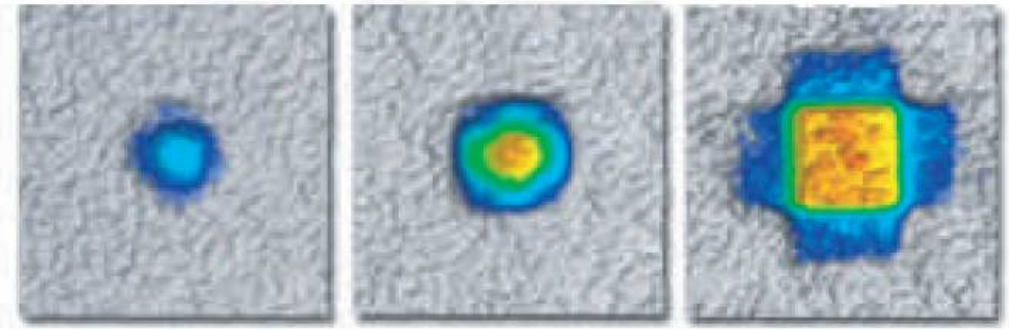

Figure 1.2: Fermi surfaces imaged by time-of-flight of an ultracold Fermi gas of ^{40}K atoms released from a 3D optical lattice potential for increasing filling factors corresponding to different Fermi energies, see [27] and references therein.

Polarized and hence non-interacting Fermi gases at zero temperature in three

dimensional periodic potentials make it possible to study the Fermi surface (Fig. 1.2) and the momentum distribution of ideal Fermi gases at zero temperature [28], as well as quantum phenomena related to solid state physics such as Bloch waves [29] and Bloch oscillations [30] in one dimensional optical lattices. The advantage of polarized Fermi gases in these experiments lies in the fact that due to the Pauli principle in the absence of s-wave collisions damping and instabilities are prevented, making the observations of long-living oscillations possible.

To have a finite s-wave interaction between the fermions, they need to be in different spin states, which experimentally is achieved in mixtures of different atomic species or transferring the fermions into different hyperfine levels.

Indeed, a great appeal of ultracold gases lies in the fact that the s-wave scattering length can be changed by means of an external magnetic field, in the presence of Feshbach resonances, from negative to positive values, and consequently the interactions between particles can be controllably tuned [31].

For instance, fermions with repulsive interactions in optical lattices are a powerful tool to investigate solid state models such as the Hubbard hamiltonian [32], which was initially proposed to study electrons in solids, and to locate different phases such as the antiferromagnetic and the superfluid ones [33, 34]. Fermionic quantum gases therefore can be used to simulate condensed matter configurations and give the possibility to understand the physics of strongly correlated systems. The tunability of the lattice potential allows to observe the Mott insulator state [35], a model which was originally introduced to describe the transition from a metal to an insulator [36].

On the other hand, if the interaction is attractive, the system at low temperature is a superfluid. Depending on the strength of the interaction, we can have different regimes. When the scattering length is small and positive two fermions with spin-up and spin-down form a molecule, whose size is much smaller than the interparticle distance (see Fig. 1.3). This gas of weakly repulsive molecules undergoes the usual BEC phase transition [5, 37–40] to a "molecular condensate"[5, 6, 38], exhibiting the typical bimodal distribution as shown in Fig. 1.1 (b).

For small negative values of the scattering length one has a transition to the so-called Bardeen Copper Schrieffer (BCS) superfluid [41]. The fermions form long-range Cooper pairs [42], whose size is much bigger than the interparticle distance (see Fig. 1.3).

The most interesting physics occurs in the so-called unitary regime, where the scattering length a_s diverges, and the interparticle distance, of the order of $1/k_{\mathrm{F}}$, is the only length scale. The system is strongly correlated and its properties do not depend neither on the value, nor on the sign of a_s. The system exhibits an universal behaviour, being dilute but strongly interacting, since all length scales disappear from the calculation of thermodynamic functions. The transition from

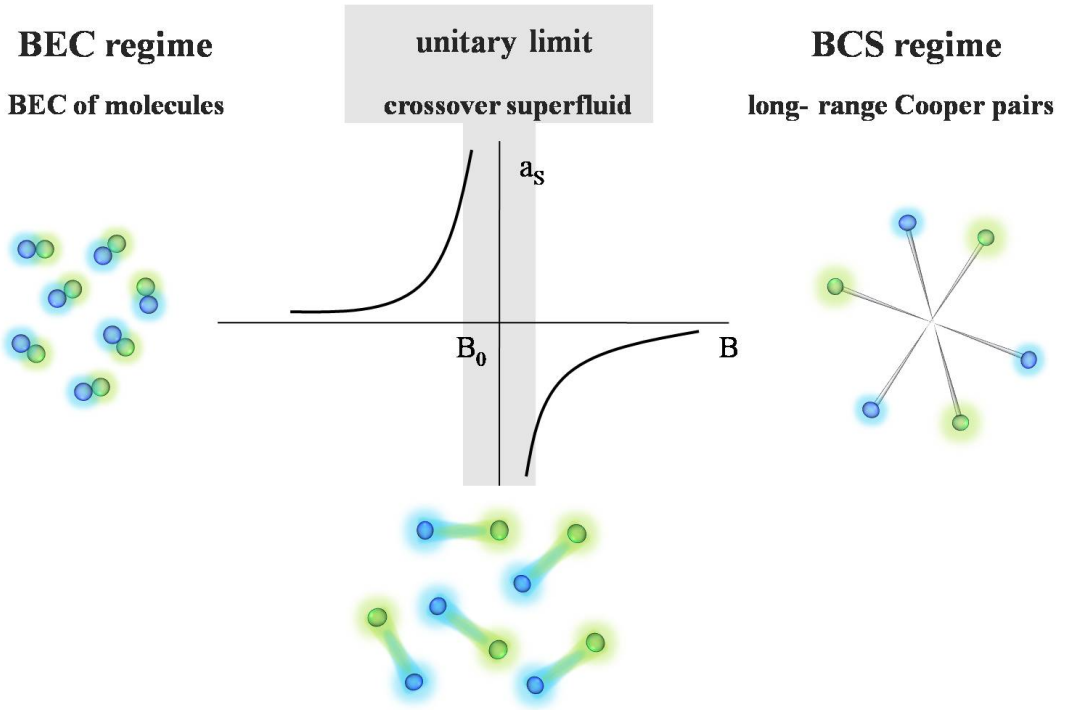

Figure 1.3: The BEC-BCS crossover. Interatomic interaction strength can be widely varied with a magnetic Feshbach resonance. In highly dilute and ultra cold systems the low energy collisions between two particles are characterized by the s-wave scattering length a_s. For $a_s > 0$ on the BEC side the fermions form tightly bound molecules. Close to the resonance, also called the unitary limit, the interaction is very strong and a_s diverges. For $a_s < 0$ on the BCS side of the resonance the fermions form Cooper pairs.

the BEC to the BCS state is smooth at zero temperature, and the system is expected to be superfluid along the entire BEC-BCS crossover.

A crucial test of the superfluidity of a system is its response to rotation, i.e. its moment of inertia [11]. Due to its macroscopic wave function, a superfluid adapts to the rotation differently than a normal fluid [43, 44]. Under strong rotation, flow in form of quantized vortices enters the system, and one can observe the formation of vortex lattices [16].

By smoothly varying the scattering length from negative to positive values of a rotating gas of ^{6}Li, in 2005 experimenters [45] were able to image vortex lattices in as shown in Fig. 1.4. This observation provided the first evidence of the superfluid behaviour of ultracold fermionic gases along the crossover. In these experiments, vortices are produced by spinning the condensate with a laser beam. The vortices are observed by releasing the atomic cloud of molecules, stabilizing and making them visible through a rapid sweep of the scattering length to small and positive values, i.e. to the BEC regime.

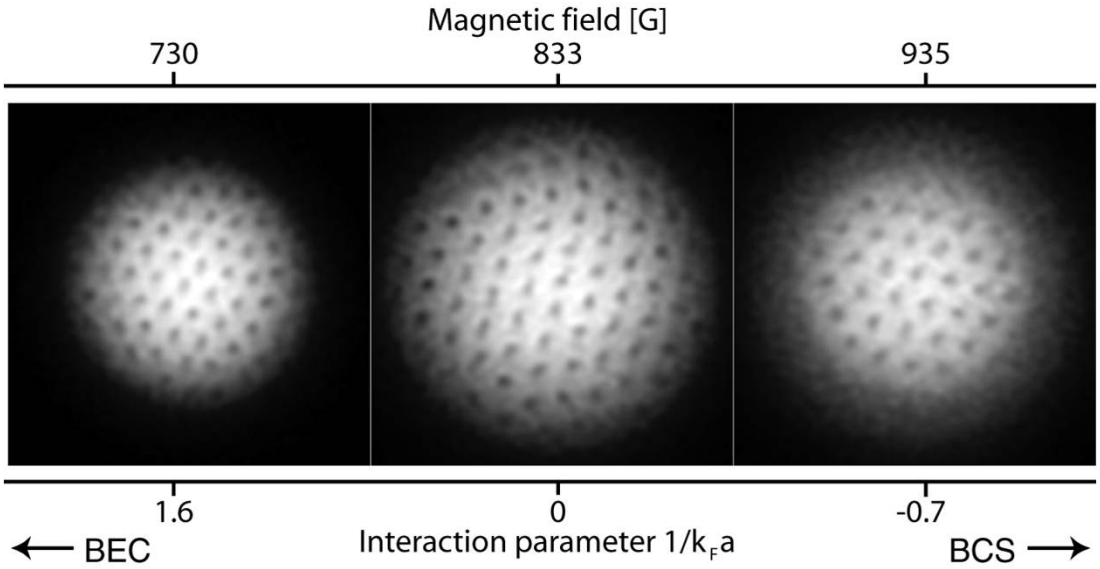

Figure 1.4: Absorption images of vortex lattices in ^{6}Li [45] for a molecular Bose-Einstein condensate (left), for a unitary superfluid (center) and a BCS superfluid (right).

The ability to not only control the interaction between the particles but also the atom numbers in the different spin states opened the path to the realization of more complex configurations [45–48]. Soon fermionic superfluidity with imbalanced spin-populations [49] was realised. It became possible to directly observe the superfluid phase transition in polarized Fermi gases [50] as well as to measure the Chandrasekhar-Clogston (CC) limit which corresponds to the maximal imbalance in the spin states above which superfluidity disappears. This limit was first introduced 1962 by Clogston [51] and independently by Chandrasekhar [52] in the context of superconductivity, where it represents the upper limit for a magnetic field, beyond which superconductivity will break down.

From the theoretical point of view, the balanced system can be described with reasonably good approximation along the entire BEC-BCS crossover solving the BCS mean field equations, i.e. the gap and number equations. This approach was first introduced by Eagels [53] and Leggett [54] to investigate the superconducting and superfluid properties of matter beyond the weak coupling limit.

In the BEC limit BCS mean-field theory correctly predicts the formation of dimers, however with a wrong value for the dimer-dimer scattering length. The problem of two colliding composite bosons was later solved by Petrov *et al.* [55] using the zero-range approximation, and the effective scattering length between two dimers was found to be $a_{dd} \simeq 0.60 a_s$, where a_s is the atom-atom scattering length.

A major difficulty is encountered at unitarity, where BCS mean-field theory is known to give reasonable predictions in the case of unpolarized configurations

(see, for example, [26]). However, it fails to give quantitatively correct results in the imbalanced case and to predict correctly the Chandrasekhar-Clogston limit of critical polarization (see chapter 3). This failure is mainly due to the fact that, within BCS theory, the energy of the normal state at unitarity is just the sum of the kinetic energies of the spin-up and spin-down components and hence interactions in the normal phase are ignored. Naively, the reason is because BCS theory treats the interaction as a perturbation, where the interaction is simply proportional to the scattering length, which diverges at unitarity.

Recent theoretical efforts have been focused on the correct inclusion of interactions [56–62] in order to describe the polarized Fermi gas and the normal to superfluid transition as observed in experiments [46–50, 63, 64]. Also numerical techniques, as e.g. fixed-node diffusion Monte Carlo (FN-DMC) [65], have been used to investigate the ground-state properties for the BEC-BCS crossover and of the polarized Fermi gas at unitarity and at zero temperature (see, e.g., [26] and references therein).

The experiments on polarized Fermi gases can be explained by using the theory of Lobo *et al.* [59] (see chapter 3). The authors suggest that, at unitarity and at zero temperature, the highly polarized system can be treated as a normal Fermi liquid, where weakly interacting quasi particles associated with the minority atoms interact with the majority particles. The theory is in very good agreement with the experimental findings of the MIT group [50]. The calculations have proven to be very efficient not only in reproducing the experimental value of the Chandrasekhar-Clogston limit $x_c = 0.44$, but also the density profiles of the two separate spin components as shown in Fig. 1.5 [60].

The recent observation of heteronuclear Feshbach resonances in ultracold mixtures of two different fermionic species [66] as well as the realization of degenerate configurations [67] opened new stimulating perspectives in the field of Fermi superfluids built with atomic species of different masses. The appeal of mass and population imbalanced mixtures lies in the fact that on one hand they can mimic physical models as, e.g., color superconductivity in dense quark matter (high density QCD, [68, 69]), and on the other hand they pave the route towards new exotic pairing phases.

The phase diagram of Fermi mixtures with unequal masses and the corresponding polarization effects, including the possible occurrence of the Fulde-Ferrell-Larkin-Ovchinnikov (FFLO) phase [70], have already been the object of many theoretical predictions based on BCS mean-field theory [71–77]. Monte Carlo calculations were recently employed to investigate fermion pairing in the unitary regime for a mass ratio corresponding to a ^{6}Li-^{40}K mixture [78] and to predict the Chandrasekhar-Clogston limit as a function of the mass ratio as well as the density profiles of the harmonically trapped system.

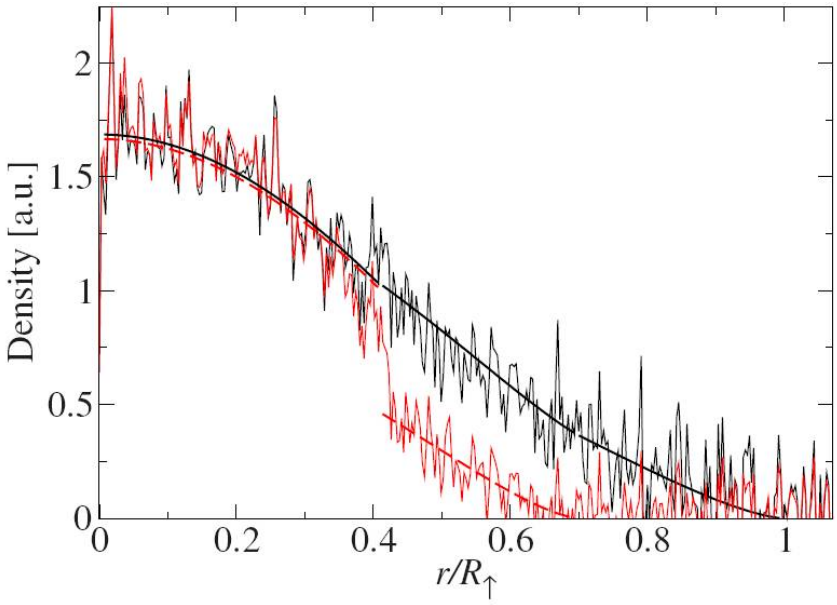

Figure 1.5: Density profiles for a polarization $P = 0.44$. Theory: Solid black line (dashed red line) is the spin-↑ (spin-↓) density. Experiment: The black (red) line is the spin-↑ (spin-↓) density as reported in [63]. The density jump in the ↓ component is clearly visible. From [60].

In this thesis we first review in chapter 2 the theory of the normal state of the unitary Fermi gas at $T = 0$ as discussed in [59, 60] and the main properties of the normal-to-superfluid transition.

In chapter 3 we study the trapped gas under adiabatic rotation, i.e., avoiding the formation of vortices. We show that for polarized systems the rotation enhances the Chandrasekhar-Clogston limit due to pair breaking at the border between the superfluid and the normal phase, while it leaves the global critical polarization P_c of the trapped system unaffected [79]. In the case of an unpolarized unitary superfluid the rotation causes a phase separation between a superfluid core and an unpolarized normal shell, in which the densities of the ↑ and ↓ atom numbers is equal [80]. For both the polarized and the unpolarized systems we calculate experimental observables such as the density profiles and the angular momenta.

From the study of Bose-Einstein condensates it is well known that an adiabatic rotation induces a quadrupole deformation of the trapped atomic cloud when the rotation exceeds a certain angular velocity. In Fermi gases the situation is different due to the phase separation discussed above, and the quadrupole instabilities are found to set on at smaller angular velocity than in the BEC case [80]. This phenomenon together with a more general discussion concerning not only the energetic but also the dynamic instabilities of the phase separated system is presented in chapter 4.

The main goal of chapter 5 is to use the present knowledge of the equation of

state of Fermi mixtures with unequal masses to give quantitative predictions for the phase separation between the normal and superfluid components. The analysis is based on the study of the zero temperature μ-h phase diagram of the uniform two component gas, where $\mu = (\mu_\uparrow + \mu_\downarrow)/2$ is the chemical potential and $h = (\mu_\uparrow - \mu_\downarrow)/2$ is an effective magnetic field. The phase diagram at unitarity is determined thanks to the knowledge of the equation of state available from diagrammatic techniques applied to highly polarized configurations and from Monte Carlo simulations. The phase diagram is then used, in the local density approximation, to calculate the density profiles of the two Fermi components in the presence of harmonic trapping.

In chapter 6 we investigate the polarization produced by the relative displacement of the potentials trapping two spin species of a unitary Fermi gas with population imbalance. We investigate the dipole polarizability of a polarized system both in the two-fluid and the three-fluid model at zero temperature and point out the major differences between the two treatments.

In chapter 7 we eventually draw our conclusions.

2 The Unitary Fermi Gas

The study of polarization effects in Fermi superfluids has been the object of intense experimental and theoretical work (for recent reviews on the subject see, e.g., [26, 81]). Recent experiments with harmonically trapped configurations [45–48, 50, 63] have shown that a polarized Fermi gas at unitarity and zero temperature undergoes a phase separation between a central core of an unpolarized superfluid and an external shell of a polarized normal gas. In a trap the relevant parameter for imbalanced systems at $T = 0$ is the polarization

$$P = \frac{N_\uparrow - N_\downarrow}{N_\uparrow + N_\downarrow}, \tag{2.1}$$

where $N_\uparrow$ is the number of particles in the spin-up state, and $N_\downarrow$ is the number in the spin-down state, respectively.

Experiments, where surface tension effects are not important and the local density approximation is applicable (see, e.g., [50, 63]), have revealed the occurrence of a critical value of the total polarization $P_c \simeq 0.77$ of the gas above which the superfluid core disappears.

In [59, 60] the equations of state of uniform matter for the superfluid and for the polarized normal phases, calculated with *ab initio* Monte Carlo simulations, have been employed within a local density approximation to treat the effect of the harmonic trapping in the unitary regime [61]. These calculations were proven to be very efficient not only in reproducing the experimental value of the critical polarization, but also the density profiles of the two separate spin components. Therefore they provide an accurate and consistent description of the phase separation exhibited by the unitary Fermi gas at zero temperature. In particular, the discontinuity characterizing the spin-down density at the interface between the superfluid and normal components, as well as the typical knee revealed by the column density of the same spin-down component, are dramatic features reproduced with accuracy by theory. These calculations have pointed out the crucial role played by the interactions in the normal phase [60].

Here and in the following we will review the physics of dilute mixtures of spin-$\uparrow$ and spin-$\downarrow$ fermions at zero temperature and at unitarity, i.e. when the scattering

length, characterizing the interaction between the particles, is much bigger than the interparticle distance [59, 60]. In this limit, the system can be regarded as a strongly interacting fluid, and one of the fascinating phenomena occurring is the phase separation between an unpolarized superfluid and a partially polarized normal gas.

2.1 The Equation of State of the Unitary Fermi Superfluid

At unitarity and zero temperature all thermodynamic quantities are universal functions of $E_{\mathrm{F}} = (\hbar^2/2m)(6\pi^2 n)^{2/3}$. Hence the equation of state of a fully polarized Fermi gas, at unitarity and zero temperature, is given by the equation of state of the *ideal* Fermi gas $\mu(n) = (6\pi^2)^{2/3}(\hbar^2/2m)n^{2/3}$. In the case of interactions, the equation of state has the same density dependence as the ideal gas, apart from a dimensionless normalisation factor $(1+\beta)$, which accounts for interactions in the system.

In the case of an unpolarized superfluid state, $N_\uparrow = N_\downarrow$, the equation of state is given by

$$\frac{E_{\mathrm{S}}}{N_{\mathrm{S}}} = \frac{3}{5}E_F(1+\beta), \tag{2.2}$$

where E_{S} is the total energy of the system, and N_{S} is the total number of particles. The value of the dimensionless factor $\beta = -0.58$ has been calculated employing Monte Carlo simulations [82, 83]. Eventually, the equation of state of the unpolarized superfluid state is given by

$$\frac{E_{\mathrm{S}}}{N_{\mathrm{S}}} = \xi_{\mathrm{S}}\frac{3}{5}\frac{\hbar^2}{2m}(6\pi^2 n_{\mathrm{S}})^{2/3} \equiv \epsilon_{\mathrm{S}}(n_{\mathrm{S}}), \tag{2.3}$$

where $\xi_{\mathrm{S}} \equiv (1+\beta) = 0.42$.

2.2 The Equation of State of the Unitary Fermi Gas

In contrast to the superfluid, the normal phase is polarized, $N_\uparrow \neq N_\downarrow$, and therefore its equation of state must depend on the concentration

$$x = \frac{N_\downarrow}{N_\uparrow}, \tag{2.4}$$

where $x \leq 1$.

The equation of state of the unitary Fermi gas at zero temperature was derived in the spirit of a longstanding subject in condensed matter physics, namely the problem of a single impurity interacting with its environment. Related examples are the moving electron in a crystal lattice, the lattice *polaron* [1], or a magnetic impurity in a sea of electrons known as the Kondo problem [85].

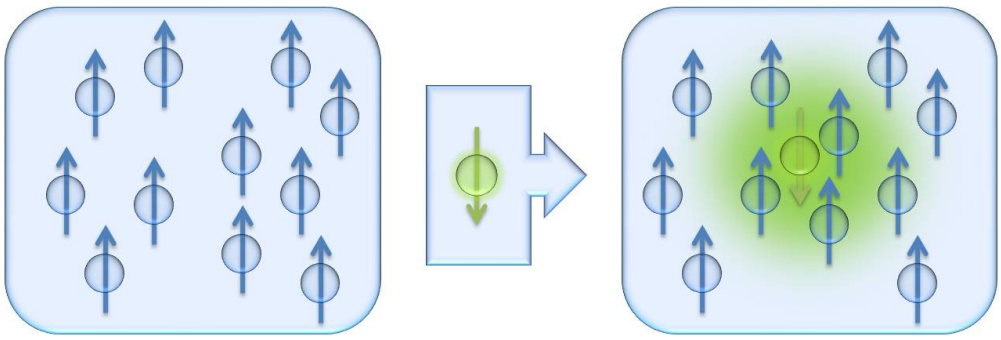

Figure 2.1: Left panel: Nonperturbed sea of ↑-particles. Left panel: spin-↓ impurity immersed in the Fermi sea of spin-↑ atoms; due to the interactions it becomes a quasiparticle, an impurity dressed by particle-hole excitations, resulting in a Fermi polaron with an effective mass and energy.

In our case the impurity is a spin-↓ atom immersed in a spin-↑ sea, which becomes "coated"or "dressed"by the interaction with the spin-↑ particles. As a consequence, the impurity loses its identity as a bare spin-↓ particle and becomes a quasiparticle with an effective mass and energy, a Fermi polaron [86, 87].

The equation of state at unitarity was first derived by Lobo *et al.* [59] assuming that the partially polarized phase is a dilute mixture which is created by adding a few spin-↓ particles to a noninteracting gas of spin-↑ atoms.

In a small x expansion the energy of the normal state can be written as [59, 60]

$$\frac{E_{\mathrm{N}}(x)}{N_\uparrow} = \frac{3}{5}E_{F\uparrow}\left(1 - Ax + \frac{m}{m^*}x^{5/3} + Bx^2\right) = \frac{3}{5}E_{F\uparrow}g(x) \equiv \epsilon_{\mathrm{N}}(x), \tag{2.5}$$

where $N_\uparrow$ is the total number of spin-↑ atoms and $E_{F\uparrow} = \hbar^2/2m(6\pi^2 n_\uparrow)^{2/3}$ the Fermi energy of the spin-↑ gas. The first term in Eq.(2.5) corresponds to the energy per particle of the noninteracting ↑-gas, while the term linear in x gives the binding energy A of the spin-↓ particles to the spin-↑ sea. In Eq.(2.5) it is assumed that adding spin-↓ particles to the spin-↑ sea, the ↓-atoms form a Fermi gas of quasiparticles or Fermi polarons with an effective mass m^*, and contribute to the total energy by the quantum pressure term proportional to $x^{5/3}$.

[1] The term *polaron* was first used by Landau [84] to describe an electron, which by moving through a crystal lattice polarizes the ions. This brings the ions out of their equilibrium and distorts the lattice, creating phonons which "dress" the electron.

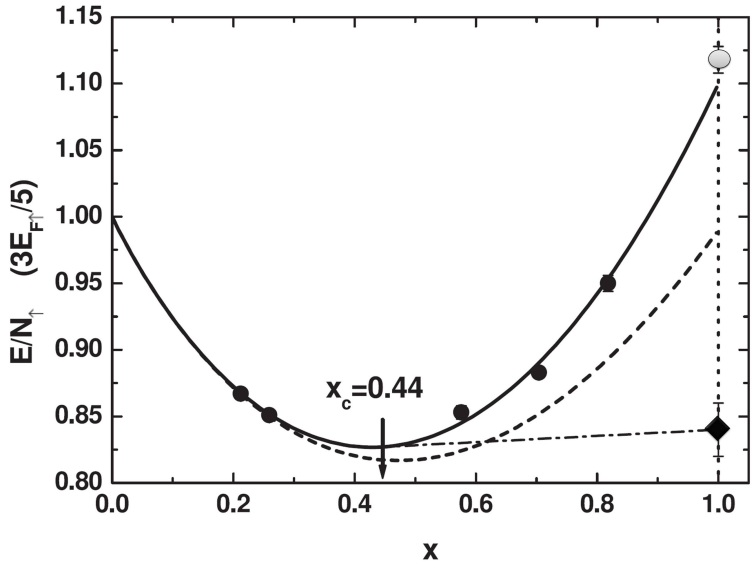

Figure 2.2: Equation of state of a normal Fermi gas as a function of the concentration x (circles). The solid line is a polynomial best fit to the Monte Carlo results. The dashed line corresponds to expansion (2.5). The dot-dashed line is the coexistence line between the normal and the unpolarized superfluid states, and the arrow indicates the critical concentration x_c above which the system phase separates. For $x = 1$, the energy of both the normal (white dot) and the superfluid (black diamond) states are shown, [59].

The values of the binding energy A and of the effective mass m^* have been calculated using different many-body methods, e.g. Quantum Monte Carlo Methods and the T-matrix approach [59, 65, 88–91]. The most recent Monte Carlo calculations give $A = 0.99(1)$ and $m^*/m = 1.09(2)$ [65].

Eventually, the last term proportional to x^2 includes the effect of interactions between the quasiparticles. It has has been estimated fitting the expression (2.5) to the Monte Carlo results for the equation of state as a function of the concentration, and the parameter $B = 0.14$ accounting for these interactions has been calculated in [65]. The parametrization in Eq.(2.5) reproduces the Monte Carlo results for the energy of the normal state not only in the low x regime, but also for large values of the concentration parameter.

The results for the equation of state of the unitary Fermi gas are shown in Fig. 2.2 as a function of the concentration x. The dashed line corresponds to Eq.(2.5), while the solid line shows the polynomial best fit to the Fixed-Node Diffusion Monte Carlo (FN-DMC) results (circles) [59]. For a concentration $x = 1$, i.e. for a mixture of equal number of $\uparrow$ and $\downarrow$ atoms, both the energy of the normal and the superfluid state are shown, which yield $E_{\mathrm{N}}/(3/5E_{\mathrm{F}\uparrow}N_\uparrow) = 1.12(2)$ (white dot in Fig. 2.2) and $E_{\mathrm{SF}}/(3/5E_{\mathrm{F}\uparrow}N_\uparrow) = 0.84(2)$ (black diamond in Fig. 2.2), respectively [59].

From the equation of state of the normal phase one can determine both the transition between the mixed and the unpolarized superfluid phase and the transition between the mixed and the fully polarized phase. The conditions for the phase separation are obtained by requiring that the pressure and the chemical potential be the same in the two phases. The transition between the fully polarized is a second order phase transition and takes place at $x = 0$, which corresponds to $\mu_\downarrow/\mu_\uparrow = -3/5A$.

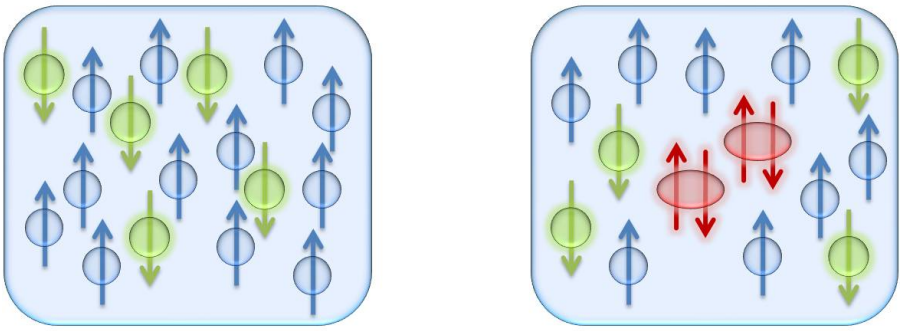

Figure 2.3: Left panel: Polarized Fermi gas with a concentration of $n_\downarrow/n_\uparrow < 0.44$. Right panel: For a concentration $n_\downarrow/n_\uparrow > 0.44$, the system starts nucleating a superfluid core.

For the normal to superfluid transition instead the critical concentration is $x_c = 0.44$ indicated by the arrow in Fig. 2.2, corresponding to $\mu_\downarrow/\mu_\uparrow = 0.017$. If the concentration is smaller than x_c, the system remains normal, whereas for $x > x_c$ it starts nucleating the superfluid phase as schematically shown in Fig. 2.3. This critical value of the concentration x_c is the Chandrasekhar-Clogston limit of polarization, above which superfluidity disappears. The normal to superfluid transition is a first order phase transition indicated by the nonconvexity of the Maxwell construction as shown by the coexistence line (dot-dashed) in Fig. 2.2.

The role of interactions and of the underlying quasiparticle concept becomes obvious when compared to the results obtained within BCS theory. Within BCS theory, the energy of the normal state at unitarity is just the sum of the noninteracting kinetic energies of the spin-↑ and spin-↓ component

$$\frac{E^{\mathrm{BCS}}(x)}{N_\uparrow} = \frac{3}{5}E_{F\uparrow}(1 + x^{5/3}), \tag{2.6}$$

and hence an increasing function of the concentration as shown in Fig. 2.4, where we also plot the energy of the normal state as introduced by Lobo *et al.*.

The parameter characterizing the interactions in the superfluid phase on the other hand is $\xi_{\mathrm{BCS}} = 0.59$, so that the superfluid energy is $E_{\mathrm{SF}}^{\mathrm{BCS}}/(3/5E_{\mathrm{F}\uparrow}N_\uparrow) = 1.18$. This yields for the critical concentration the value $x_c = 0.04$, which is significantly smaller than the value resulting from [59].

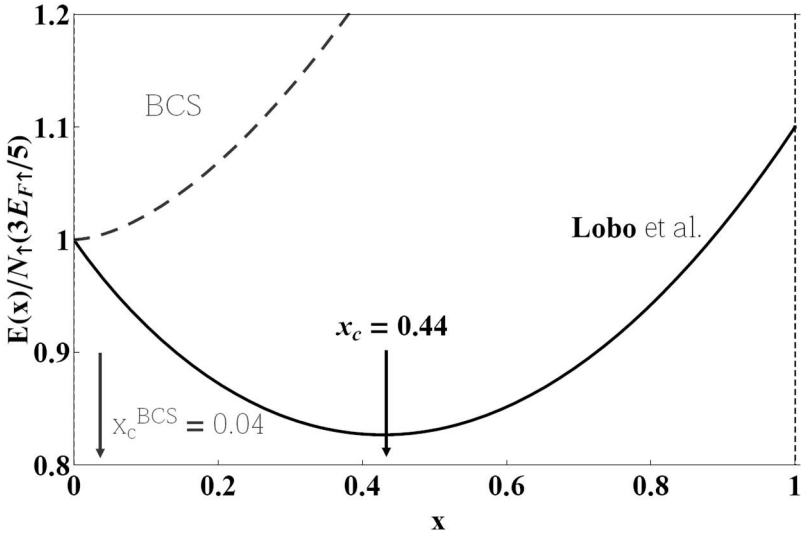

Figure 2.4: Energy of the normal state as derived by Lobo *et al.* (black solid) and critical concentration $x_c = 0.44$ for the normal to superfluid transition (black arrow). As a comparison, the energy as resulting from the BCS treatment (grey dashed), together with $x_c^{\mathrm{BCS}} = 0.04$ (grey arrow), is also shown.

2.3 Local Density Approximation for the Trapped System

In the experimentally relevant cases, where the number of atoms confined by a harmonic potential is of the order of $N \simeq 10^5 - 10^7$, the local density approximation (LDA, also referred to as semiclassical or Thomas-Fermi approximation) provides a simple description of the system. The LDA profits from the knowledge of the equation of state of the uniform system to deduce the behaviour of the system in a harmonic trap.

Here and in the following we will always consider systems at zero temperature, where the equation of state is provided by the density dependence $\epsilon(n)$ of the energy density. Then, within the local density approximation, it is assumed that, locally, the system behaves like a uniform gas, and the energy density can be expressed as $\epsilon(n) = nE(n)/N$, where $E(n)/N$ is the energy per atom of uniform matter. The energy of the trapped system can then be written in the integral form

$$E = \int d\mathbf{r}\{\epsilon[n(\mathbf{r})] + V_{ho}(\mathbf{r})n(\mathbf{r})\}, \tag{2.7}$$

which is the sum of the internal energy (first summand) and of the oscillatory energy (second summand) provided by the harmonic trapping potential $V_{ho}(\mathbf{r}) = \frac{1}{2}m(\omega_x^2 x^2 + \omega_y^2 y^2 + \omega_z^2 z^2)$. The value of the density profile at equilibrium is determined by the variational relation $\delta(E - \mu_0 N)/\partial n(\mathbf{r}) = 0$, which

yields the Thomas-Fermi equation

$$\mu_0 = \mu[n(\mathbf{r})] + V_{ho}(\mathbf{r}). \tag{2.8}$$

In the above equation, $\mu(n) = \partial\epsilon(n)/\partial n$ is the local chemical potential, which is determined by the equation of state of the uniform system, while μ_0 is the chemical potential of the trapped gas, which is fixed by $\int d\mathbf{r}\ n(\mathbf{r}) = N$.

The LDA can be applied when the relevant energies are much larger than the single-particle oscillator energy $\hbar\omega_i$, i.e., when $\mu_0 \gg \hbar\omega_i$ $(i = x, y, z)$. In the case of fermions due to the quantum pressure term related to the Pauli principle, one can apply the Thomas-Fermi relationship Eq.(2.8) even to the noninteracting configuration using the chemical potential $\mu(n) = (3\pi^2)^{2/3}(\hbar^2/2m)n^{2/3}$ of the noninteracting Fermi gas, which yields the equilibrium profile

$$n(\mathbf{r}) = \frac{8}{\pi^2}\frac{N}{R_x^0 R_y^0 R_z^0}\left[1 - \left(\frac{x}{R_x^0}\right)^2 - \left(\frac{y}{R_y^0}\right)^2 - \left(\frac{z}{R_z^0}\right)^2\right]^{3/2} \tag{2.9}$$

in the trap. In Eq.(2.9), $R_i^0 = a_{ho}(48N)^{1/6}(\omega_{ho}/\omega_i)$ $(i = x, y, z)$ are the Thomas-Fermi radii and $a_{ho} = \sqrt{\hbar/m\omega_{ho}}$ is the harmonic oscillator length. The Thomas-Fermi radius gives the width of the density distribution at $T = 0$.

2.4 Phase Separation in the Trapped System

For equal particle numbers, $N_\uparrow = N_\downarrow$, the system is completely superfluid while a polarization $P = 1$ indicates a fully polarized noninteracting Fermi gas. For values of the polarization $0 < P < P_c$ the system exhibits a phase separation between an unpolarized superfluid core and an external partially polarized normal shell. Hence, polarizing a Fermi superfluid through an imbalance of the spin population gives rise to a shell structure in the trap as shown schematically in Fig. 2.5.

To determine the condition of equilibrium between the superfluid and normal phase in the trap, we define R_S the surface which separates the superfluid from the partially polarized system, while $R_\uparrow$ is the Thomas-Fermi radius of the fully polarized normal part (see Fig. 2.5). Then we can write down the free energy in the trap as

$$\begin{aligned} E &= 2\int_{r<R_S} d\mathbf{r}\left[\epsilon_S(n_S(\mathbf{r})) - \mu_S^0 + V(\mathbf{r})\right] n_S(\mathbf{r}) \\ &+ \int_{R_S<r<R_\uparrow} d\mathbf{r}\Big\{\epsilon_N(x)n_\uparrow(\mathbf{r}) + V(\mathbf{r})[n_\downarrow(\mathbf{r}) + n_\uparrow(\mathbf{r})] \\ &\qquad - \mu_\uparrow^0 n_\uparrow(\mathbf{r}) - \mu_\downarrow^0 n_\downarrow(\mathbf{r})\Big\}, \end{aligned} \tag{2.10}$$

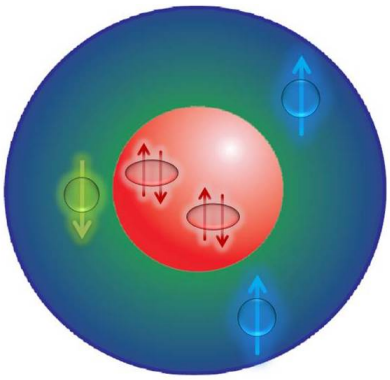

Figure 2.5: Sketch: Shell structure of the trapped system, consisting of a superfluid core (red) surrounded by a partially polarized shell (green), $N_\uparrow > N_\downarrow$, and fully $\uparrow$-polarized corona (blue).

where $\mu^0_{\uparrow(\downarrow)}$ is the chemical potential of the spin-$\uparrow$ (spin-$\downarrow$) component and $\mu^0_S = (\mu^0_\uparrow + \mu^0_\downarrow)/2$ is the superfluid chemical potential, respectively. To find the equilibrium we minimize the energy with respect to the densities of the superfluid and the normal part, which yields the the LDA expressions for the superfluid

$$\mu^0_S = \xi_S \frac{\hbar^2}{2m}(6\pi n_S)^{2/3} + V(\mathbf{r}), \tag{2.11}$$

and the normal phase

$$\mu^0_\uparrow = \left(g(x) - \frac{3}{5} x g'(x) \right) \frac{\hbar^2}{2m}(6\pi n_\uparrow)^{2/3} + V(\mathbf{r}), \tag{2.12}$$

$$\mu^0_\downarrow = \frac{3}{5} g'(x) \frac{\hbar^2}{2m}(6\pi n_\uparrow)^{2/3} + V(\mathbf{r}). \tag{2.13}$$

By varying the energy with respect to the superfluid border R_S we eventually find the equilibrium condition for the two phases in the trap, which is equivalent to implying that the pressure of the two phases be the same

$$\left(n_S^2 \frac{\partial \epsilon_S}{\partial n_S} \right)_{r=R_S} = \frac{1}{2} \left(n_\uparrow^2 \frac{\partial \epsilon_N(x)}{\partial n_\uparrow} + n_\uparrow n_\downarrow \frac{\partial \epsilon_N(x)}{\partial n_\downarrow} \right)_{r=R_S}. \tag{2.14}$$

From Eqs.(2.13) and (2.14) we obtain an implicit equation for the concentration at the border

$$g(x(R_S)) + \frac{3}{5}[1 - x(R_S)] g'(x(R_S)) - (2\xi_S)^{3/5}[g(x(R_S))]2/5 = 0. \tag{2.15}$$

In the superfluid phase the $\uparrow$ and $\downarrow$-densities are equal, such that a solution $x(R_S) < 1$ of Eq.(2.15) indicates density jumps between the single components at

the interface. At the border we find that $x(R_S) = 0.44$ which is identical with the Chandrasekhar-Clogston limit of the bulk system. The density jumps between the superfluid and the spin-up and spin-down component at the border can be easily calculated and are given by

$$\frac{n_\uparrow(R_S)}{n_S(R_S)} = \left(\frac{2\xi_S}{g(x(R_S))}\right)^{3/5} \sim 1.01, \tag{2.16}$$

$$\frac{n_\downarrow(R_S)}{n_S(R_S)} = x(R_S)\left(\frac{2\xi_S}{g(x(R_S))}\right)^{3/5} \sim 0.45. \tag{2.17}$$

From Eqs.(2.11-2.13) one can calculate the density profile as shown in Fig. 2.6 for a polarization $P = 0.44$. The system exhibits the typical shell structure consisting of a superfluid core, where the densities of both the spin components are equal, and a normal surrounding phase with $N_\uparrow > N_\downarrow$. Visible is also the significant jump in the minority component, while the spin-$\uparrow$ density is practically continuous.

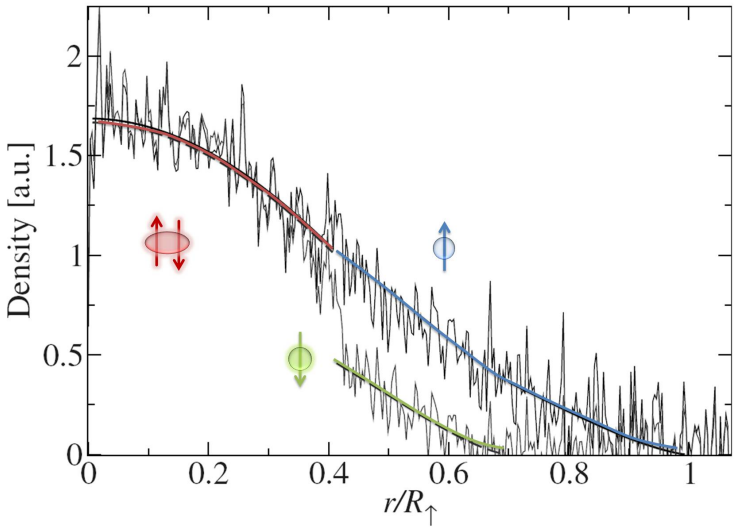

Figure 2.6: Density profiles for a polarization $P = 0.44$. Theory: solid red (SF), green ($\downarrow$-component) and blue ($\uparrow$-component). Experiment: The black (red) line is the spin-$\uparrow$ (spin-$\downarrow$) density as reported in [63]. Figure from [60].

Importantly, from the densities one can predict the critical polarization P_c in the trap, i.e. the particle imbalance above which the superfluid disappears and only the normal phase is present. The critical polarization in the trap corresponds to the Chandrasekhar-Clogston limit of the bulk system, and with the present values of A, m^*, and B the critical polarization is given by $P_c = 0.77$. The proper inclusion of interactions is crucial to correctly describe the normal to superfluid

quantum phase transition and the critical polarization. For the trapped system, BCS mean-field approach would predict the incorrect value $P_c \simeq 1$ for the critical polarization.

In Fig. 2.6 the theoretical density profiles are shown together with the experimental data from the MIT group [50, 63]. The comparison with the MIT experiments is favored by the possibility to apply the local density approximation due to the large values of the total particle number N and hence negligible details of the interface at a microscopic scale. Note, that for the prediction of the density profiles as revealed in the experiment no other input is needed than the polarization P, apart from, of course, the proper equation of state of the superfluid and the normal phase.

2.5 The Limit of High Polarizations and the Fermi Polaron

In the limit of high polarizations, to the leading order in x Eqs. (2.13) yield [60]

$$\mu_\uparrow^0 = \frac{\hbar^2}{2m}\left(6\pi^2 n_\uparrow\right)^{2/3} + V(\mathbf{r}), \tag{2.18}$$

$$\mu_\downarrow^0 + \frac{3}{5}A\mu_\uparrow^0 = \frac{\hbar}{2m^*}\left(6\pi^2 n_\downarrow\right)^{2/3} + V(\mathbf{r})\left(1+\frac{3}{5}A\right). \tag{2.19}$$

with $m^*/m = 1.09(2)$ and $A = 0.99(1)$ [65]. Both the effective mass m^*/m as well as the binding energy A enter in the expressions, proving the role of the interactions. The background spin-$\uparrow$ sea has the density profile of an ideal Fermi gas, while the radius of the spin-$\downarrow$ component is reduced by

$$R_\downarrow = R_\downarrow^0\left[\left(1+\frac{3}{5}A\right)\frac{m}{m^*}\right]^{-1/4}, \tag{2.20}$$

where $R_\downarrow^0 = (48N_\downarrow)^{1/6}\sqrt{\hbar/(m\omega)}$ is the Thomas Fermi radius and

$$\frac{\omega^*}{\omega} = \sqrt{\frac{m^*}{m}\left(1+\frac{3}{5}\right)A} \tag{2.21}$$

is the effective trapping frequency felt by the spin down particles due to their interaction with the $\uparrow$-component.

The latter relation has been recently employed in experiments [87] to directly determine the polaron effective mass from dynamical measurements of low lying excitation modes. In [87], Nascimbène *et al.* excite the axial breathing mode of

an ultracold Fermi gas in order to study the dynamics of the radii of the majority and minority component for different polarizations. The analysis of the Fourier spectrum of the dynamical evolution of the radii reveals that for $P < 0.75$ the oscillation rates of the $\uparrow$ and $\downarrow$ components are equal and hence strongly coupled, indicated by a single peak in the spectrum.

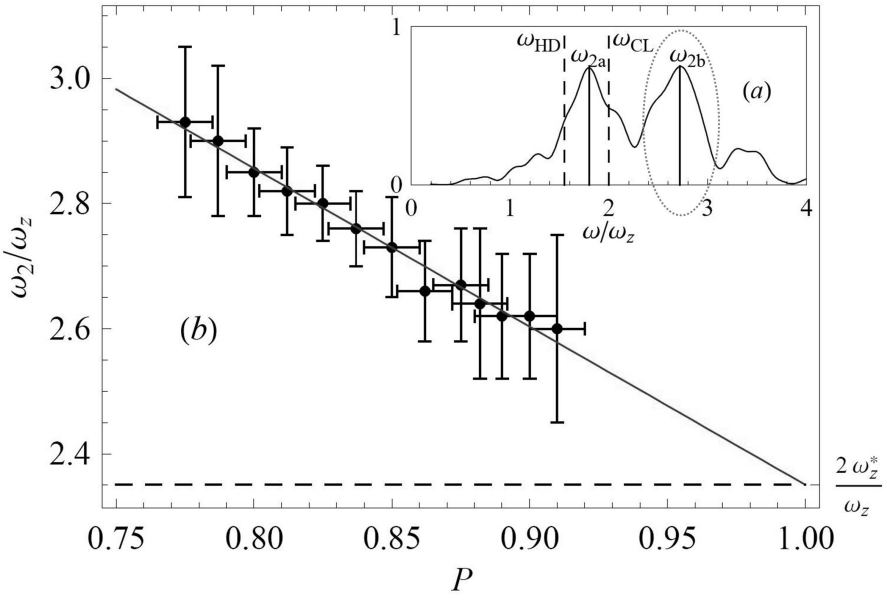

Figure 2.7: (a) Frequency power spectrum for P = 0.90(2). The peak between ω_{HD} and ω_{CL} corresponds to the oscillation in phase with the majority, the other one to the polaron oscillation (grey dashed circle). (b) Frequency of the polaron component as a function of polarization. All frequencies are normalized to ω_z, from [87].

For $P \simeq 1$ however, the spectrum reveals two peaks as shown in Fig. 2.7 (a), indicating that the minority component oscillates out of phase with the majority cloud. The frequency ω_{2b} of the second peak (grey dashed circle in Fig. 2.7 (a)) is then identified with ω^*/ω in Eq.(2.21) to extract the value of the effective mass. With an interpolated frequency of $\omega^*/\omega \sim 1.175$ for $P \to 1$ (see Fig. 2.7 (b)), the effective mass is determined to be $m^*/m = 1.17(10)$. This is in good agreement with theoretical [65, 88] predictions and static observations, where the value of the effective mass was extracted by determining the energy density of a resonantly interacting Fermi gas from the *in situ* density distributions [60, 92]. The dynamic measurement [87] not only confirms the results of the effective mass, but also the underlying Fermi polaron concept.

2.6 Conclusions

The highly polarized Fermi gas at unitarity is an example of a strongly interacting Fermi liquid which remains normal even at temperatures close to zero. The assumption of a phase separation between a superfluid and polarized normal gas describes accurately the behavior of the trapped resonant Fermi gas at $T = 0$. The theory of the normal state agrees with all the main results obtained by the MIT group such as the prediction of the Chandrasekhar-Clogston limit for the concentration $x_c = 0.44$ as well as for the critical polarization $P_c \sim 0.77$ in the trap [46, 50, 63, 64]. The two-shell structure for $P < P_c$, and the correct value of the density jump between the superfluid and the normal component at the interface [60] were found to be in good agreement. In contrast to this, BCS results are quantitatively not correct as shown by the value of the critical concentration, which within BCS theory is predicted to be $x_c = 0.04$. This proves the role of interactions at unitarity in the normal phase, and shows that their inclusion in the equation of state is necessary for predicting correctly the main features of the trapped gas.

In the limit of high polarizations, one can derive simplified expression for the densities of the majority and minority components. While the majority species has the density profile of an ideal Fermi gas, the density profile of the minority species is quenched due to the interactions with the $\uparrow$-component and feels a renormalized potential. This influences remarkably the excitations of collective modes and their spectrum as calculated in [60] and experimentally shown in [87].

3 Unitary Fermi Gas under Adiabatic Rotation

It is well known that the response to a transverse probe, like the rotation, is a crucial tool to test the superfluidity of a system. The most famous example in this contest is the classic "rotating bucket"experiment on superfluid ^{4}He [93], where a cylindrical container is rotated as the liquid is cooled. For trapped superfluid gases, this can be achieved by rotating the confining potential. While a normal gas rotates in a classical rigid way, a superfluid features a different behavior.

The effect of the rotation on the behavior of a superfluid is a longstanding subject of investigation in condensed matter as well as in nuclear systems [94, 95]. Due to the irrotationality constraint imposed by the existence of the order parameter a superfluid cannot rotate like a normal fluid. The phenomena exhibited by superfluids are multifaceted and include the quenching of the moment of inertia at small angular velocities and the appearance of quantized vortices at higher velocities. Vortices have already been observed in these polarized configurations and shown to disappear for high polarizations [49].

Previous theoretical work on superfluid rotating Fermi gases has mainly focused on the dynamics [96] and on the instability [97, 98] of configurations with high vortex density. Here we investigate the behavior of the gas *when quantized vortices are not formed*. Experimentally this scenario is achievable through an adiabatic ramping of the the angular velocity of the rotating trap starting from a configuration at rest. In the case of trapped BEC's this procedure has permitted to reach values of angular velocity significantly higher than the critical angular velocity for the formation of quantized vortices whose nucleation is inhibited by the presence of a barrier.

Under these conditions new physical phenomena occur like, for example, the spontaneous breaking of rotational symmetry caused by the energetic instability of the surface modes [99] and, at even higher angular velocities, the occurrence of dynamic instabilities [100]. These phenomena have been observed experimentally in BEC's [101], confirming in a qualitative and quantitative way the correctness of the irrotational hydrodynamic picture of rotating superfluids.

In the following we show that a trapped rotating Fermi gas at unitarity exhibits a further interesting phenomenon, associated with the breaking of superfluidity

in the external region. Indeed, atoms prefer to be in the normal phase because of the energy gain due to the rotation. This mechanism of the depletion of the superfluid due to the rotation has also been recently confirmed within BCS mean-field theory [102]. The occurrence of this phenomenon requires proper conditions of adiabaticity in the ramping of the rotation of the trap in order to avoid the formation of vortices, a condition that has been already successfully realized in rotating Bose-Einstein condensates [101, 103]. The results presented in this chapter have been published in [79, 80].

We will first discuss the effect of rotation on a polarized Fermi gas, after which we will consider the particular case of a nonpolarized superfluid system.

3.1 Rotating Adiabatically a Polarized Fermi Gas

We consider a polarized ($N_\uparrow \neq N_\downarrow$) Fermi gas at unitarity confined by a harmonic potential $V(\mathbf{r}) = m(\omega_x^2 x^2 + \omega_y^2 y^2 + \omega_z^2 z^2)/2$, rotating adiabatically with angular velocity Ω along the z-axis. We study the problem in the rotating frame of the trap, where the potential is static and the Hamiltonian contains the additional term $-\Omega L_Z$.

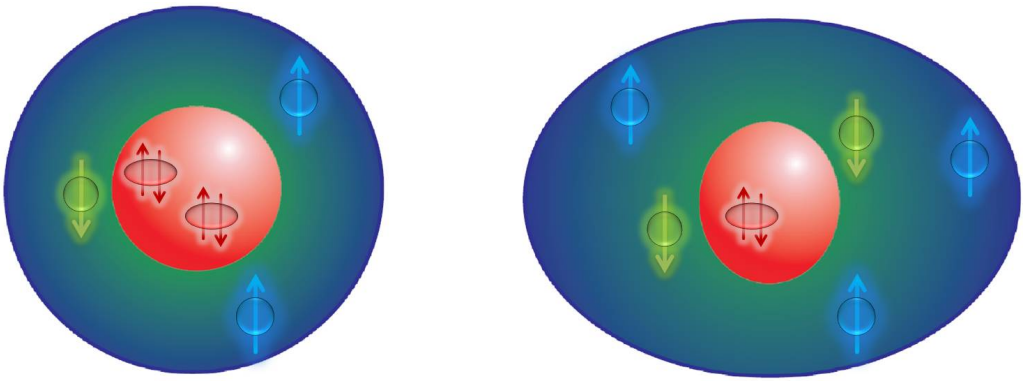

Figure 3.1: The typical shell structure of the trapped system consisting of a superfluid core (red) surrounded by a partially (green) and fully polarized (blue) normal shell for a polarization $P = 0.44$, $\Omega = 0$ (left panel) and $\Omega = 0.5\omega_\perp$ (right panel), respectively. The superfluid is squeezed in the radial direction while the normal part exhibits the bulge effect due to the rotation.

In the LDA the grand canonical energy of the rotating configuration at zero

temperature takes the form

$$\begin{aligned} E &= \int d\mathbf{r} \left(\epsilon(n_\uparrow(\mathbf{r}), n_\downarrow(\mathbf{r})) + V(\mathbf{r}) + \frac{1}{2}mv^2 - m\Omega(\mathbf{r}\times\mathbf{v})_\mathrm{Z} \right) n(\mathbf{r}) \\ &\quad - \int d\mathbf{r}[\mu_\uparrow^0 n_\uparrow(\mathbf{r}) + \mu_\downarrow^0 n_\downarrow(\mathbf{r})], \end{aligned} \tag{3.1}$$

where $\epsilon(n_\uparrow(\mathbf{r}), n_\downarrow(\mathbf{r}))$ is the energy density per particle depending on the $n_{\uparrow,\downarrow}(\mathbf{r})$ densities of the two spin species, $\mathbf{v}$ is the velocity field, $\mu_\uparrow^0$ and $\mu_\downarrow^0$ are the chemical potentials of the $\uparrow$ and $\downarrow$ particles, and $n(\mathbf{r}) = n_\uparrow(\mathbf{r}) + n_\downarrow(\mathbf{r})$ is the total density.

We assume that the phase separation in the trap manifests as the formation of an inner unpolarized superfluid core occupying the region $r < R_\mathrm{S}(\theta,\phi)$ surrounded by an external normal shell, which is confined to $R_\mathrm{S}(\theta,\phi) < r < R_\mathrm{N}(\theta,\phi)$ as shown in Fig. 3.1. Here, we term $R_\mathrm{S}(\theta,\phi)$ the interface separating the superfluid from the normal phase and $R_\mathrm{N}(\theta,\phi)$ the Thomas-Fermi radius of the gas where the density vanishes. Thus, the integral (3.1) splits into two parts

$$\begin{aligned} E &= 2\int_{r<R_\mathrm{S}} d\mathbf{r} \left(\epsilon_\mathrm{S}(n_\mathrm{S}(\mathbf{r})) - \mu_\mathrm{S}^0 + V(\mathbf{r}) + \frac{1}{2}mv_\mathrm{S}^2 - m\Omega(\mathbf{r}\times\mathbf{v}_\mathrm{S})_\mathrm{Z} \right) n_\mathrm{S}(\mathbf{r}) \\ &\quad + \int_{R_\mathrm{S}<r<R_\mathrm{N}} d\mathbf{r} \left[\epsilon_\mathrm{N}(x(\mathbf{r}))n_\uparrow(\mathbf{r}) - \mu_\uparrow^0 n_\uparrow(\mathbf{r}) - \mu_\downarrow^0 n_\downarrow(\mathbf{r}) \right] \\ &\quad + \left(V(\mathbf{r}) + \frac{1}{2}mv_\mathrm{N}^2 - m\Omega(\mathbf{r}\times\mathbf{v}_\mathrm{N})_\mathrm{Z} \right) n(\mathbf{r}), \end{aligned} \tag{3.2}$$

In this equation, $\epsilon_\mathrm{S}(n_\mathrm{S}(\mathbf{r}))$ is the energy density of the superfluid as given by Eq.(2.3), while $\epsilon_\mathrm{N}(x(\mathbf{r}))$ is the energy density of the normal state as given by Eq.(2.5), $\mu_\mathrm{S}^0 = (\mu_\uparrow^0 + \mu_\downarrow^0)/2$ is the superfluid chemical potential and $n_{\uparrow,\downarrow}(\mathbf{r})$ the $\uparrow$ and $\downarrow$ densities in the normal phase. In the above equation we have distinguished between the velocity fields $\mathbf{v}_\mathrm{S}$ and $\mathbf{v}_\mathrm{N}$ in the superfluid and normal phases, respectively.

To find the equilibrium conditions, we minimize the energy with respect to the densities, to the velocity fields as well as with respect to the border surface $R_\mathrm{S}(\theta,\phi)$. In the case of the superfluid the velocity field obeys the irrotationality constraint and can thus be written as $\mathbf{v}_\mathrm{S} = \nabla\Phi$. Variation of the energy with respect to the velocity potential Φ yields the continuity equation

$$\nabla \cdot n_\mathrm{S}(\nabla\Phi - \boldsymbol{\Omega}\times\mathbf{r}) = 0, \tag{3.3}$$

while the variation with respect to the superfluid density n_S yields the LDA relationship

$$\mu_{\rm S}^0 = \xi_{\rm S}\frac{\hbar^2}{2m}(6\pi^2 n_{\rm S})^{2/3} + V^{\rm S}(\mathbf{r}), \tag{3.4}$$

where $V^{\rm S}(\mathbf{r}) = V(\mathbf{r}) + \frac{1}{2}mv^2 - m\Omega(\mathbf{r}\times\mathbf{v}_{\rm S})_{\rm Z}$ is the effective harmonic potential felt by the superfluid.

Using the same procedure for the normal part (without the irrotationality constraint) we get $\mathbf{v}_{\rm N} = \mathbf{\Omega}\times\mathbf{r}$, i.e. it rotates rigidly. The variation with respect to the densities gives the LDA expressions

$$\mu_\uparrow^0 = \left(g(x) - \frac{3}{5}xg'(x)\right)\frac{\hbar^2}{2m}(6\pi^2 n_\uparrow)^{2/3} + V^{\rm N}(\mathbf{r}), \tag{3.5}$$

$$\mu_\downarrow^0 = \frac{3}{5}g'(x)\frac{\hbar^2}{2m}(6\pi^2 n_\uparrow)^{2/3} + V^{\rm N}(\mathbf{r}), \tag{3.6}$$

where the effective potential $V^{\rm N}(\mathbf{r})$ felt by the particles in the normal phase is now squeezed due to the rigid rotation according to $(\omega_x^{\rm N})^2 = \omega_x^2 - \Omega^2$, $(\omega_y^{\rm N})^2 = \omega_y^2 - \Omega^2$.

By varying the energy (3.2) with respect to $R_{\rm S}(\theta,\phi)$ we eventually find the equilibrium condition for the coexistence of the two phases in the trap. This is equivalent to implying that the pressure of the two phases be the same

$$\left(n_{\rm S}^2\frac{\partial\epsilon_{\rm S}}{\partial n_{\rm S}}\right)_{r=R_{\rm S}} = \frac{1}{2}\left(n_\uparrow^2\frac{\partial\epsilon_{\rm N}(x)}{\partial n_\uparrow} + n_\downarrow n_\uparrow\frac{\partial\epsilon_{\rm N}(x)}{\partial n_\downarrow}\right)_{r=R_{\rm S}}. \tag{3.7}$$

Using the expressions for the energy densities (2.5) and (2.3) we obtain an equation for the density discontinuity in the trap given by

$$\frac{n_\uparrow(R_{\rm S})}{n_{\rm S}(R_{\rm S})} = \left(\frac{2\xi_{\rm S}}{g(x(R_{\rm S}))}\right)^{3/5} \equiv \gamma(x(R_{\rm S})), \tag{3.8}$$

where $x(R_{\rm S})$ is the local concentration at the interface. The combination of the above equation with Eqs.(3.4) and (3.5) yields the useful relationship

$$\left(\mu_{\rm S}^0 - V^{\rm S}(R_{\rm S})\right) = \gamma(x(R_{\rm S}))\left(\mu_\uparrow^0 - V^{\rm N}(R_{\rm S})\right), \tag{3.9}$$

which determines the surface $R_{\rm S}(\theta,\phi)$ separating the superfluid and the normal part.

Eventually using also Eq.(3.6) we find an expression which implicitly defines the concentration as a function of the position at the interface

$$g(x(R_{\rm S})) + \frac{3}{5}[1-x(R_{\rm S})]g'(x(R_{\rm S})) - (2\xi_{\rm S})^{3/5}[g(x(R_{\rm S}))]^{2/5} = \frac{2(V^{\rm S}(R_{\rm S})-V^{\rm N}(R_{\rm S}))}{E_{F\uparrow}(R_{\rm S})}. \quad (3.10)$$

In absence of rotation $V^{\rm S} = V^{\rm N} \equiv V$ the solution of Eq.(3.10) yields the value $x(R_{\rm S}) = 0.44$ [59]. This value coincides with the maximum concentration achievable in the normal phase of uniform matter before phase separation. Since the rotation affects differently the potentials $V^{\rm S}$ and $V^{\rm N}$, the value of the concentration depends now on the angular position of the interface. It ranges from a minimum value $x[R_{\rm S}(0,\phi)] = x_{\rm c} = 0.44$ along the z-axis (where the effect of the rotation is vanishing) to a maximum, Ω dependent value $x[R_{\rm S}(\pi/2,\phi)]$ in the xy plane (where the effect of the rotation is largest).

The effect of the rotation is thus to enhance the average value of the concentration in the normal phase and hence to favour the depletion of the superfluid. This is physically understood by noticing that in the rotating frame the atoms in the normal part gain the energy $\frac{1}{2}mv_{\rm N}^2(\mathbf{r})$ due to the centrifugal force. Thus, the energy of the normal part, in the rotating frame, can become smaller than the value in the superfluid [79]. As will be shown below, the main effect is to change the critical concentration $x_{\rm c}$ at the interface.

Notice, however, that the critical *global* concentration $P_{\rm c}$ for the system to start nucleating the central superfluid core is not affected by the rotation and keeps the nonrotating value $P_{\rm c} = 0.77$. The reason for that is easily explained within the local density approximation used here.

Just above $P_{\rm c}$ the system is completely normal and the only effect of the rotation is the squeezing of the transverse trapping frequencies, while in the z direction the system remains unaffected (see Eqs.(3.5, 3.6)). Since at $P_{\rm c}$ the superfluid is nucleated at the center of the trap where centrifugal effects are absent, the local condition for equilibrium between the superfluid and the normal component is the same as without rotation. The calculation of the critical polarization proceeds then in exactly the same way as without rotation, but for a simple rescaling of the trapping frequencies which has no effect on the value of $P_{\rm c}$.

Results

In the following we will assume $\omega_x = \omega_y = \omega_\perp$ and we consider the solution $\mathbf{v}_{\rm S} = \mathbf{0}$, thus a nonrotating axi-symmetric superfluid and consequently $V^{\rm S} \equiv V$. In this case the local concentration depends only on the polar angle θ and the superfluid radius takes the form

$$R_{\rm S}^2(\theta) = \frac{2}{m}\frac{(\mu_{\rm S}^0 - \gamma(x(R_{\rm S}))\mu_\uparrow^0)}{(1-\gamma(x(R_{\rm S})))} \times \left(\omega_z^2\cos^2\theta + \omega_\perp^2\sin^2\theta + \frac{\gamma(x(R_{\rm S}))}{1-\gamma(x(R_{\rm S}))}\Omega^2\sin^2\theta\right)^{-1}, \quad (3.11)$$

while the Thomas-Fermi radius $R_{\rm N}$ of the normal gas is fixed by the condition $\mu_\uparrow = V^{\rm N}(\mathbf{r})$ yielding

$$R_{\rm N}^2(\theta) = \frac{2\mu_\uparrow^0}{m}\left(\omega_z^2\cos^2\theta + \omega_\perp^2\sin^2\theta - \Omega^2\sin^2\theta\right)^{-1} \geq R_{\rm S}^2(\theta). \quad (3.12)$$

The values of the chemical potentials are fixed by the normalization

$$\int_{r<R_{\rm S}} d\mathbf{r}\ \ n_{\rm S}(\mathbf{r}) + \int_{R_{\rm S}<r<R_{\rm N}} d\mathbf{r}\ n_\uparrow(\mathbf{r}) = N_\uparrow, \quad (3.13)$$

and

$$\int_{r<R_{\rm S}} d\mathbf{r}\ \ n_{\rm S}(\mathbf{r}) + \int_{R_{\rm S}<r<R_{\rm N}} d\mathbf{r}\ n_\downarrow(\mathbf{r}) = N_\downarrow. \quad (3.14)$$

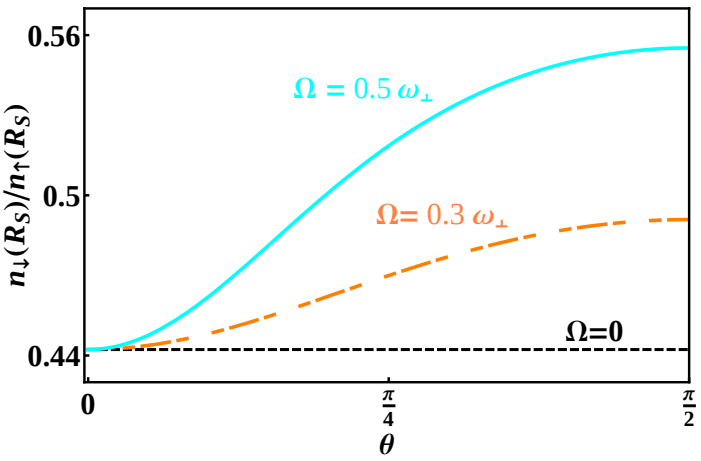

Figure 3.2: Concentration $n_\downarrow/n_\uparrow$ for $P = 0.44$, $\Omega = 0$ (black small dashed), $\Omega = 0.3\omega_\perp$ (orange dashed), and $\Omega = 0.5\omega_\perp$ (turquoise solid) as a function of the polar angle θ.

In Fig. 3.2 we plot the concentration $n_\downarrow/n_\uparrow$ at the interface for $P = 0.44$ as a function of the polar angle θ for different values of the angular velocity. The figure clearly points out the increase of the concentration when one moves from the z-axis to the xy plane.

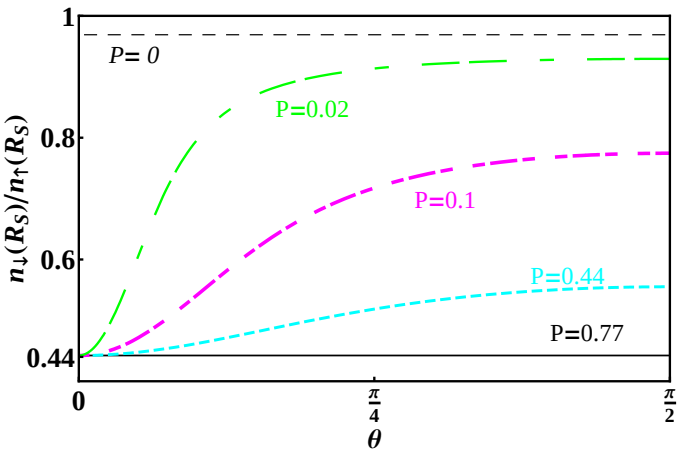

Figure 3.3: Concentration $n_\downarrow/n_\uparrow$ at the superfluid-normal interface as a function of the polar angle θ for $\Omega = 0.5\omega_\perp$ and different values of the polarization: $P = 0.77$ (black solid), $P = 0.44$ (turquoise dashed), $P = 0.1$ (pink dotted-dashed), $P = 0.2$ (green long dashed) and $P = 0$ (black thin dashed).

Complementary to this is Fig. 3.3, where we show the concentration $n_\downarrow/n_\uparrow$ for a fixed angular velocity $\Omega = 0.5\omega_\perp$ and different values of the polarization as a function of the angular position. This clearly reveals the nature of the normal state by highlighting the two extreme and singular cases $P = 0.77$ and $P = 0$. As already pointed out, at the threshold value $P = 0.77$ for the nucleation of the superfluid, the rotation does not affect the value of x_c as evidenced by the solid black line in Fig. 3.3. On the other hand, in the case that $P = 0$ the critical concentration is constant and singular $n_\downarrow/n_\uparrow = 1$ for all angles but $\theta = 0$. For all other values $0 < P < P_c$, the rotation has a considerable effect on the local value $n_\downarrow/n_\uparrow$.

The density profiles exhibit a typical shell structure. In Fig. 3.4 we plot the radii of the superfluid (red), $\uparrow$ (blue), and $\downarrow$ (green) component in units of the Thomas-Fermi radius of an ideal gas $R^0_\uparrow$ versus the angular velocity $\Omega/\omega_\perp$ for a polarization $P = 0.44$. While the superfluid radius decreases until the superfluid core completely vanishes at $\Omega = \omega_\perp$, the Thomas-Fermi radii of the $\uparrow$ and $\downarrow$ component diverge for $\Omega = \omega_\perp$ as a consequence of the centrifugal effect. It is curious to see that while the normal part exhibits the typical bulge effect, the superfluid behaves in the opposite way. In fact, its radial size becomes smaller than the axial one as a consequence of the depletion caused by the rotation, with consequently inversion of the behavior of the aspect ratio $R_\perp/R_Z$ (see Fig. 3.1).

It is worth mentioning that at large enough angular velocities the system exhibits solutions which break the axial symmetry [99]. Such critical value is predicted to be $\Omega_{cr} \sim 0.5\omega_\perp$ as we have shown in detail in chapter II. The results in Figs.

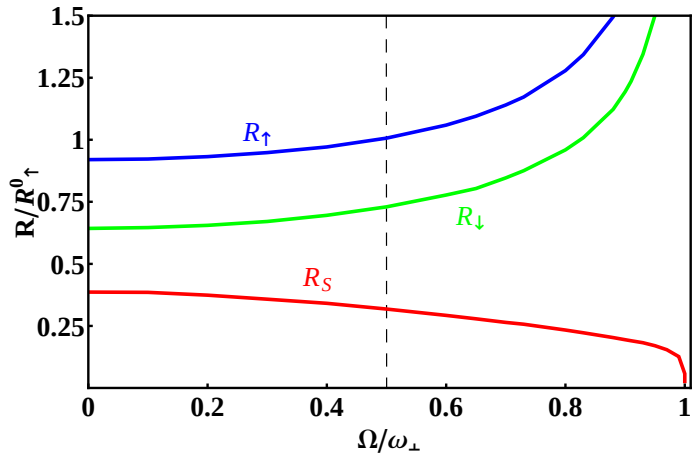

6

Figure 3.4: Radii in units of $R^0_\uparrow$ versus angular velocity for $\theta = \pi/2$ of the superfluid (red), $n_\uparrow$ (blue), and $n_\downarrow$ (green) for a polarization $P = 0.44$.

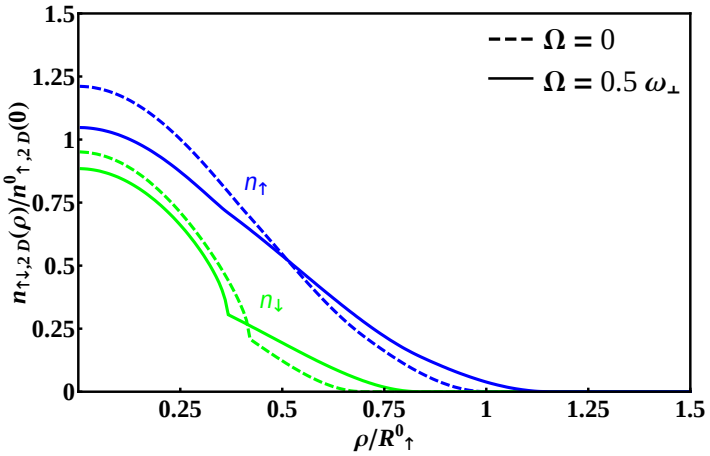

Figure 3.5: Column densities of the $n_\uparrow$ (blue), and $n_\downarrow$ (green) component in a spherical harmonic trap for a polarization $P = 0.44$ and $\Omega = 0$ (dashed lines) and $\Omega = 0.5\omega_\perp$ (solid lines).

3.4, 3.9, and 3.10 for $\Omega > 0.5\omega_\perp$ (dashed vertical line) correspond to the axial symmetric solution of the problem.

In an experiment the effect of phase separation as well as the radius of the superfluid are best revealed as a knee in the *in situ* column density $n_{\sigma,2D}(\rho) \equiv \int dz\ n_\sigma(\mathbf{r})$, with $\sigma = \uparrow, \downarrow$. These observables can nowadays be measured with high precision using phase-contrast image techniques. We expect that the position of the knee for a fixed polarization will depend on the angular velocity. This is clearly shown in the column density of the majority ($\uparrow$, blue) and the minority

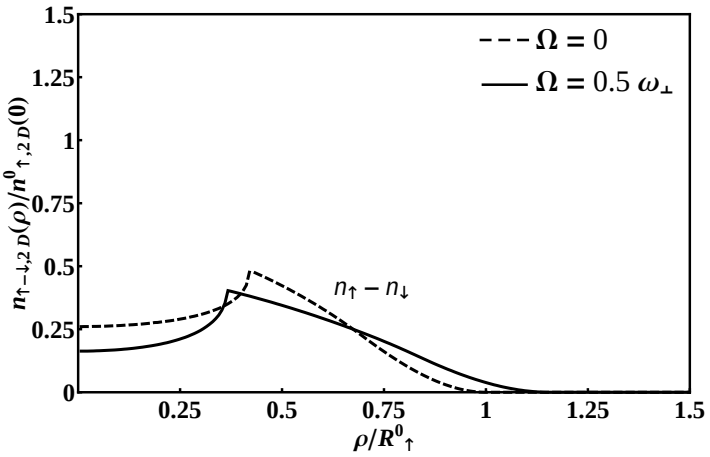

Figure 3.6: Difference of the column densities of the $n_\uparrow$ and $n_\downarrow$ components in a spherical harmonic trap for a polarization $P = 0.44$ and $\Omega = 0$ (dashed line) and $\Omega = 0.5\omega_\perp$ (solid line).

($\downarrow$, green) components, Fig. 3.5, for $\Omega = 0$ (dashed) and $\Omega = 0.5\omega_\perp$ (solid), as well as in the density difference, Fig. 3.6.

The knee is a direct consequence of the discontinuity exhibited by the three dimensional density shown in Figs. 3.7 and 3.8, where we plot $n_{\rm S}$ (red), $n_\uparrow$ (blue), and $n_\downarrow$ (green) in a spherical trap for $\theta = 0$ and $\theta = \pi/2$, respectively. The densities and the radial coordinate have been renormalized with respect to the central value of $n_\uparrow^0$ and the Thomas-Fermi radius $R_\uparrow^0$ of an ideal gas. In accordance to the results for the superfluid radius shown in Fig. 3.4 the discontinuity in the density takes place at a smaller value of the radius compared to the nonrotating configuration.

For $\theta = 0$ the densities $n_\uparrow$ and $n_\downarrow$ jump from the superfluid value $n_{\rm S}$ to the values $n_\uparrow \sim 1.01 n_{\rm S}$ and $n_\downarrow = x_{\rm c} n_\uparrow \simeq 0.44 n_{\rm S}$ as one enters the normal phase, precisely as in the nonrotating case [59]. Yet for $\theta = \pi/2$ the behavior is different and, in particular, for $\Omega = 0.5\omega_\perp$ the densities jump from $n_{\rm S}$ to $n_\uparrow \simeq 0.99 n_{\rm S}$ and $n_\downarrow \simeq 0.55 n_{\rm S}$. The smaller relative jump with respect to the nonrotating case reflects the smaller polarization (higher concentration x) exhibited by the rotating normal phase at the interface.

Further insight on the effect of the rotation is provided by the depletion of the superfluid. In Fig. 3.9 we plot the ratio between the number of particles in the superfluid $N_{\rm S}$ and the total number N (superfluid fraction) as a function of the angular velocity. This effect is especially pronounced for small polarizations (Fig. 3.9 black line, $P = 0$) since the depletion for higher polarization is large already in the nonrotating case.

Finally in Fig. 3.10 we plot the angular momentum $L_{\rm Z} = \Omega \int d\mathbf{r}(x^2 + y^2) n_{\rm N}(\mathbf{r})$

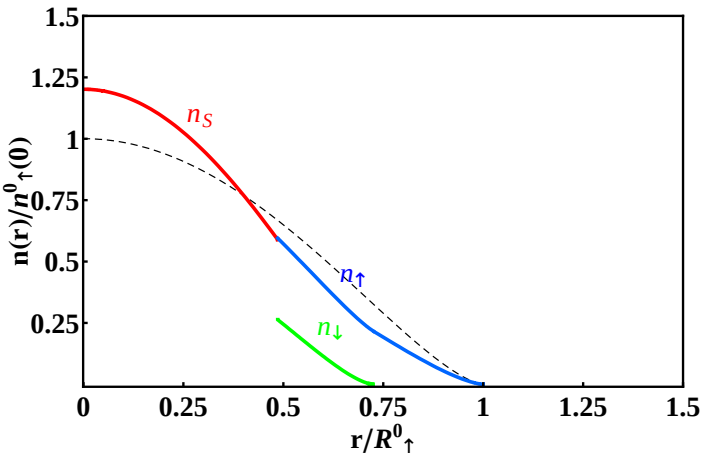

Figure 3.7: Density profiles for $\theta = 0$ of the superfluid (red), $n_\uparrow$ (blue), and $n_\downarrow$ (green) in a spherical harmonic trap for a polarization $P = 0.44$ and $\Omega = 0.5\omega_\perp$ in units of the central density of the noninteracting gas (dashed line).

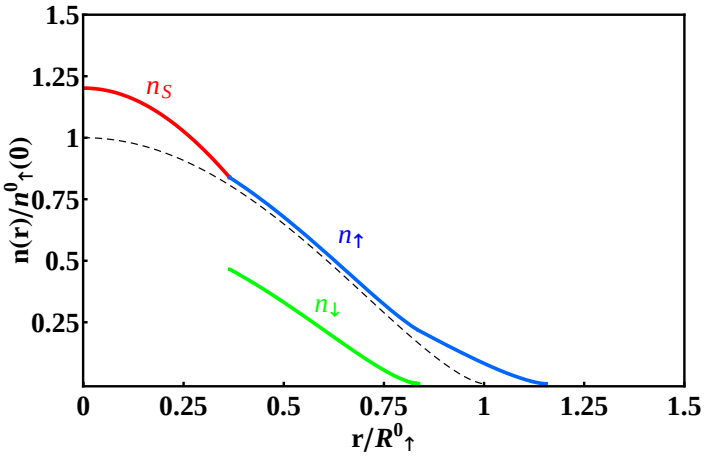

Figure 3.8: Density profiles for $\theta = \pi/2$ of the superfluid (red), $n_\uparrow$ (blue), and $n_\downarrow$ (green) in a spherical harmonic trap for a polarization $P = 0.44$ and $\Omega = 0.5\omega_\perp$ in units of the central density of the noninteracting gas (dashed line).

of the system for different polarizations. For an axi-symmetric configuration the superfluid does not carry angular momentum which is thus provided only by the normal component. Hence, the more particles are in the normal part, the stronger the response of the system to the rotation.

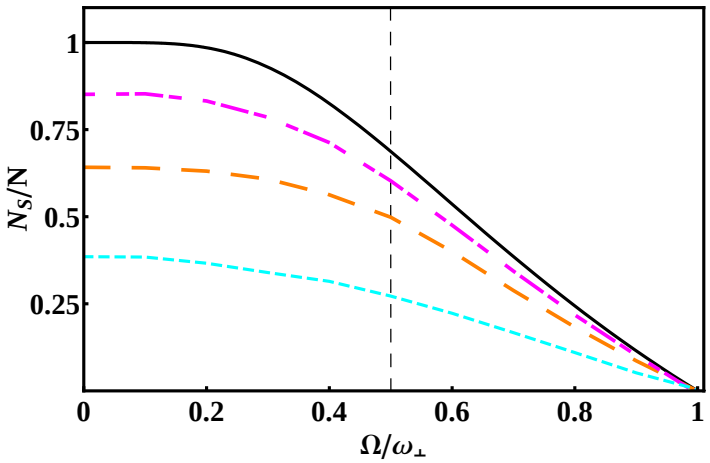

Figure 3.9: Evolution of the superfluid particle number for different polarizations $P = 0$ (black solid), $P = 0.1$ (pink dot-dashed) , $P = 0.25$ (orange large dashed) and $P = 0.44$ (turquoise small dashed) as a function of $\Omega/\omega_\perp$.

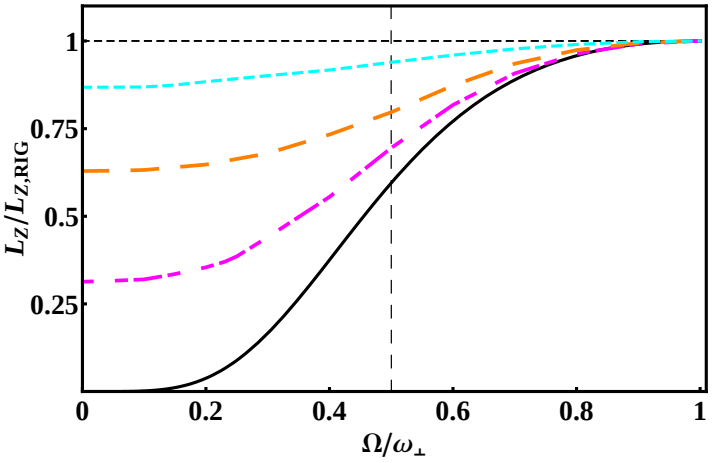

Figure 3.10: Angular momentum L_Z in units of the rigid value for different polarizations (black solid $P = 0$, pink dot-dashed $P = 0.1$, orange large dashed $P = 0.25$ and turquoise small dashed $P = 0.44$) as a function of $\Omega/\omega_\perp$.

Conclusions

In conclusion we have analyzed the effect of adiabatic rotation on a polarized Fermi gas at unitarity, assuming phase separation between a superfluid and a normal phase. We find that the normal phase is energetically favoured by the rotation and thus the superfluid is further depleted with respect to the nonrotating configuration. The normal region exhibits the typical bulge effect due to the centrifugal force while the superfluid is squeezed. This has clear observable

effects on the density profiles which can be addressed experimentally. A striking feature is that although the *g*lobal polarization is not affected by the rotation, the concentration $n_\downarrow/n_\uparrow$ at the border increases from the non-rotating value on the z-axis to a maximum value in the xy plane.

In our work we assume that the polarized system separates in only two phases. This assumption works well for the experiment carried out so far [60]. In the rotating case other phases could show up and it would be very interesting to see how they affect the results. For example, within BCS theory a third superfluid phase is found to occupy a small region at the interface (see [102] and discussion at the end of this chapter), but a more microscopic investigation of the phase separation at unitarity is necessary to settle the problem.

3.2 Rotating Adiabatically a Unitary Fermi Superfluid

A particular case of the general situation described in the previous section is is the rotation of a unitary Fermi superfluid, where $N_\uparrow = N_\downarrow$. In this case, the rotation of the initially fully superfluid system produces a phase separation between a superfluid core and a rotating normal gas.

The System

We are interested in an unpolarized superfluid confined in a harmonic potential $V(\mathbf{r}) = m(\omega_x^2 x^2 + \omega_y^2 y^2 + \omega_z^2 z^2)/2$, rotating with angular velocity Ω along z as shown in Fig. 3.11.

We study the problem in the frame rotating with the trap where the potential is static and the Hamiltonian is $H - \Omega L_\mathrm{Z}$. In the local density approximation the energy of the rotating configuration at zero temperature can be written as

$$E = \int d\mathbf{r} \left[\epsilon(n) + V(\mathbf{r}) + \frac{1}{2} m v^2 - m\Omega(\mathbf{r} \times \mathbf{v})_\mathrm{Z} - \mu \right] n \ , \tag{3.15}$$

where $\epsilon(n)$ is the energy density per particle, $\mathbf{v}$ the velocity field, μ the chemical potential and n the density.

By terming $R_\mathrm{S}(\theta, \phi)$ the interface separating the superfluid from the normal component, the integral in Eq.(3.15) splits in two parts. The internal superfluid core occupies the region $r < R_\mathrm{S}(\theta, \phi)$ and the surrounding normal phase is confined to $R_\mathrm{S}(\theta, \phi) < r < R_\mathrm{N}(\theta, \phi)$, where $R_\mathrm{N}(\theta, \phi)$ is the Thomas-Fermi radius of the gas where the density vanishes. The energy densities in the two phases are given by

$$\epsilon_\mathrm{S} = \xi_\mathrm{S} \frac{3}{5} \frac{\hbar^2}{2m} (6\pi^2 n_\mathrm{S})^{2/3}, \tag{3.16}$$

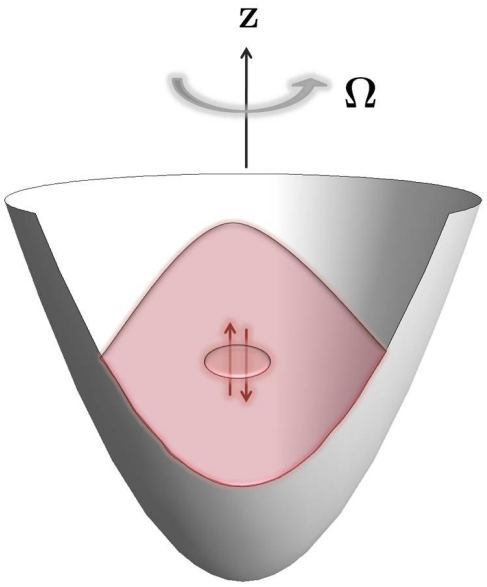

Figure 3.11: Sketch of an unpolarized Fermi superfluid in a trap rotating with angular velocity Ω around its z-axis.

$$\epsilon_{\mathrm{N}} = \xi_{\mathrm{N}} \frac{3}{5} \frac{\hbar^2}{2m} (6\pi^2 n_{\mathrm{N}})^{2/3}, \tag{3.17}$$

where n_{S} (n_{N}) is the superfluid (normal) density and the dimensionless parameters $\xi_{\mathrm{S}} = 0.42$ and $\xi_{\mathrm{N}} = 0.56$ account for the role of interactions in the two phases. Their value has been calculated in [82, 83] employing Quantum Monte Carlo simulations.

The equilibrium is found by minimizing the energy with respect to the densities and the velocity fields of the superfluid and normal part, as well as with respect to the position of the border surface. Notice that this picture ignores surface tension effects, a plausible assumption in the limit of large samples. The superfluid velocity obeys the irrotationality constraint and can be written as $\mathbf{v}_{\mathrm{S}} = \nabla\Phi$. Varying the energy with respect to the velocity potential Φ yields the continuity equation

$$\nabla \cdot ((\nabla\Phi - \mathbf{\Omega} \times \mathbf{r}) n_{\mathrm{S}}) = 0, \tag{3.18}$$

while variation with respect to the superfluid density n_{S} leads to

$$\mu = \xi_{\mathrm{S}} \frac{\hbar^2}{2m} (6\pi^2 n_{\mathrm{S}})^{2/3} + V^{\mathrm{S}}(\mathbf{r}), \tag{3.19}$$

where $V^{\rm S}(\mathbf{r}) = V(\mathbf{r}) + \frac{1}{2}mv_{\rm S}^2 - m\Omega(\mathbf{r}\times\mathbf{v}_{\rm S})_{\rm Z}$ is the effective harmonic potential felt by the superfluid.

Using the same procedure for the normal part without the irrotationality constraint we have $\mathbf{v}_N = \mathbf{\Omega}\times\mathbf{r}$, i.e. the normal component rotates rigidly. The variation with respect to the normal density yields an equation similar to (3.19)

$$\mu = \xi_{\rm N}\frac{\hbar^2}{2m}(6\pi^2 n_{\rm N})^{2/3} + V^{\rm N}(\mathbf{r}), \tag{3.20}$$

where the effective harmonic potential $V^{\rm N}(\mathbf{r})$ is now quenched by the rigid rotation according to $(\omega_x^{\rm N})^2 = \omega_x^2 - \Omega^2$, $(\omega_y^{\rm N})^2 = \omega_y^2 - \Omega^2$.

By varying the energy (3.15) with respect to $R_{\rm S}(\theta,\phi)$ we eventually find the equilibrium condition for the coexistence of the two phases in the trap. The resulting equation implies that the pressure of the two phases be the same: $n_{\rm S}^2(\partial\epsilon_{\rm S}/\partial n_{\rm S}) = n_{\rm N}^2(\partial\epsilon_{\rm N}/\partial n_{\rm N})$. Using Eqs.(3.16) and (3.17), one then predicts a density discontinuity at the interface given by

$$\frac{n_{\rm N}}{n_{\rm S}} = \gamma \quad \text{with} \quad \gamma = \left(\frac{\xi_{\rm S}}{\xi_{\rm N}}\right)^{3/5} = 0.85 \tag{3.21}$$

independent of the angular velocity. The equal pressure condition (3.21) combined with Eqs.(3.19) and (3.20), results in the useful relationship

$$(\mu - V^{\rm S}(\mathbf{r})) = \gamma(\mu - V^{\rm N}(\mathbf{r})), \tag{3.22}$$

which determines the surface $R_{\rm S}(\theta,\phi)$ separating the superfluid and the normal part.

Results

In the following we assume $\omega_x = \omega_y \equiv \omega_\perp$ and we consider the solution $\mathbf{v}_{\rm S} = 0$, corresponding to a non rotating axi-symmetric superfluid and hence to $V^{\rm S} = V$. In this case we find

$$R_{\rm S}^2(\theta) = \frac{2\mu}{m}\left(\omega_z^2\cos^2\theta + \omega_\perp^2\sin^2\theta + \frac{\gamma}{1-\gamma}\Omega^2\sin^2\theta\right)^{-1}, \tag{3.23}$$

where θ is the polar angle. On the other side the Thomas-Fermi radius $R_{\rm N}$ of the normal gas is fixed by the condition $\mu = V^{\rm N}$ yielding

$$R_{\rm N}^2(\theta) = \frac{2\mu}{m}\left(\omega_z^2\cos^2\theta + \omega_\perp^2\sin^2\theta - \Omega^2\sin^2\theta\right)^{-1} \geq R_{\rm S}^2(\theta)\ . \tag{3.24}$$

The value of μ is fixed by the normalization condition

$$\int_{r<R_{\rm S}(\theta)} n_{\rm S}\ d\mathbf{r} + \int_{R_{\rm S}(\theta)<r<R_{\rm N}(\theta)} n_{\rm N}\ d\mathbf{r} = N\ , \tag{3.25}$$

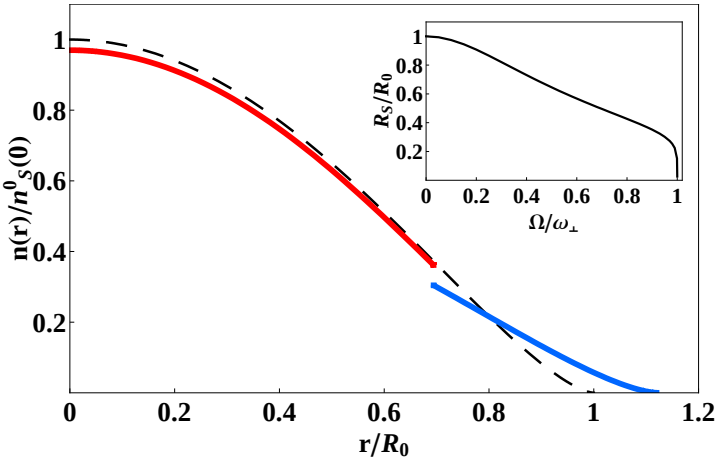

Figure 3.12: Density profile for $\theta = \pi/2$ of the rotating Fermi gas at $\Omega = 0.45\omega_\perp$ (full line). The profile in the absence of rotation is also shown (dashed line). Inset: Superfluid radius versus $\Omega/\omega_\perp$.

where N is the total number of particles.

While for $\Omega = 0$ the system is completely superfluid, for $\Omega > 0$ it phase separates into a superfluid and a normal component characterized by the density jump Eq.(3.21) at the interface. This behavior shares interesting analogies with the the phase separation between a superfluid and a normal component exhibited by polarized Fermi gases [46, 47, 50, 63], where a jump in the density at the interface is also predicted to occur [59, 91]. By tomographic techniques [63] it is nowadays possible to measure the density *in situ*, thus the predicted discontinuity, and hence the value of ξ_S/ξ_N, should be observable experimentally.

The radii R_S and R_N coincide at $\theta = 0$ which means the absence of the normal part along the z-axis. In the plane of rotation ($\theta = \pi/2$) the difference between the two radii is instead maximum and becomes larger and larger as Ω increases. In particular the radius of the superfluid is always smaller than the radius of the cloud in the absence of rotation, while the radius of the normal gas is always larger due to the bulge effect produced by the rotation.

In Fig. 3.12 we plot the densities n_S and n_N as a function of the radial coordinate at $\theta = \pi/2$ in a spherical trap for $\Omega = 0.45\omega_\perp$. The densities and the radial coordinate have been renormalized with respect to the central density n_S^0 and the Thomas-Fermi radius R_0 of the superfluid at rest. The inset shows the superfluid radius R_S renormalized by R_0 as a function of the angular velocity $\Omega/\omega_\perp$. The jump in the densities between the superfluid and the normal part is exhibited as a knee in the total density of the gas (Fig. 3.13), reflecting the density discontinuity produced by the rotation [79]. Fig. 3.12 shows again that near the rotational axis the system prefers to remain superfluid, while beyond a certain distance due

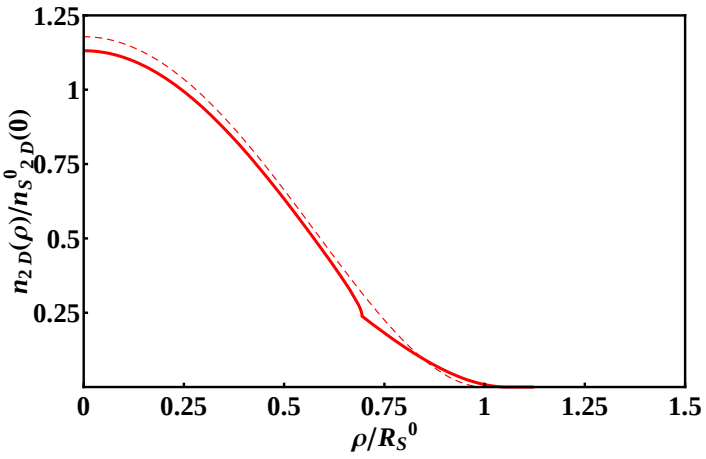

Figure 3.13: Total column density of the unpolarized system in a spherical harmonic trap for $\Omega = 0$ (dashed red line, superfluid at rest). For $\Omega = 0.45\omega_\perp$ the system consists of a superfluid core surrounded by a normal shell where $n_\uparrow = n_\downarrow$.

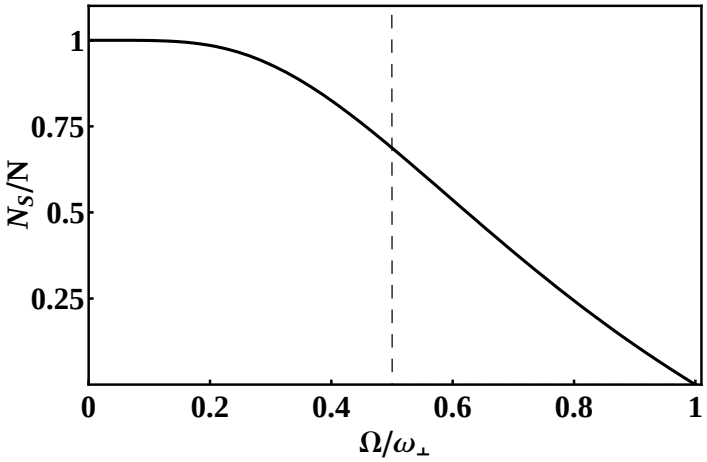

Figure 3.14: Depletion of the superfluid as a function of the trap angular velocity for an axi-symmetric configuration.

to the centrifugal energy gain by breaking pairs the system becomes normal.

From the knowledge of the density profiles and from the radii Eqs.(3.23) and (3.24) we can calculate the number of particles in each phase. In Fig. 3.14 we show the ratio between the number of particles N_S in the superfluid phase and the total number N as function of the angular velocity. The higher the angular velocity, the more particles prefer to stay in the normal phase and thus the superfluid is depleted. At small angular velocities the depletion of the superfluid follows the law $N_\mathrm{S}/N = 1 - \left(\frac{\gamma}{1-\gamma}\right)^{5/2} \Omega^5$, where $\left(\frac{\gamma}{1-\gamma}\right)^{5/2} \Omega^5 = N_\mathrm{N}/N$ corresponds to the

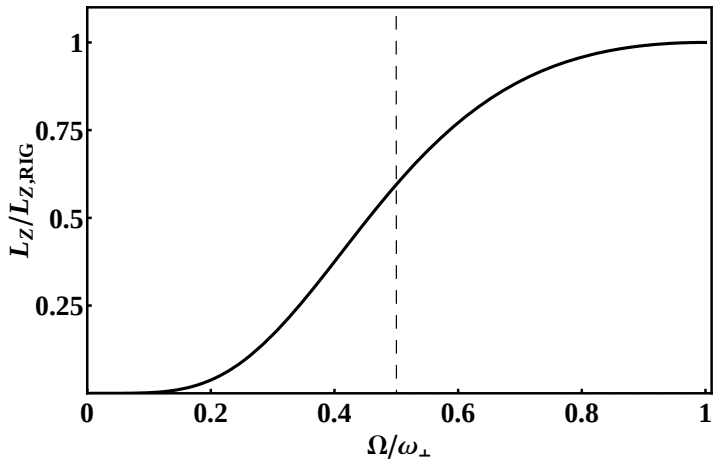

Figure 3.15: Angular momentum in units of the rigid value as a function of the trap angular velocity for an axi-symmetric configuration.

particle number in the normal part.

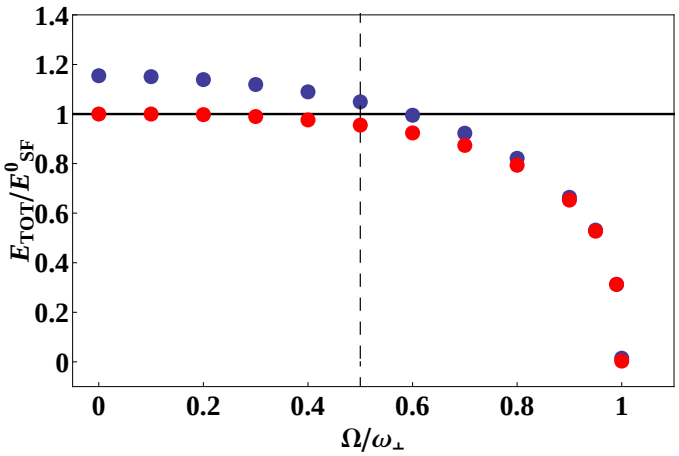

Figure 3.16: Total energy of the phase separated system in the rotating frame (red points), normalized by the energy of a superfluid at rest. As a comparison, we show the energy if the system was only normal (blue points).

Another important observable is the angular momentum L_Z. For an axi-symmetric configuration the superfluid does not carry angular momentum which is then provided only by the normal component: $L_Z = \Omega \int d\mathbf{r}\ (x^2 + y^2) n_N$. The total angular momentum then increases with Ω and eventually reaches the rigid body value at $\Omega = \omega_\perp$ (see Fig. 3.15). At small angular velocities the angular momentum follows the law $L_Z = \pi \left(\frac{4096}{525}\right) \left(\frac{\gamma}{1-\gamma}\right)^{5/2} \Omega^5$ and it goes to zero for

$\Omega \to 0$. This corresponds to the case of BEC's, where the moment of intertia is zero for a symmetric configuration as $\Omega \to 0$.

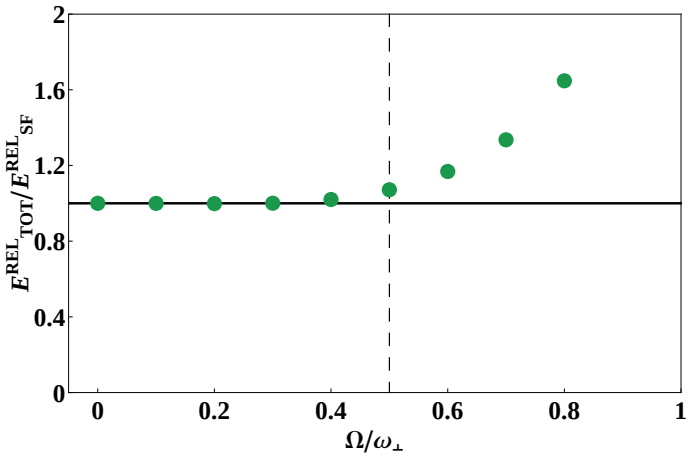

Figure 3.17: Release energy of the phase separated system, normalized by the release energy of a solely superfluid system. This is the energy which can be experimentally measured after switching off the trap.

The angular momentum of a rotating configuration has been measured in BEC's by studying the precession phenomena exhibited by the surface excitations [104]. While for small values of the angular velocity ($\Omega < 0.2\omega_\perp$) the superfluid is robust, it is remarkable that even at angular velocities far from the centrifugal limit the depletion of the superfluid and hence the angular momentum of the system are sizable.

In Fig. 3.16 we plot the total energy of the system (red points) in the rotating frame as well as the total energy of the system as it would consists of the normal part only (blue points). The higher energy of the solely normal system for $\Omega = 0$ proofs that the superfluid is the more favourable state at unitarity. Eventually as $\Omega \to \omega_\perp$, the two energies begin to converge since the superfluid is depleted, until at $\Omega = \omega_\perp$ they fully overlap.

In most experiments with ultracold atomic gases, absorption images taken after the cloud has been released from the trap provide valuable information about the equation of state of the system. An experimentally measurable quantity is hence the release energy, i.e. the energy of the system after the external trap is switched off, and is simply given by

$$E_{\mathrm{rel}} = \int d\mathbf{r}\ \epsilon[n(\mathbf{r})] \tag{3.26}$$

where $\epsilon[n(\mathbf{r})]$ is the energy density. It is the sum of the kinetic and the interaction

energy $E_{\rm rel} = E_{\rm kin} + E_{\rm int}$, and in our case, the kinetic energy comes only from the rigidly rotating normal part.

If the system would not phase separate, the release energy would be the internal energy of a fully superfluid system for any value of Ω. But since the superfluid depletes and the normal part can carry angular momentum, the kinetic energy term becomes finite, hence the release energy increases with Ω and eventually diverges for $\Omega \to \omega_\perp$. This can be nicely seen in Fig. 3.17, where we plot the relase energy of the system for $0 \leq \Omega \leq \omega_\perp$ (green points) in units of the relase energy of an entirely superfluid system.

It is worth mentioning that at large enough angular velocities the system exhibits solutions which break the axial symmetry [99]. Such a critical value is predicted to be $\Omega_{\rm cr} \sim 0.5\omega_\perp$ as we will show in detail in chapter 4. The results in Figs. 3.14 - 3.17 for $\Omega > 0.5\omega_\perp$ (dashed vertical line) correspond to the axial symmetric solution of the problem.

Conclusions

Trapped superfluid Fermi gases can behave quite differently from BEC's because pairs are easily broken by the rotation. While at small angular velocities the superfluid is unaffected by the rotation of the trap [105], at higher angular velocities the rotation results in a phase separation between a non rotating superfluid core and a rigidly rotating normal component. The mechanism of pair breaking is very intuitive. In fact near the border of the cloud, where the density n is small, the energy cost for destroying superfluidity is also small, being proportional to $n^{2/3}$. Vice versa the centrifugal energy gained by the normal phase can be large, being proportional to $\Omega^2 R^2$ where R is the radius of the cloud. Notice that this mechanism cannot occur in the BEC regime due to the high energy cost needed to break the dimers.

Furthermore, differently from the nucleation of vortices, the formation of the normal part is not inhibited by the presence of a barrier as all the relevant energy scales are vanishingly small near the border and the energy gain is ensured as soon as one starts rotating the trap. The appearance of a normal part due to rotation is not peculiar of ultra-cold atomic Fermi gases. For example, superfluidity is known to be unstable in nuclei rotating with high angular velocity [95]. Such an effect is also related to the so-called intermediate state in type-I superconductors, where the role of the rotation is played by the external magnetic field (see, e.g., [106]).

The formation of the rotating normal component requires that the trap transfers angular momentum to the gas within experimentally accessible times. Its realization would open the unique possibility of exploring the Fermi liquid behaviour

of a strongly interacting gas at zero temperature. Important effects to investigate are, for example, the zero sound nature of the collective oscillations and the behaviour of viscosity.

Finally, let us briefly argue on the possibility of having a rotating system without vortices in the superfluid, which is the main assumption of the present work. If the vortices could enter the superfluid, the lowest energy configuration would not be the one discussed here, but rather a superfluid core with vortices surrounded by a rotating normal shell, as also experimentally seen in [45]. We expect that there exists a barrier for a vortex to enter the superfluid, as happens for a BE condensate. The interface caused by the fermions in the normal state could however change the scenario. On the one hand, the phase separation in the trap should disfavor the vortex formation as the superfluid density is finite at the interface. On the other hand, since there is a relative velocity between the superfluid and the normal shell, vortex nucleation could be favoured by a Kelvin-Helmoltz-like mechanism. Moreover, we have shown that the interface reduces the critical angular velocity for a quadrupole instability. In the BEC case the latter is considered as a route toward vortex formation [101]. In the end, more theoretical and experimental work is needed to enlighten the issue of vortex nucleation in these systems.

3.3 Comparison with a BCS-like Theory at Unitarity

In our work we have assumed that the system phase separates in only two phases. This assumption works well for the experiments carried out so far [60]. However, in the rotating case other phases could appear as shown in a microscopic description within the framework of BCS theory by Urban and Schuck [102] and by Iskin and Tiesinga [107]. Here we will give a brief summary of the work by Urban and Schuck.

In [102] the authors study the pair breaking effect in a unitary Fermi superfluid in the BCS-BEC crossover at zero temperature by solving selfconsistently the gap- and number equations with the cranking term ΩL_{Z}. This leads to solutions which describe *three* distinct regions which the authors term (A), (B), and (C). Region (A) describes the region near the rotational axis where the superfluid is at rest, as in our case. In region (B) pairs are gradually broken, starting from the superfluid edge of region (A) towards the edge of region (B), which verges on region (C). Hence the further away from the rotational axis, the more pairs are broken until in region (C) the pairs are completely broken and the system can rotate rigidly. The emergent phase (B) is absent in our macroscopic description and implicates that the density for a finite angular velocity $\Omega/\omega_{\perp}$ is void of any discontinuities.

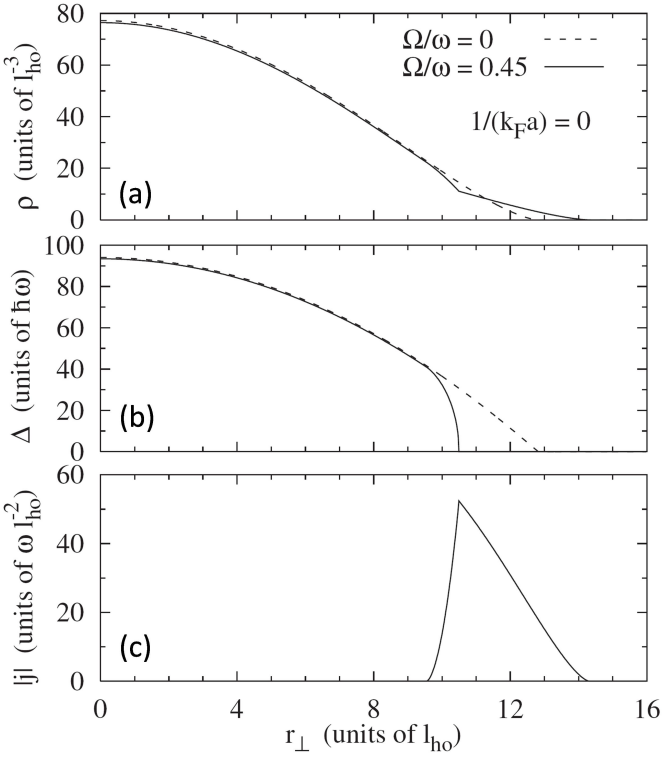

Figure 3.18: (a) Density per spin state ρ, (b) gap Δ, and (c) current $|\mathbf{j}|$ in a rotating unitary Fermi gas within the BCS description as functions of the distance $r_\perp$ from the z-axis. The solid line shows the nonrotating case, while the dashed line corresponds to $\Omega = 0.45\omega_\perp$. Courtesy Michael Urban and [102].

The authors calculate the density ρ, the gap Δ, and the current $|\mathbf{j}|$ of the adiabatically rotating unitary Fermi gas for $\Omega = 0$ and $\Omega = 0.45\omega_\perp$ as shown in Fig. 3.18 [102]. They also find that for a finite angular velocity Ω the system exhibits the bulge effect of the rotation (Fig. 3.18 (a)): in the z-direction size of the system decreases, while the radial size increases. The visible kink in the density profile is attributed to the reduced chemical potential and hence to the decrease of the gap Δ in the centre of the trap (see Fig. 3.18 (b)). The particle current $|\mathbf{j}|$ (see (Fig. 3.18 (c)) remains a continuous function in the intermediate region (B) caused by the rotation, and has its maximum at the position of the kink in the density.

In the case of the microscopic treatment of Urban and Schuck the density ρ remains continuous. This is different from our prediction, where the phase separation between a fully paired superfluid and a fully unpaired normal phase leads to a density discontinuity characterized by Eq.(3.21) in the radial profile as shown in Fig. 3.12. The region (B) found in [102], which consists of both paired and unpaired particles, is a direct consequence of the nonvanishing current $|\mathbf{j}|$. Would

this current be absent, the jump in the density would be characterized by the BCS value $\rho_{\mathrm{N}}/\rho_{\mathrm{S}} = \xi_{\mathrm{S}}^{\mathrm{BCS}}/\xi_{\mathrm{N}}^{\mathrm{BCS}} = 0.73$.

4 Quadrupole Instability induced by Rotation

In chapter 3 we have shown that the effect of the rotation applied to polarized Fermi gas at unitarity is to enhance the Chandrasekhar-Clogston limit, while in the unpolarized case it causes a phase separation between a superfluid core and an unpolarized outer shell.

A major issue concerns the conditions of stability of the rotating configuration discussed in this work. Let us first consider the question of energetic stability. We have shown that in the frame rotating with the trap, the phase separated configuration is energetically favoured with respect to the configuration where the whole gas is at rest and superfluid. This is true for any value of the angular velocity.

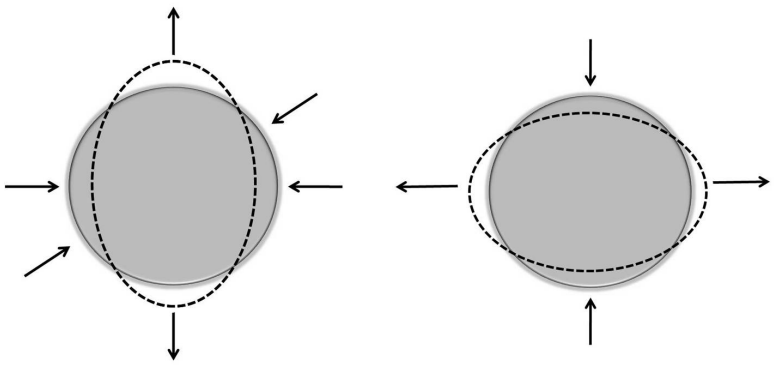

Figure 4.1: Sketch of the shape deformation due to excitation of the quadrupole mode in a Bose-Einstein condensate.

When Ω exceeds a critical value of order $(\hbar/mR^2)\ln(R/d)$, where d is the healing length fixed, at unitarity by the interparticle distance, quantized vortices become an even more favourable configuration. This energetic instability is not however expected to be a severe difficulty if one increases the angular velocity in an adiabatic way because the presence of a barrier inhibits the access to the vortical configuration as proven experimentally in the case of BEC's [108].

A further important effect is the spontaneous breaking of axi-symmetry. In fact, one expects that above a certain critical value $\Omega_{\rm cr}$ the system exhibits a surface energetic instability, undergoing a continuous shape deformation, similarly to what happens in Bose-Einstein condensates [99, 101, 103] as shown in Figs.4.1 and 4.2. This effect is accounted for by the solution $\mathbf{v}_{\rm S} \neq \mathbf{0}$ of Eq.(3.18) which becomes energetically favorable above $\Omega_{\rm cr}$.

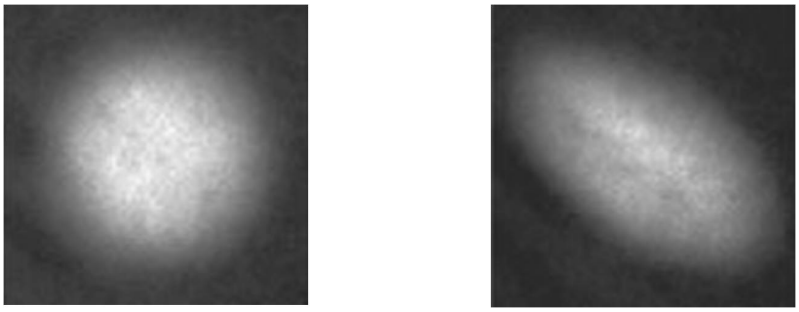

Figure 4.2: Absorption image of the quadrupole oscillation of a Bose-Einstein condensate, [101].

In the case of Bose-Einstein condensates the quadrupole instability occurs at $\Omega_{\rm cr} = \omega_\perp/\sqrt{2}$ when the $\omega = \sqrt{2}\omega_\perp$ hydrodynamic quadrupole mode becomes energetically unstable in the rotating frame. The value $\Omega = \sqrt{2}\omega_\perp$ applies in the Thomas-Fermi regime. In a more general case, one has to solve the Gross-Pitaevskii equation [109].

For larger values of Ω the solution $\mathbf{v}_{\rm S} = 0$ corresponds to the so called overcritical branch [99]. If one ignores the effect of phase separation taken into account the spontaneous breaking of axial symmetry in rotating Fermi gases would take place at the same value as in the BEC case as shown by G. Tonini *et al.* [110].

A different value is predicted to occur for the rotating Fermi gas however due to the new boundary conditions imposed by the presence of the normal component. In fact, the current of the superfluid, in the rotating frame, should be tangential to the interface where the density, differently from the Bose-Einstein condensate case, does not vanish. In the following we will determine the value of the critical velocity in the simplest case of a rotating unpolarized gas and we will consider the onset of a quadrupole deformation.

4.1 Conditions for the Quadrupole Instability

We consider an axially symmetric potential $\omega_x = \omega_y = \omega_\perp \neq \omega_z$ and a solution where axi-symmetry is spontaneously broken. This is associated with the appear-

ance of a non vanishing velocity field in the superfluid component whose velocity potential will be chosen of the form

$$\Phi = xyf(r^2, z^2), \tag{4.1}$$

where f is an arbitrary function of $r^2 = x^2 + y^2$ and of z^2. Note that in the case of the quadrupole instability of a Bose-Einstein condensate an exact stationary solution is found with f =const.

The value of $\Omega_{\rm cr}$ corresponds to the onset of solutions with a deformed configuration. It is determined by solving the continuity equation in the rotating frame

$$\nabla \cdot [(\nabla\Phi - \mathbf{\Omega} \times \mathbf{r})n_{\rm S}(\mathbf{r})] = 0, \tag{4.2}$$

where $n_{\rm S}(\mathbf{r})$ is now no longer axi-symmetric, and by imposing that the superfluid current be tangential to the boundary $B(\mathbf{r})$ of the superfluid

$$(\nabla\Phi - \mathbf{\Omega} \times \mathbf{r}) \cdot \nabla B(\mathbf{r}) \Big|_{r=R_{\rm S}} = 0. \tag{4.3}$$

The density, in the local density approximation, is given by

$$n_{\rm S}(\mathbf{r}) = \frac{1}{\xi_{\rm S}} \frac{1}{6\pi^2} \left(\frac{2m}{\hbar^2}\right)^{3/2} (\mu - V^{\rm S}(\mathbf{r}))^{3/2}, \tag{4.4}$$

where $V^{\rm S}(\mathbf{r}) = V(\mathbf{r}) + \frac{1}{2}mv_{\rm S}^2 - m\Omega(\mathbf{r} \times \mathbf{v}_{\rm S})_{\rm Z}$ is the effective harmonic potential felt by the superfluid. By expanding the external potential to first order in f as

$$V^{\rm S}(\mathbf{r}) = V(\mathbf{r}) + \delta V^{\rm S}(\mathbf{r}) \tag{4.5}$$

with

$$\delta V^{\rm S}(\mathbf{r}) = -m\nabla\Phi(\mathbf{\Omega} \times \mathbf{r}), \tag{4.6}$$

one finds

$$n_{\rm S}(\mathbf{r}) = (\mu - V(\mathbf{r}))^{3/2} - \frac{3}{2}(\mu - V(\mathbf{r}))^{1/2} \cdot \delta V^{\rm S}(\mathbf{r}). \tag{4.7}$$

At the same time the border can be written as $B(\mathbf{r}) = B^0(\mathbf{r}) + \delta B(\mathbf{r})$, where $B^0(\mathbf{r})$ is the radius of the superfluid given by

$$R_{\rm S}^2(\theta) = \frac{2\mu}{m} \left(\omega_z^2 \cos^2\theta + \omega_\perp^2 \sin^2\theta + \frac{\gamma}{1-\gamma}\Omega^2 \sin^2\theta\right)^{-1}, \tag{4.8}$$

and

$$\delta B(\mathbf{r}) = -m\nabla\Phi \cdot (\mathbf{\Omega} \times \mathbf{r}) \tag{4.9}$$

is the linear perturbation due to the quadrupole symmetry breaking.

Then, Eqs.(4.2) and (4.3) reduce to

$$(\mu - V(\mathbf{r}))\Delta\Phi + \frac{3}{2}(\nabla\delta V^{\mathrm{S}}(\mathbf{r}))\cdot(\mathbf{\Omega}\times r) - \frac{3}{2}\nabla V(\mathbf{r})\cdot\nabla\Phi = 0, \tag{4.10}$$

and

$$\nabla\Phi\cdot\nabla B_0(\mathbf{r}) - (\mathbf{\Omega}\times r)\cdot\nabla\delta B(\mathbf{r})\,\Big|_{r=R_{\mathrm{S}}(\theta)} = 0. \tag{4.11}$$

By inserting the explicit expressions of the respective functions in Eqs.(4.10) and (4.11), after some straightforward algebra we obtain

$$(2\Omega^2-1)f + \frac{2}{3}(1-r^2-z^2)(r^2 f_{\mathrm{rr}} + z^2 f_{\mathrm{zz}}) + (2-3r^2-2z^2)f_{\mathrm{r}} + \frac{1}{3}(1-r^2-4z^2)f_{\mathrm{z}} = 0, \tag{4.12}$$

and

$$\Big(\,[1-\gamma(1-\Omega^2)-2\Omega^2]f + [1-\gamma(1-\Omega^2)]r^2 f_{\mathrm{r}} + (1-\gamma)z^2 f_{\mathrm{z}}\,\Big)\times (1-r^2-z^2)^{3/2}\;\Big|_{r=R_{\mathrm{S}}(\theta)} = 0, \tag{4.13}$$

where the latter equation is evaluated at the interface Eq.(4.8). In Eqs.(4.12, 4.13) $f_{\mathrm{r(z)}}$ is the first derivative of f with respect to r (z), $f_{\mathrm{rr(zz)}}$ the second, and the expressions have been renormalized with respect to the radius of a superfluid at rest $(R_{\mathrm{S}}^0)^2 = 2\mu/m\omega_\perp^2$ and we have made the substitution $\Omega/\omega_\perp \to \Omega$ and the assumption $\omega_z = \omega_\perp$.

4.2 Critical Angular Velocity in Two Dimensions

In the case of a two-dimensional system ($R_{\mathrm{S}}(\theta) \equiv R_{\mathrm{S}}$) the previous equations can be easily solved. In this case indeed Eqs.(4.12) and (4.13) reduce to

$$(2\Omega^2-1)f(r^2) + (2-3r^2)f_{\mathrm{r}}(r^2) + \frac{2}{3}(1-r^2)r^2 f_{\mathrm{rr}}(r^2) = 0, \tag{4.14}$$

and

$$[1-\gamma(1-\Omega^2)-2\Omega^2]f(r^2) + [1-\gamma(1-\Omega^2)]r^2 f_{\mathrm{r}}(r^2)\;\Big|_{r=R_{\mathrm{S}}} = 0, \tag{4.15}$$

the latter being evaluated at

$$R_{\mathrm{S}}^2 \equiv \frac{(1-\gamma)}{[1-\gamma(1-\Omega^2)]}. \tag{4.16}$$

The solutions of the continuity equation Eq.(4.14) are hypergeometric functions ${}_2F_1(a_{2D}, b_{2D}, c_{2D}; r^2)$ [111], with the coefficients a_{2D}, b_{2D} and c_{2D} given by

$$\begin{aligned} a_{2D} &= \frac{7}{4} - \frac{1}{4}\sqrt{25+48\Omega^2}, \\ b_{2D} &= \frac{7}{4} + \frac{1}{4}\sqrt{25+48\Omega^2}, \\ c_{2D} &= 3. \end{aligned} \tag{4.17}$$

Inserting these solutions in the boundary condition (4.15), we find the value $\Omega_{cr} = 0.45\omega_\perp$ for the emergence of a spontaneous quadrupole deformation in two dimensions.

4.3 Critical Angular Velocity in Three Dimensions

For the three-dimensional case it is convenient to introduce spherical coordinates

$$\begin{aligned} r^2 &= \rho^2 \sin^2\theta, \\ z^2 &= \rho^2 \cos^2\theta. \end{aligned} \tag{4.18}$$

Then, the continuity equation (4.12) is given by

$$(1-\rho^2)\rho^2(\partial_{\rho^2})^2 + \frac{1}{2}(7-10\rho^2)\partial_{\rho^2} f + \frac{3}{2}(2\Omega^2-1)f + \frac{1-\rho^2}{4\rho^2}\left[\partial_\theta^2 + 5\left(\frac{\cos\theta}{\sin\theta}\right)\partial\theta\right] f = 0, \tag{4.19}$$

while the condition that the current be tangential to the superfluid border (4.13) is rewritten as

$$\left([1-\gamma(1-\Omega^2)-2\Omega^2]f + (1-\gamma)\partial_{\rho^2} f + \frac{\gamma\,\Omega^2}{2}\sin\theta\cos\theta\;\partial_\theta f\right) \times \left(1 - \frac{1-\gamma}{1-\gamma(1-\Omega^2\sin^2\theta)}\right)^{3/2} \Big|_{r=R_S(\theta)} = 0, \tag{4.20}$$

the latter being evaluated at

$$R_S^2(\theta) \equiv \frac{(1-\gamma)}{[1-\gamma(1-\Omega^2\sin^2\theta)]}. \tag{4.21}$$

As in the 2D case, we first have to solve the continuity equation in order to obtain the solutions, which are then used to calculate the critical angular velocity from Eq.(4.20). Since we can not solve the problem exactly, we will use some

approximations. First we make use of the separation ansatz $f = R(\rho^2)\Theta(\theta)$ to find the solution for the the continuity equation (4.19). This yields

$$\frac{1}{R}\left(\frac{4\rho^2}{1-\rho^2}\right)\left[(1-\rho^2)\rho^2 R^{''} + \frac{1}{2}(7-10\rho^2)R^{'} + \frac{3}{2}(2\Omega^2-1)R\right] = -\frac{1}{\Theta}\left[\Theta^{''} + 5\left(\frac{\cos\theta}{\sin\theta}\right)\Theta^{'}\right], \tag{4.22}$$

where for the sake of readability we have used $R(\rho^2) \equiv R$ and $\Theta(\theta) \equiv \Theta$, and have divided by R and Θ.

This is an eigenvalue problem which can be solved by setting the left hand side of Eq.(4.22) to correspond to an eigenvalue A, and eventually we get

$$(1-\rho^2)\rho^2 R^{''} + \frac{1}{2}(7-10\rho^2)R^{'} + \left[\frac{3}{2}(2\Omega^2-1) + \left(\frac{1-\rho^2}{4\rho^2}\right)A\right]R = 0. \tag{4.23}$$

The solution of this equation is given by

$$R(\rho^2, A, \Omega) = (\rho^2)^q \; {}_2F_1(a_{3\mathrm{D}}, b_{3\mathrm{D}}, c_{3\mathrm{D}}; \rho^2), \tag{4.24}$$

where $q = (-5 + \sqrt{25-4A})$ and ${}_2F_1(a_{3\mathrm{D}}, b_{3\mathrm{D}}, c_{3\mathrm{D}}; \rho^2)$ are the hypergeometric functions [111] with

$$\begin{aligned} a_{3\mathrm{D}} &= \frac{3}{4} + \frac{1}{4}\sqrt{25-4A} - \frac{1}{2}\sqrt{10-A+12\Omega^2}, \\ b_{3\mathrm{D}} &= \frac{3}{4} + \frac{1}{4}\sqrt{25-4A} + \frac{1}{2}\sqrt{10-A+12\Omega^2}, \\ c_{3\mathrm{D}} &= 1 + \frac{1}{2}\sqrt{25-4A}. \end{aligned} \tag{4.25}$$

The same way we solve the equation for Θ, where now we set the right hand side of Eq.(4.22) to correspond to the eigenvalue A leading to

$$\sin\theta\;\Theta^{''} + 5\cos\theta\;\Theta^{'} + A\;\theta\sin\theta = 0. \tag{4.26}$$

The solutions of the equation for Θ

$$\Theta(A, \theta) = \frac{P_n^m(x)}{(\cos^2\theta - 1)}, \tag{4.27}$$

where $P_n^m(x)$ are the associated Legendre polynomials with

$$\begin{aligned} n &= -\frac{1}{2} + \frac{1}{2}\sqrt{25+4A}, \\ m &= 2, \\ x &= \cos\theta. \end{aligned} \tag{4.28}$$

We can now write down the complete solution of the continuity equation as

$$\begin{aligned} f(\rho^2, A, \Omega, \theta) &= R(\rho^2, A, \Omega)\ \Theta(A, \theta) \\ &\equiv (\rho^2)^d\ {}_2F_1(a_{3\mathrm{D}}, b_{3\mathrm{D}}, c_{3\mathrm{D}}; \rho^2)\ \left(\frac{P_n^m(x)}{\cos^2\theta - 1}\right), \end{aligned} \tag{4.29}$$

which can be used in Eq.(4.20) at $\rho^2 \equiv R_{\mathrm{S}}^2(\theta)$ to find the critical angular velocity $\Omega_{\mathbf{cr}}$ for the onset of the quadrupole instability in three dimensions.

For the solution we lack the exact value of A, however, by requiring that the coefficients in Eq.(4.25) be real, we can narrow down the possible values for A to the range $-4 < A < 0$. On the other hand, the condition, that the velocity of the superfluid be tangential to the border $R_{\mathrm{S}}(\theta)$ corresponds to the physical condition, that the *current* of the superfluid be zero, and so $|\mathbf{v} \cdot \mathbf{n}_{\mathrm{B}}|\ n_{\mathrm{S}}(R_{\mathrm{S}}(\theta)) \equiv j = 0$, where $\mathbf{n}_{\mathrm{B}}$ is the normal vector and $n_{\mathrm{S}}(R_{\mathrm{S}}(\theta))$ the superfluid density at the border.

Then, eventually, within a variational approach we can formulate the condition that for a certain value of Ω the normalized expectation value of the current $\hat{J}$ be zero,

$$\hat{J} = \frac{2\pi\ \int d\theta \left(\sqrt{(\int dA\ C_{\mathrm{A}}\ T_{\mathrm{A}})^2}\right)^d n_{\mathrm{S}}(R_{\mathrm{S}}(\theta))}{\int d\theta \left(\sqrt{(\int dA\ C_{\mathrm{A}}\ \nabla\Phi)^2}\right)^d n_{\mathrm{S}}(R_{\mathrm{S}}(\theta))} = 0, \tag{4.30}$$

where d=1,2 and C_{A} are optimization coefficients, Φ is the velocity field Eq.(4.1), and T_{A} is the abbreviation for Eq.(4.20).

The results of the numerical calculation yield the estimate $\Omega_{\mathrm{cr}} \sim 0.5\omega_\perp$ for the critical angular velocity in three dimensions. Notice that both in two and three dimensions the critical velocity is predicted to be smaller than the value $\Omega_{\mathrm{cr}} = \omega_\perp/\sqrt{2}$ holding in the BEC case.

4.4 Conclusions

In conclusion we have addressed the question of quadrupole instability of the superfluid core, which produces a spontaneous breaking of axial symmetry of the cloud. The critical frequency for the onset of the instability turns out to be smaller than in the BEC case. Its measurement would provide a further crucial test of the mechanism of phase separation and of the equation of state of the normal phase [59, 60, 92].

An even more challenging question concerns the emergence of *dynamic* instabilities. In the case of a rotating BEC a dynamic instability takes place at values of Ω slightly larger than $\omega_\perp/\sqrt{2}$ and corresponds to the appearance of imaginary components in the frequency of some hydrodynamic modes [100]. In the case of

the rotating Fermi gas discussed in this work a dynamic instability might be associated with the Kelvin-Helmholtz instability of the interface between two fluids in relative motion (see.e.g [112]).

However, if the densities of the two fluids are different, at the interface, an external force stabilizes the two-fluid system against the appearance of complex frequencies in the low energy excitations of the interface [112]. This is actually our case where the density of the two phases exhibits the gap as in Eq. (3.21) and the system feels the external force produced by the harmonic confinement. We consequently expect that the system be dynamically stable at least for moderately small values of the angular velocity.

5 Phase Separation in Fermi Mixtures with Different Masses and Different Trapping

The recent observation of heteronuclear Feshbach resonances in ultracold mixtures of two fermionic species [66] as well as the realization of a degenerate two-species Fermi-Fermi mixture [67] opened new stimulating perspectives in the field of Fermi superfluids built with atomic species of different masses. Particular interest in these systems has arised due to the fact of the posibility to use component-selective trapping and the versatility of experiments.

The phase diagram of Fermi mixtures with unequal masses and the corresponding polarization effects, including possible occurrence of exotic phases such as the FFLO phase [70], have already been the object of theoretical predictions based on BCS mean-field theory [71–77]. This theory is known to give reasonable predictions at unitarity in the case of unpolarized configurations (see, e.g., [26]). However, it fails to give quantitatively correct results in the imbalanced case and to predict the Chandrasekhar-Clogston limit correctly. This failure is mainly due to the fact that it ignores the role of interactions in the normal phase which play a crucial role at unitarity [59, 60].

We use the equation of state for the normal phase as introduced in chapter 2 together with many-body results form diagrammatic and *ab initio* Monte Carlo calculations to analyze the effect of mass asymmetry on the phase separation from the normal to the superfluid state. We first discuss the Chandrasekhar-Clogston limit x_c and its properties in dependence on the mass ratio $m_\downarrow/m_\uparrow = \kappa$, after which we investigate the $\mu - h$ phase diagram. The local density approximation is then employed to predict the density profiles of the trapped gas, and we show that component-selective trapping can lead to many different configurations in the trapped case. The results presented in this chapter have been published in [113].

It is worth mentioning that the mass ratio κ cannot be neither too large nor too small in order to avoid instabilities due to the appearance of three-body bound states, see [114] and references therein.

5.1 Equation of State of the Unitary Fermi Gas with Unequal Masses

In the case of two atomic species (hereafter called spin-up and spin-down) with unequal masses, $m_\uparrow \neq m_\downarrow$, the equation of state as discussed in chapter 2 can be extended to hold also in the case of mass asymmetry. The form of the equation of state remains the same, with the only difference that the values of the parameters A and m^* can now depend on the mass ratio.

The generalization of Eq.(2.5) to the unequal mass case yields

$$\begin{aligned} \frac{E(x,\kappa)}{N_\uparrow} &= \frac{3}{5}E_{F\uparrow}\left(1 - A(\kappa)x + \frac{F(\kappa)^{-1}}{\kappa}x^{5/3} + B(\kappa)x^2\right) \\ &= \frac{3}{5}E_{F\uparrow}g(x,\kappa) \equiv \epsilon_{\mathrm{N}}(x,\kappa). \end{aligned} \tag{5.1}$$

The values of A and m^* have been calculated in [88] and [89] as functions of $m_\downarrow/m_\uparrow = \kappa$ using diagrammatic many-body techniques. The parameter A is an increasing function of κ, going to infinity for $\kappa \to 0$ and reaching the asymptotic value $A \sim 0.45$ for $\kappa \to \infty$ as shown in Fig. 5.1.

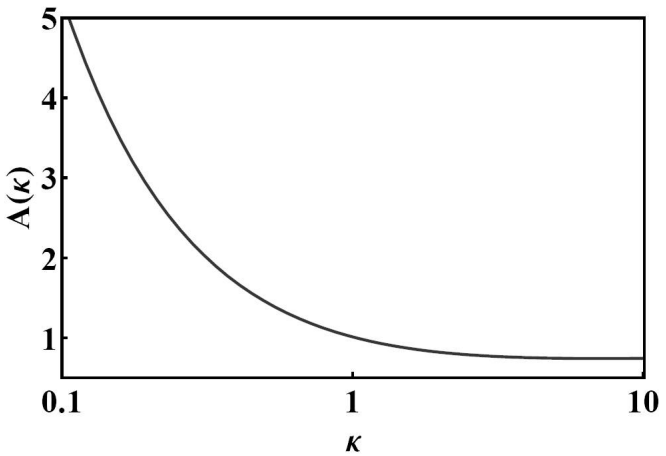

Figure 5.1: The binding energy $A(\kappa)$ as a function of κ as presented in [88].

On the other hand, at unitarity, the effective mass, which we will denote in the rest of the paper as $m^* = m_\downarrow F(\kappa)$, shows a weak dependence on the mass ratio (see Fig. 5.2).

The quasiparticle interaction B has up to now only been estimated for equal masses $m_\downarrow = m_\uparrow$. We can find an estimation for $B(\kappa)$ in the case $\kappa \neq 1$ in the

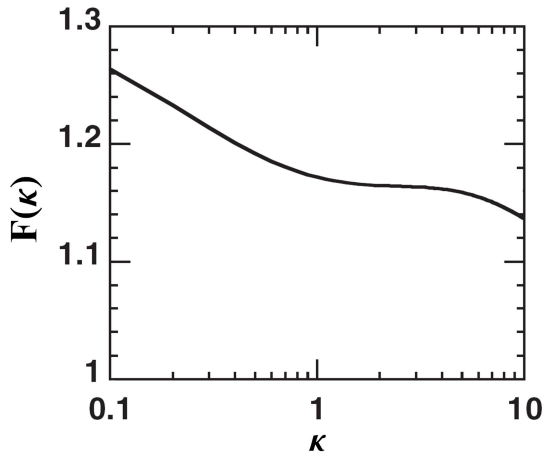

Figure 5.2: Relative effective mass $m^*/m_\downarrow = F(\kappa)$ as a function of the mass ratio κ at unitarity. From [88].

following way. In the unpolarized case ($x = 1$) the energy of the normal state as a function of κ has been calculated using Monte Carlo methods [82, 83], resulting in the expression

$$\frac{E_{\mathrm{N}}(\kappa)}{N_\uparrow} = \xi_{\mathrm{N}}(\kappa)\frac{3}{5}\frac{\hbar^2}{4m_\kappa}(6\pi^2 n_\uparrow)^{2/3} \equiv \epsilon(n_\uparrow, \kappa), \tag{5.2}$$

where the dimensionless parameter $\xi_{\mathrm{N}}(\kappa)$ accounts for the interactions, and $m_\kappa = (m_\uparrow m_\downarrow)/(m_\uparrow + m_\downarrow)$ is the reduced mass. First results based on quantum Monte Carlo (QMC) calculations suggest that the dependence of the interaction parameter $\xi_{\mathrm{N}}(\kappa)$ on κ is very weak [115] so that we can set $\xi_{\mathrm{N}}(\kappa) \equiv \xi_{\mathrm{N}} = 0.56$ [82, 83] also for $\kappa \neq 1$. Therefore the effect of unequal masses on the energy of the unpolarized normal state enters only through the reduced mass m_κ.

We can define B as a function of the mass ratio by requiring that the energy of the normal state be reproduced by Eq.(2.5) for a concentration $x = 1$ with the κ-dependent interaction parameters A and $m^*/m_\downarrow$ given in [88] [1]. The function $B(\kappa)$ for $0 \leq \kappa \leq 10$ is shown in Fig. 5.3.

In Fig. 5.4 we show the energy of the normal state for the values of the mass ratio $\kappa = 0.1$ (blue long dashed), representing the limit of a very light impurity, $\kappa = 1$ (black solid), and $\kappa = 10$ (red short dashed), i.e. a very heavy impurity. For heavy impurities ($\kappa = 10$) the main contribution to the energy in Eq.(5.1) comes from the binding energy A and the quasiparticle interaction B, since due to their big mass the kinetic energy of the $\downarrow$-particles tends to zero, so that the

[1] Note, that this procedure is different from the fitting procedure used in [60], where in that case the value $B = 0.14$ is almost half of what we find here. This leaves the value of the critical concentration almost unchanged.

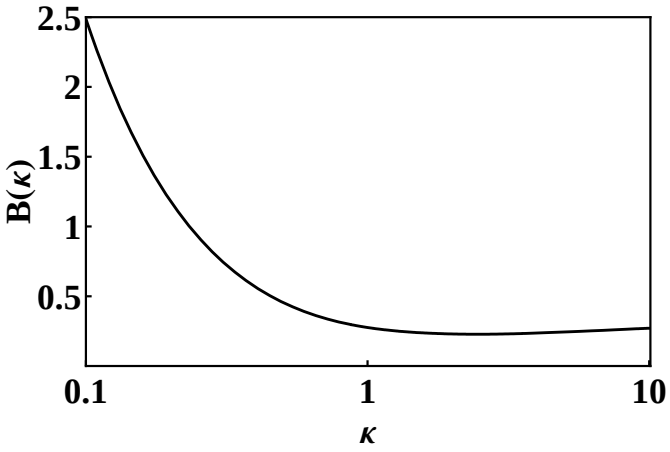

Figure 5.3: Parameter $B(\kappa)$ accounting for the quasiparticle interaction as a function of the mass ratio κ.

term proportional to $x^{5/3}$ can be neglected. For light impurities on the other hand ($\kappa = 0.1$), the main contribution comes from the binding A and the kinetic energy term, hence B is not very relevant.

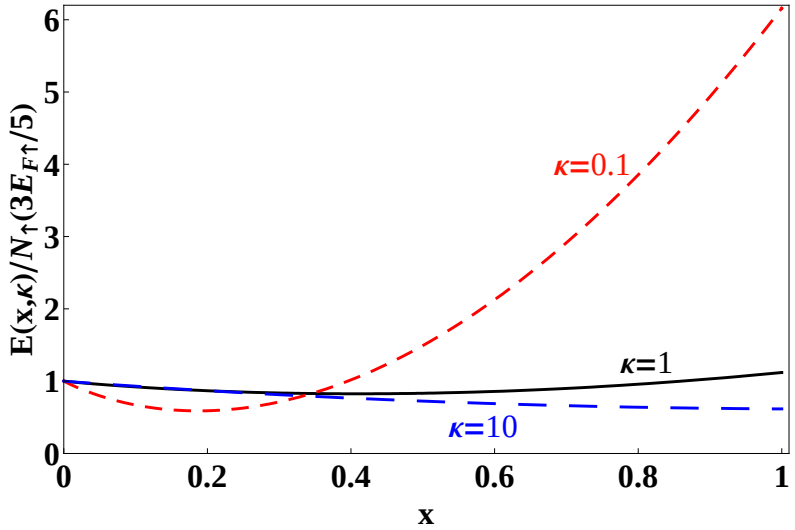

Figure 5.4: Equation of state of the normal phase as a function of the concentration x for the values $\kappa = 0.1$ (blue long dashed), $\kappa = 1$ (black solid) and $\kappa = 10$ (red short dashed) of the mass ratio.

The superfluid state in the unequal mass case yields

$$\frac{E_S(\kappa)}{N_S} = \xi_S(\kappa)\frac{3}{5}\frac{\hbar^2}{4m_\kappa}(6\pi^2 n_S)^{2/3} \equiv \epsilon_S(n_S, \kappa), \tag{5.3}$$

where N_S is the number of atoms in the superfluid phase, n_S the superfluid density, m_κ the reduced mass, and $\xi_S(\kappa)$ accounts for the interactions in the superfluid. Also in the superfluid phase the coefficient $\xi_S(\kappa)$ has only a very weak dependence on the mass ratio [115] so that we can set $\xi_S(\kappa) \equiv \xi_S = 0.42$ [82, 83] as in the equal mass case.

5.2 Chandrasekhar-Clogston limit $\mathbf{x}_c$

In order to establish the phase diagram for the system we address the equilibrium conditions for the phase separation of the superfluid and normal state in the bulk. We start by writing down the energy of the system at zero temperature

$$\begin{aligned} E &= 2\int d\mathbf{r}\ \Big[\,\epsilon_S(n_S,\kappa)n_S - \mu_S^0 n_S\,\Big] \\ &\quad + \int d\mathbf{r}\,\Big[\,\epsilon_N(x,\kappa)n_\uparrow - \mu_\uparrow^0 n_\uparrow - \mu_\downarrow^0 n_\downarrow\,\Big], \end{aligned} \tag{5.4}$$

where $\epsilon_S(n_S,\kappa)$ and $\epsilon_N(x,\kappa)$ are the energy densities per particle, $n_S, n_\uparrow$ and $n_\downarrow$ the densities, $\mu_\uparrow^0$ and $\mu_\downarrow^0$ the chemical potentials of the spin-$\uparrow$ and spin-$\downarrow$ component, respectively, and $\mu_S^0 = (\mu_\uparrow^0 + \mu_\downarrow^0)/2$ is the superfluid chemical potential.

To find the equilibrium conditions we minimize the energy with respect to the densities of the superfluid and normal phase, and we find the chemical potentials

$$\mu_S^0 = \xi_S \frac{\hbar^2}{4m_\kappa}(6\pi^2 n_S)^{2/3}, \tag{5.5}$$

$$\mu_\uparrow^0 = \left(g(x,\kappa) - \frac{3}{5}x g'(x,\kappa)\right)\frac{\hbar^2}{2m_\uparrow}(6\pi^2 n_\uparrow)^{2/3}, \tag{5.6}$$

$$\mu_\downarrow^0 = \frac{3}{5}g'(x,\kappa)\frac{\hbar^2}{2m_\uparrow}(6\pi^2 n_\uparrow)^{2/3}, \tag{5.7}$$

where prime means the derivative with respect to x. Eventually requiring that the pressure of the two phases be equal yields

$$\left(n_S^2\frac{\partial\epsilon_S}{\partial n_S}\right) = \frac{1}{2}\left(n_\uparrow^2\frac{\partial\epsilon_N(x,\kappa)}{\partial n_\uparrow} + n_\downarrow n_\uparrow\frac{\partial\epsilon_N(x,\kappa)}{\partial n_\downarrow}\right). \tag{5.8}$$

Making use of Eqs.(5.1) and (5.3) we can write the equal pressure condition as the density jump

$$\frac{n_\uparrow(x,\kappa)}{n_S(\kappa)} = \left(\frac{(1+\frac{1}{\kappa})\xi_S}{g(x,\kappa)}\right)^{3/5}. \tag{5.9}$$

From Eqs.(5.5)-(5.8) we obtain the implicit equation

$$g(x(\kappa)) + \frac{3}{5}[1-x(\kappa)]g'(x(\kappa)) - \left[\left(1+\frac{1}{\kappa}\right)\xi_{\rm S}\right]^{3/5}[g(x(\kappa))]^{2/5} = 0, \tag{5.10}$$

which gives the Chandrasekhar-Clogston limit $x_{\rm c}$ in dependence on the mass ratio κ. For values smaller than $x_{\rm c}(\kappa)$ the system remains normal, while for $x > x_{\rm c}(\kappa)$ the system starts nucleating the superfluid and phase separates into those two states.

In Fig. 5.5 we plot $x_c(\kappa)$ for mass ratios $0.1 < \kappa < 10$ (blue solid line). Comparing with $x_{\rm c}(\kappa = 1) = 0.42$ we find that for mass ratios $\kappa > 1$ the concentration needed to create a superfluid phase decreases, while for mass ratios $\kappa < 1$ it first increases and reaches a maximum value at $\kappa \sim 0.3$.

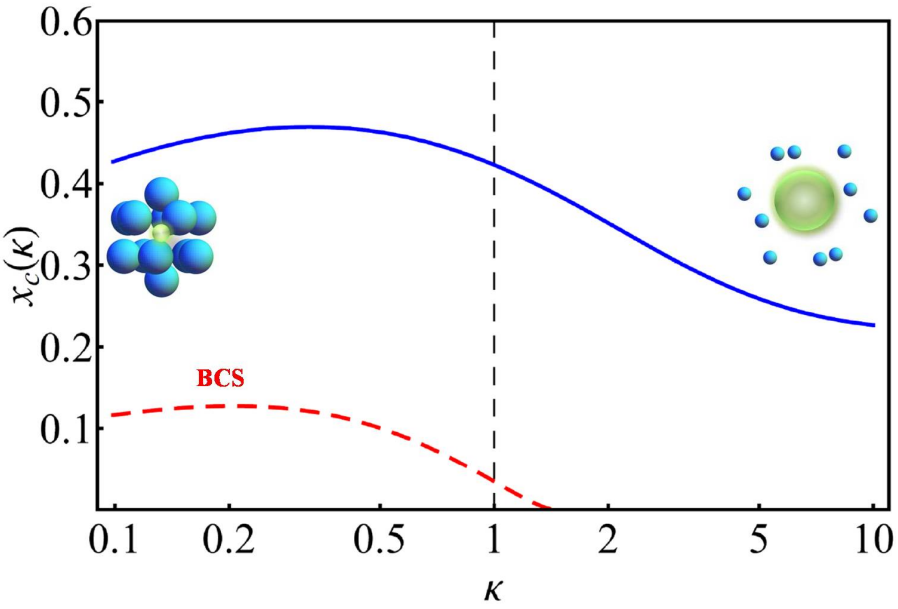

Figure 5.5: Critical concentration $x_c(\kappa)$ for the bulk system to phase separate as a function of the mass ratio κ (solid blue). In comparison, also the concentration derived from the BCS mean-field solutions at unitarity is shown (dashed red).

In the same figure we plot $x_{\rm c}(\kappa)$ as resulting from the BCS mean-field approach at unitarity (red dashed line, see also e.g. [72, 73]). In the latter treatment interactions in the normal phase are not taken into account, and hence its energy is just the sum of the $\uparrow$ and $\downarrow$ components, $E_{\rm N}^{\rm BCS} = E_{{\rm F}\uparrow}N_\uparrow + E_{{\rm F}\downarrow}N_\downarrow$, and the interaction parameter for the superfluid is $\xi_{\rm S}^{\rm BCS} = 0.59$. The significant quantitative difference between the two curves proves the importance of interactions [60].

It is worth noticing that x_c is sensitive to the actual value of the parameters used in Eq.(5.1). Since an exact calculation of the parameter $B(\kappa)$ in the case of unequal masses is still lacking, the interpolated value of $B(\kappa)$ might be a significant source of error. As for $\kappa >> 1$ the kinetic energy of the quasiparticles becomes irrelevant (see Eq.(5.1)), the Chandrasekhar-Clogston limit is only determined by the values of $A(\kappa)$ and $B(\kappa)$. Thus an uncertainty in B affects more our predictions.

We varied the value of $B(\kappa)$ by $\pm 10\%$ to see its final impact on the value of $x_c(\kappa)$, and we find that the variation in $x_c(\kappa)$ is about $\mp 5\%$ for mass ratios $\kappa \leq 1$, while for $\kappa > 1$ it is about $\mp 10\%$.

In terms of the chemical potentials of the $\uparrow$ and $\downarrow$ components the phase transition is characterized by the critical value $\eta_c(\kappa) = (\mu_\downarrow/\mu_\uparrow)_{x_c}$. From the knowledge of $\eta_c(\kappa)$ we are able to determine the coexistence lines between the superfluid and the normal phase.

5.3 Phase Diagram

We represent the different homogeneous phases employing the $\mu - h$ phase diagram, where $2\mu = \mu_\uparrow + \mu_\downarrow$ and $2h = \mu_\uparrow - \mu_\downarrow$. The transition line between the superfluid (S) and partially polarized (PP) phase is given by

$$\begin{aligned} \mu_{\rm S}^{h>0} &= \frac{1+\eta_c(\kappa)}{1-\eta_c(\kappa)} h, \\ \mu_{\rm S}^{h<0} &= -\frac{1+\eta_c(\frac{1}{\kappa})}{1-\eta_c(\frac{1}{\kappa})} h, \end{aligned} \tag{5.11}$$

and stands for the first-order phase transition between the unpolarized superfluid and the partially polarized normal phase.

The second-order phase transition between the partially polarized (PP) and the fully polarized (FP) phase occurs at $x = 0$, which corresponds to $\mu_\downarrow/\mu_\uparrow = -3/5A(\kappa)$, and thus the coexistence line is given by

$$\begin{aligned} \mu_{\rm PP}^{h>0} &= \frac{1-\frac{3}{5}A(\kappa)}{1+\frac{3}{5}A(\kappa)} h, \\ \mu_{\rm PP}^{h<0} &= -\frac{1-\frac{3}{5}A(\frac{1}{\kappa})}{1+\frac{3}{5}A(\frac{1}{\kappa})} h. \end{aligned} \tag{5.12}$$

Finally, the transition line between the fully polarized gas and the vacuum is given by the simple κ-independent relation

$$\mu_{\rm FP} = - \mid h \mid . \tag{5.13}$$

The phase diagram for unequal masses is not symmetric with respect to zero effective magnetic field h. In Fig. 5.6 (a) we show the symmetric phase diagram for $\kappa = 1$, while for $\kappa = 2.2$, corresponding to the case of a ^{87}Sr -^{40}K mixture [116], it is asymmetric with respect to zero magnetic field h as shown in Fig. 5.6 (b). While the superfluid region S moves clockwise (anticlockwise) for $\kappa > 1$ ($\kappa < 1$), the partially polarized PP moves in the opposite direction, see e.g. Figs. 5.6 and 5.6. In all the figures we use a solid line for the first-order phase transition, a dashed line for the second order phase transition, and a short-dashed-long-dashed line for the transition to the vacuum.

Such an asymmetry in phase diagrams is general for this system and has been already noticed by Parish *et al.* [75] in the T/μ vs h/μ phase diagram, and by Iskin and Sá de Melo [76, 77] in the $P = (N_\uparrow - N_\downarrow)/(N_\uparrow + N_\downarrow)$ vs $(1/k_{F,+}, a_F)$ diagram.

In particular, from Eq.(5.11) we can identify a critical mass ratio $\kappa^* = 2.73$ above which the superfluid region has moved entirely to the $h > 0$ plane (see e.g. Fig. 5.8(a)). This shift of the superfluid region above a certain mass ratio κ has also been identified by Parish *et* al. [75] applying BCS mean-field theory yielding $\kappa^* \sim 3.95$.

At the same time, for $\kappa > \kappa^*$ the sum of the spin-$\uparrow$ and spin-$\downarrow$ densities in the partially polarized phase is bigger than the superfluid density, $(n_\uparrow + n_\downarrow) > 2n_{\rm S}$. This anticipates the fact that in a trap the heavy partially polarized phase can sink towards the center, while the superfluid will form a spherical shell around it even if the two species feel the same trapping potential. This peculiar formation of a "sandwiched"superfluid has been previously identified also in [72–75].

5.4 Trapped Gas

Having constituents with different masses and hence different magnetic and optical properties permits to engineer different configurations in the trap by properly choosing the mass ratio, the polarization, and the trap parameters.

In order to study the trapped case we assume that the external potential is harmonic of the form $V_\sigma(\mathbf{r}) = \frac{1}{2}\alpha_\sigma r^2$ where $\alpha_\sigma = m_\sigma \omega_\sigma^2$ with $\sigma = \uparrow, \downarrow$, and that the local density approximation is applicable. Thus the configuration in the trap is found by using the expression $\mu_\sigma = \mu_\sigma^0 - \frac{1}{2}\alpha_\sigma r^2$ leading to

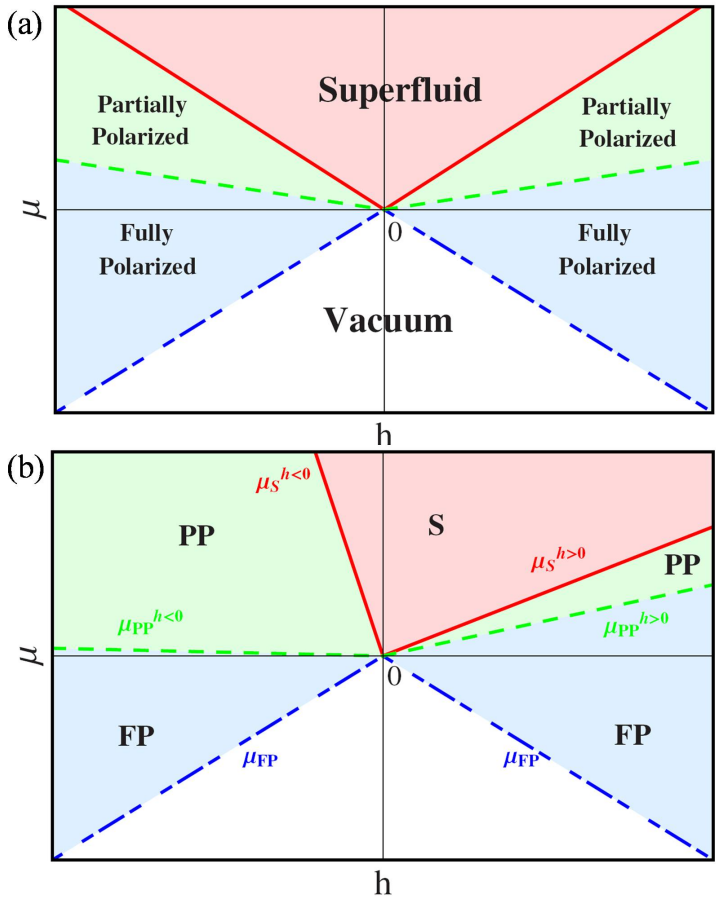

Figure 5.6: (a) In the case of equal masses the μ-h phase diagram is symmetric with respect to zero effective magnetic field h. Shown are the superfluid (S, red), the partially polarized (PP, green) and fully polarized (FP, blue) phases. (b) For $\kappa = 2.2$ the phase diagram is asymmetric.

$$\begin{aligned} \mu &= \mu_\uparrow^0 \left[\frac{1+\eta_0}{2} - \frac{1}{2}\left(1+\frac{\alpha_\downarrow}{\alpha_\uparrow}\right)\frac{r^2}{(R_\uparrow^0)^2} \right], \\ h &= \mu_\uparrow^0 \left[\frac{1-\eta_0}{2} - \frac{1}{2}\left(1-\frac{\alpha_\downarrow}{\alpha_\uparrow}\right)\frac{r^2}{(R_\uparrow^0)^2} \right], \end{aligned} \tag{5.14}$$

where we define $\eta_0 = \mu_\downarrow^0/\mu_\uparrow^0$ as the central imbalance of the system, and $(R_\uparrow^0)^2 = 2\mu_\uparrow^0/\alpha_\uparrow$. Note that if $\alpha_\uparrow = \alpha_\downarrow$ the effective magnetic field h does not depend on the position in the trap but is only a function of the central imbalance η_0. Concerning the central imbalance of the chemical potentials we have that if $\eta_0 < \eta_c(\kappa)$, there is no superfluid and the system consists only of the partially and fully polarized component. In the case that $\eta_0 > \eta_c(\kappa)$, we have a superfluid component whose fraction is determined by the value of η_0.

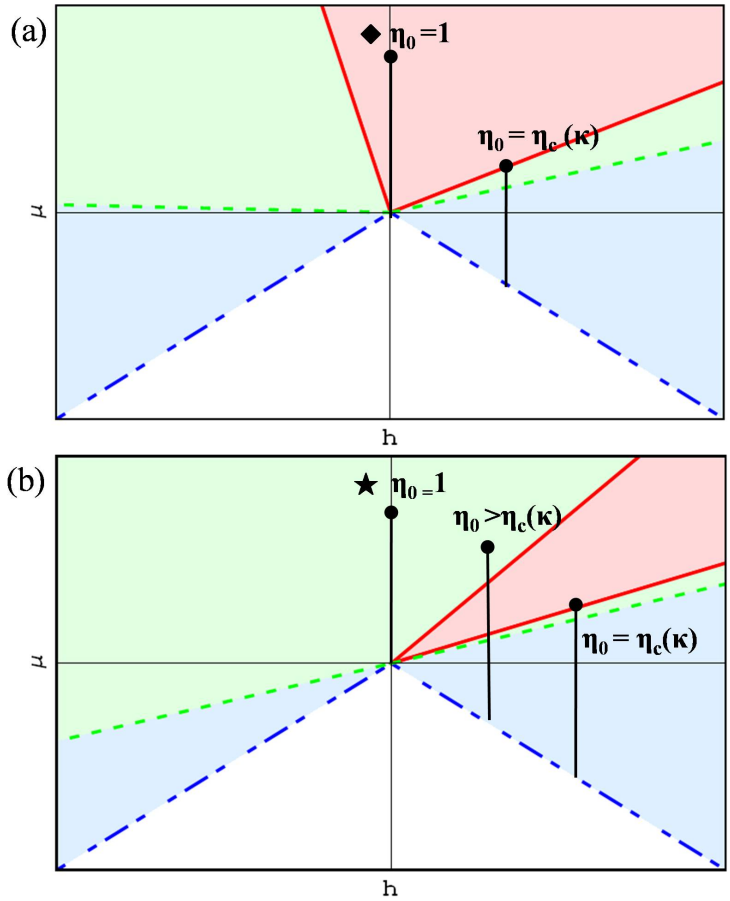

Figure 5.7: Examples of the succession of the LDA line for equal trapping $\alpha_\uparrow = \alpha_\downarrow$ and different values of the central imbalance η_0 (black dot) and mass ratios (a) $\kappa = 2.2$ (e.g.^{87}Sr-^{40}K) and (b) $\kappa = 6.7$ (e.g.^{40}K-^{6}Li).

In the following we will describe three different cases with different values of the polarization

$$P = \frac{N_\uparrow - N_\downarrow}{N_\uparrow + N_\downarrow}, \tag{5.15}$$

where the interplay between the asymmetry in the masses and in the trapping potential gives rise to different configurations.

Unequal Masses with Equal Trapping

We first analyze the situation when the spin-↑ and spin-↓ components have different masses $\kappa \neq 1$ but feel the same restoring forces $\alpha_\uparrow = \alpha_\downarrow$. This would be

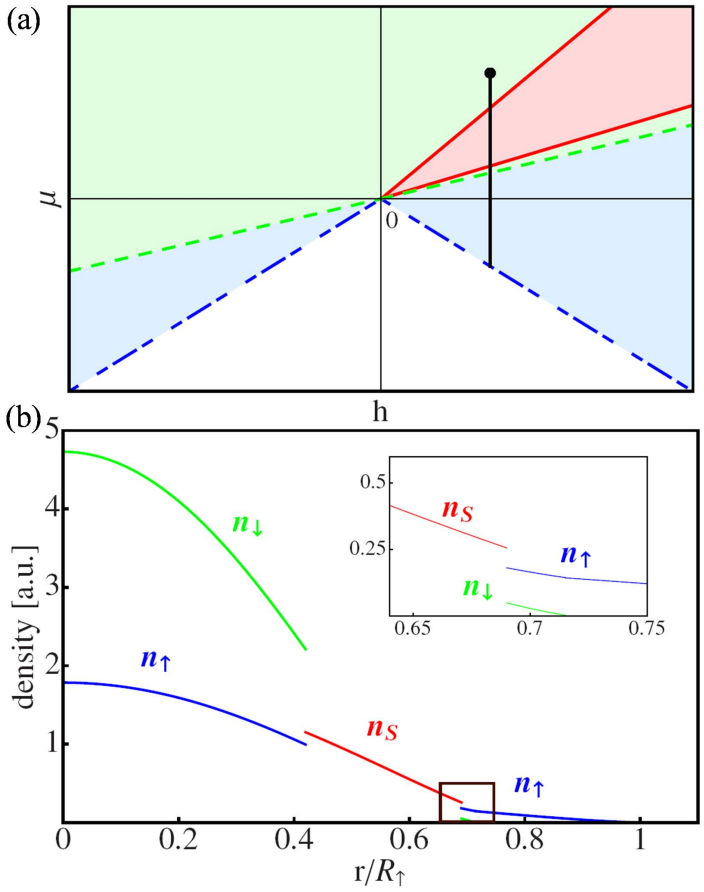

Figure 5.8: (a) Phase diagram for $\kappa = 6.7$, corresponding to a ^{40}K-^{6}Li mixture, and the LDA line (black vertical) for a central imbalance $\eta_0 = 0.3$ (black dot) and $\alpha_\uparrow = \alpha_\downarrow$. (b) Density profiles for $P = -0.13$; the inset shows a zoom into the outer superfluid-"light"normal border.

the case, for example, if the fermions are trapped magnetically and have identical magnetic moments.

For equal populations $\eta_c = 1$ and for mass ratios in the range $0.36 < \kappa < 2.73$ the system is completely superfluid (see Fig. 5.7 (a), LDA line marked with a diamond) and is always unpolarized, $P = 0$. In the opposite case, i.e. for $\kappa > 2.73$ ($\kappa < 0.37$), the system can never be completely superfluid even if the populations are equal. Therefore, we can also have the particular configuration of a system consisting only of a partially polarized phase without any fully polarized part as shown in Fig. 5.7 (b) by the LDA line marked with a star. In this particular case with $\eta_c = 1$, $\alpha_\uparrow = \alpha_\downarrow$ and $\kappa = 6.7$, the polarization of the trapped system is $P = -0.57$.

If $\eta_0 > 1/\eta_c(1/\kappa)$ the trapped system will consist of a three-shell configuration, where the superfluid is sandwiched between a "heavy"normal phase (heavy spin-

↓ are the majority) at the center of the trap, and a "light"normal phase (light spin-↑ are the majority) in the outer trap region.

As an example we choose the mass ratio $\kappa = 6.7$ corresponding to a ^{40}K -^{6}Li mixture [67, 116]. The phase diagram of the system is shown in Fig. 5.8 (a) together with the LDA line for a central imbalance $\eta_0 = 0.3$ (black dot). The intersection of the LDA line with the coexistence lines determines the radii of the configuration, from which we are able to calculate the density profiles. These are shown in Fig. 5.8 (b) for a polarization $P = -0.13$.

The density jump (or drop) between the superfluid and both normal phases is a function of κ according to Eq.(5.9). For $\kappa = 6.7$ at the "heavy"normal - superfluid border, $n_\downarrow \sim 1.92 n_{\rm S}$ and $n_\uparrow = x_{\rm c}(\frac{1}{\kappa})n_\downarrow \sim 0.86 n_{\rm S}$, while at the superfluid-"light"normal border $n_\uparrow \sim 0.71 n_{\rm S}$ and $n_\downarrow = x_{\rm c}(\kappa)n_\uparrow \sim 0.17 n_{\rm S}$ (see inset Fig. 5.8 (b)). Note that this is quite different compared to the equal mass case, where the jump between the superfluid and the majority component is $n_\uparrow \sim 1.01 n_{\rm S}$ and hence the spin-↑ density is practically continuous.

Unequal Masses with Trapping Anisotropy

Using unequal restoring forces for the trapped atoms the mass ratio for having a sandwiched superfluid needs not to be necessarily bigger than the critical value κ^*. In order to have a three-shell configuration the condition is

$$\mu < \mu_{\rm S}^{h<0} \Rightarrow \frac{\alpha_\downarrow}{\alpha_\uparrow} = \kappa \frac{\omega_\downarrow^2}{\omega_\uparrow^2} > \frac{1}{\eta_{\rm c}(\frac{1}{\kappa})}. \tag{5.16}$$

For example, for equal trapping frequencies, Eq.(5.16) simplifies to $\kappa > [1/\eta_{\rm c}(1/\kappa)]$ resulting in the critical mass ratio $\kappa_{\rm c} \sim 1.95$, while for equal oscillator lengths one gets $\kappa_{\rm c} \sim 6.7$. In Fig. 5.9 (a) we show the $\mu - h$ phase diagram of such a particular configuration, where we choose $\kappa = 2.2$ corresponding to a ^{87}Sr -^{40}K mixture [116]. The LDA line is drawn for the values $\eta_0 = 2.1$ (black dot) and $\alpha_\downarrow/\alpha_\uparrow = 8$.

In the density profiles as shown in Fig. 5.9 (b) we have chosen the parameters such that the resulting global polarization is $P = 0$.

5.5 No Trapping for ↑ Component

An interesting limiting case is when one of the elastic constants α_σ is zero (or very small), implying that one of the components would not be confined in absence of

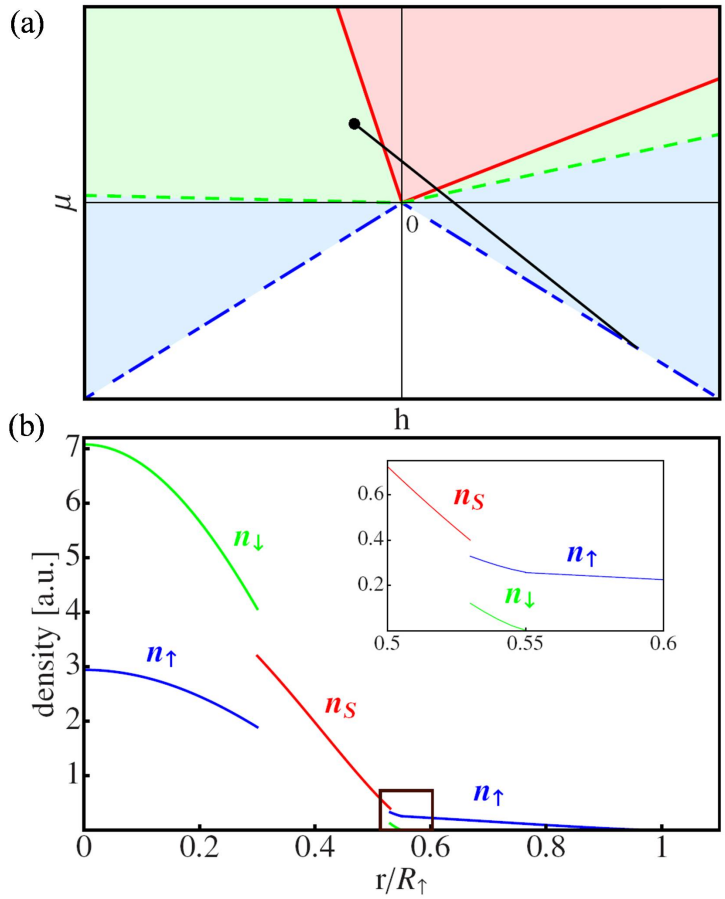

Figure 5.9: (a) Phase diagram for $\kappa = 2.2$ and LDA line for $\eta_0 = 2.1$ (black dot) and $\alpha_\downarrow/\alpha_\uparrow = 8$. With this choice, it crosses the "heavy normal", superfluid, "light normal"and fully polarized phases. (b) Density profiles for a global polarization $P = 0$; the inset shows a zoom into the superfluid-"light"normal border.

interspecies atomic forces.

If we assume that $\alpha_\uparrow \to 0$, the LDA line in the μ-h phase diagram is parallel to the polarized-vacuum transition line as shown in Fig. 5.10 (a).

Let us start considering the equal mass, $m_\uparrow = m_\downarrow = m$, highly unbalanced $N_\downarrow \gg N_\uparrow$ case. The densities are easily found to be [60]

$$\begin{aligned} \mu_\downarrow^0 &= \frac{\hbar^2}{2m}\left[6\pi^2 n_\downarrow(\mathbf{r})\right]^{2/3} + V_\downarrow(\mathbf{r}), \\ \mu_\uparrow^{0\prime} &= \frac{\hbar^2}{2m^*}\left[6\pi^2 n_\uparrow(\mathbf{r})\right]^{2/3} + V_\uparrow'(\mathbf{r}), \end{aligned} \tag{5.17}$$

where $\mu_\uparrow^{0\prime} = \mu_\uparrow^0 + \frac{3}{5}A\mu_\downarrow^0$, $V_\uparrow'(\mathbf{r}) = V_\uparrow(\mathbf{r}) + \frac{3}{5}AV_\downarrow(\mathbf{r})$ and $A \equiv A(\kappa = 1)$. From these

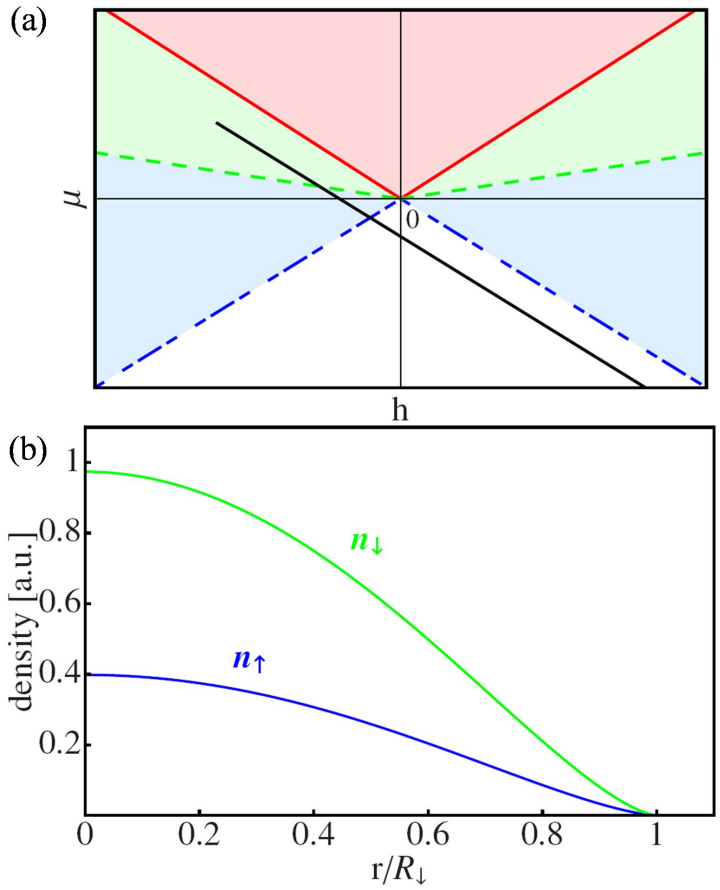

Figure 5.10: (a) Phase diagram for $\kappa = 1$. The LDA line represents the case $\alpha_\uparrow = 0$. (b) Density profile in the limiting case $\alpha_\uparrow = 0$ and $P = -0.42$.

equations it is clear that if $V_\uparrow \to 0$, the $\uparrow$-atoms feel nevertheless the renormalized potential $\frac{3}{5}AV_\downarrow(\mathbf{r})$ and are confined due to the interaction with the $\downarrow$-component. In this regime $\mu_\uparrow^0$ is negative and in the limit of a single $\uparrow$-atom, i.e. $\mu_\uparrow^{0'} \to 0$, it takes the value $\mu_\uparrow^0 = -3/5A\mu_\downarrow^0$, corresponding to a polarization $P = -1$. This induced trapping mechanism would not be predicted by a BCS mean-field description, where interactions are absent in the normal phase, and the $\uparrow$-atoms cannot be confined by the $\downarrow$-atoms.

Increasing the number of $\uparrow$ particles, the LDA line moves upward until it crosses the origin of the phase diagram, corresponding to $\mu_\uparrow^0 = 0$, and the system remains normal since for equal masses the slope of the superfluid-partially polarized coexistence line is bigger than the slope of the LDA line, i.e. $\eta_c(1/\kappa = 1) > 0$ (see Eq.(5.11)). Moreover, in this case the $\downarrow$-fully polarized phase is absent as the radii of the $\downarrow$ and $\uparrow$ species coincide, and in this limit the polarization approaches the value $P = -0.42$.

If we further increase $N_\uparrow$ we enter in a three-shell configuration including an intermediate superfluid component. But since in this case the atoms of species $\uparrow$ are no longer confined, they escape from the trap, and the system goes back to the normal state previously described. Hence we can never find a stable configuration containing a superfluid region, and the polarization of the system will always be in the range $-1 < P \leq -0.42$.

Note that the same scenario is valid for $m_\downarrow > 0.9m_\uparrow$, where $\eta_c(1/\kappa)$ is positive and the range of the polarization is between $P = -1$ and an upper value which is dependent on κ.

Interestingly, in the case $m_\downarrow < 0.9m_\uparrow$, for which $\eta_c(1/\kappa) < 0$, we find that adding $\uparrow$-atoms we end up in a superfluid state [117] characterized by a density profile given by

$$\mu_{\rm S}^0 = \xi_{\rm S}\frac{\hbar}{2m}\left[6\pi^2 n_{\rm S}(\mathbf{r})\right]^{2/3} + \widetilde{V}(\mathbf{r}), \tag{5.18}$$

where $\widetilde{V}(\mathbf{r}) = \frac{1}{4}m\omega_\downarrow^2 r^2$ is the effective potential felt by the superfluid. This configuration would correspond to a LDA line which stays entirely in the superfluid region, crossing the origin of the phase diagram. The value of the polarization for $m_\downarrow < 0.9m_\uparrow$ covers the entire range $-1 < P \leq 0$.

From the experimental point of view the above configurations could be in principle reached starting with both the trapping frequencies different from zero and a certain initial polarization, and then opening adiabatically the trap for the $\uparrow$-atoms. For instance, starting with only a superfluid in the trap the final state of the system will be simply a superfluid with a bigger radius for $m_\downarrow < 0.9m_\uparrow$, while it will be a normal state in which both components have the same radius (see Fig. 5.10 (b)) if $m_\downarrow > 0.9m_\uparrow$.

5.6 Conclusions

We have studied the zero temperature μ-h phase diagram of the unitary Fermi gas in the case of unequal masses, assuming phase separation between an unpolarized superfluid and a polarized normal phase. The latter is described by an equation of state which, unlike in the BCS mean-field treatment, takes into account the effect of the strong interaction. As we have shown, this has a dramatic impact on the results such as the Chandrasekhar-Clogston limit needed to start nucleating a superfluid.

Using LDA we have determined how the trapped configuration depends on the trapping potential, the mass ratio, and the polarization. Many different configurations are possible. Among them it is worth mentioning the three-shell con-

figuration [72–75], where the superfluid is sandwiched between a "heavy"normal phase at the center and a "light"normal phase towards the edges of the trap. Note that the shells can occupy quite small regions, and we cannot exclude that surface tension plays an important role in this case. For the sandwiched configuration, it would be interesting to investigate its behaviour when the system is rotated. As to fast rotation the question is how vortex structures can enter the superfluid, since it is surrounded by normal parts. An adiabatic rotation might cause a depletion of the sandwiched condensate in the plane of rotation, increasing the normal phase towards the edges of the trap, and restricting the superfluid to the poles of the rotating system.

We can also have non-trivial configurations even if one of the two components is not trapped, but still remains confined due to the interaction induced trapping, which is not present in the BCS treatment. Such configurations can be experimentally obtained by adiabatically opening the trap for one of the two species.

An important issue is the existence of other phases at unitarity. In the present work we assume that only two phases are possible, and hence we have not considered any polarized superfluid state. For the equal mass case the assumption seems to be correct and is theoretically understood by comparing the phase separated state energy with the polarized superfluid energy calculated via Monte Carlo, as in e.g. [118]. The same information is not yet available for the unequal mass case. However, taking the quasi-particle point of view in [118] and the recent calculation for equal population by Baranov *et* al. [119], it seems that when the mass of the minority component is much bigger than the one of the majority component, the polarized superfluid phase should be included in the description, as predicted by mean-field theory. Theoretical work in this direction is in progress.

5.7 Monte Carlo Calculation of Gezerlis *et al.*

Recently, Gezerlis *et al.* [78] employed quantum Monte Carlo simulations to investigate fermion pairing in the unitary regime for a mass ratio $\kappa \sim 6.5$, corresponding to a ^{6}Li-^{40}K mixture. The authors calculate the quasiparticle excitation energies, the equation of state, the Chandrasekhar-Clogston limit and the density profiles of heavy-in-light (light-in-heavy) Fermion mixtures in presence of harmonic trapping.

At this point we focus on a comparison between the values of the Chandrasekhar-Clogston limit and the density profiles of the trapped gas. For a mass ratio $\kappa = 6.5$ (majority light) the critical concentration is found to be $x_c^{\mathrm{QMC}} = 0.02(2)$, which is smaller than our result $x_c = 0.24$ based on diagrammatic results for $A(\kappa)$, $m^*(\kappa)$ [88], and the interpolated $B(\kappa)$.

For a mass ratio $\kappa = 0.15$ (majority heavy) on the other hand, the authors find the value $x_c^{\mathrm{QMC}} = 0.49(5)$, which is in good agreement with the value $x_c = 0.45$ we find (see also Fig. 5.5).

This differences can be explained by the fact, that the value of x_c is sensitive to the form of the equation of state and to the values of the parameters A, m^*, and B employed.

We find that the density profiles of the harmonically trapped configurations are in a good agreement with our results. In Fig. 5.11 (a) we show the polarization of a trapped system with $\kappa = 6.5$ and $\alpha_\downarrow/\alpha_\uparrow = 2$ as presented by Gezerlis *et al.* in [78] for different values of the polarization $P^{GEZ} = (N_h - N_l)/(N_h + N_l)$, where N_h is the number of the heavy particles and N_l the number of the light particles, respectively. Note, that since we define the polarization as $P = (N_\uparrow - N_\downarrow)/(N_\uparrow + N_\downarrow)$, this leads to $P^{GEZ} = -P$.

In Fig. 5.11 (b)-(d), we show the density profiles as resulting from our treatment. We find good agreement in the prediction for the shell structure in the trap (two- and three shell, respectively) as well as for the radii of the single components for different values of the polarization P. While for $P = 0$ and $P = -0.4$ the trapped system exhibits the three-shell structure with a sandwiched superfluid, for $P = 0.4$ we recover as [78] the two-shell structure of a centered superfluid core and a surrounding normal shell.

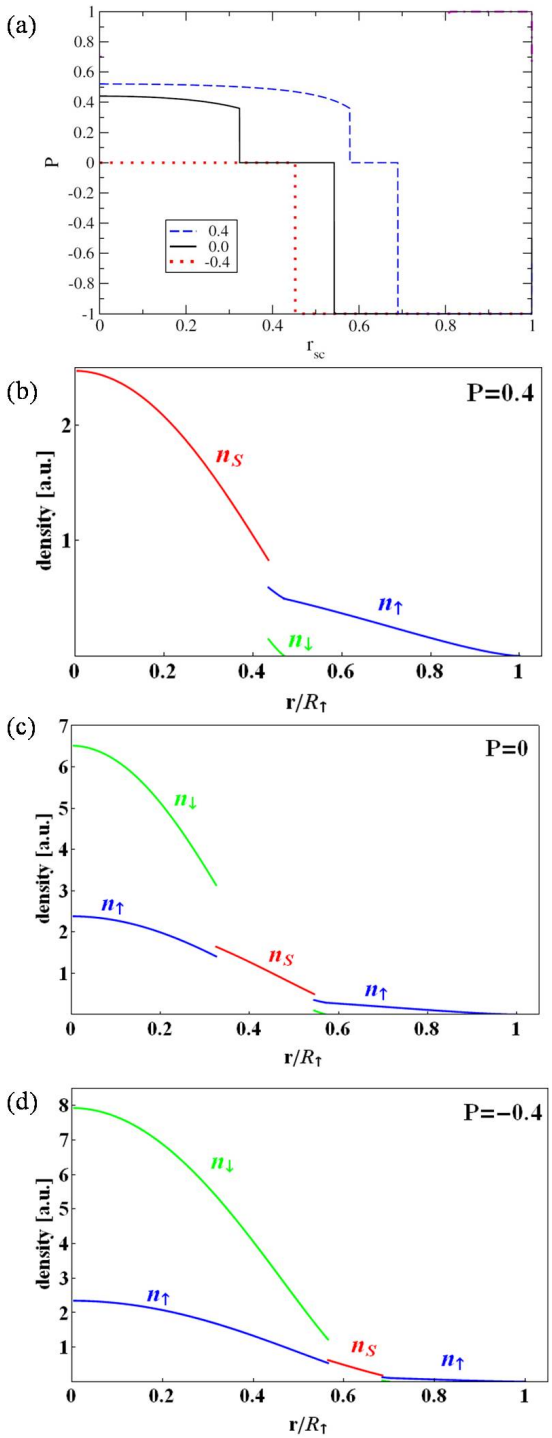

Figure 5.11: (a) Polarization $P^{GEZ} = (N_h - N_l)/(N_h + N_l)$ of a trapped system as a function of the radius (scaled such that at r_{sc} the density goes to zero) for $P - 0.4$ (pink dotted), $P = 0$ (black solid), and $P = 0.4$ (blue dashed), from [78]. (b)-(d) Density profiles of the trapped configuration for different values of the polarization $P = (N_\uparrow - N_\downarrow)/(N_\uparrow + N_\downarrow)$. (b) $P = -0.4$, (c) $P = 0$, and (d) $P = 0.4$.

6 Dipole Polarizability of the Unitary Fermi Gas

The standard way to polarize a Fermi superfluid is to create an imbalance of the spin populations. This can be achieved experimentally by either transferring atoms of the same species in different hyperfine levels or in systems with different atomic species as discussed in the previous chapter. In that case the atomic cloud in the trap forms a shell structure consisting of a superfluid core and a surrounding normal phase as it has been observed in different experiments [47, 63, 87].

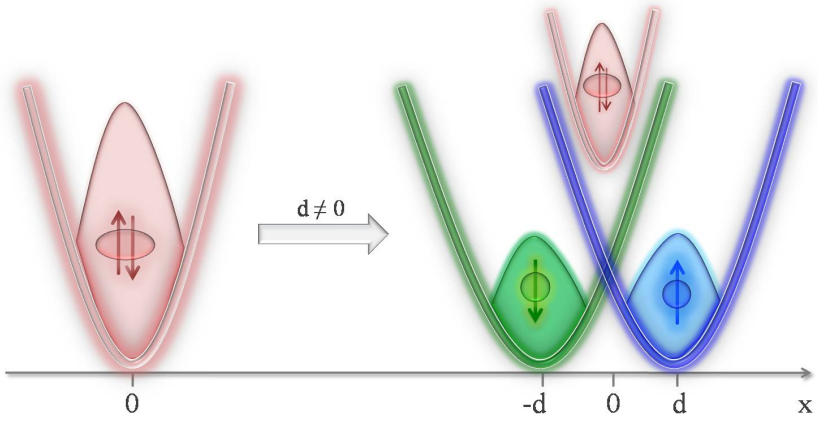

Figure 6.1: Sketch: Initially, the system is completely superfluid (P=0), $d = 0$ and hence $V_\uparrow = V_\downarrow$. As soon as the potentials are displaced in opposite directions, $d \neq 0$, the pairs in the superfluid are broken and two bordering, fully polarized $\uparrow$- and $\downarrow$ clouds are created.

A different way to polarize the system is given by geometric means. Since in principle the trapping potentials can be engineered at will, one can tune them such that the spin-$\uparrow$ and spin-$\downarrow$ components are displaced as shown in Fig. 6.1. This creates an imbalance not in the number of particles, but in its conjugate variable, the chemical potential. It is then possible to study the static response of the system to the displacement of the traps which gives rise to a dipole polarization per particle

$$D(d) = \frac{1}{N} \int d\mathbf{r} \;\; x(n_\uparrow - n_\downarrow), \tag{6.1}$$

where N is the total number of particles in the system, $2d$ is the relative displacement of the two trapping potentials, $n_{\uparrow,\downarrow}$ the spin-$\uparrow$ and spin-$\downarrow$ densities, respectively.

The dipole polarizability of a superfluid Fermi gas has already been presented by Recati *et al.* in [120]. In this paper the authors adapt the two-fluid picture, i.e., the phase separation between a superfluid and a fully polarized phase. As sketched in Fig. 6.1, starting from an initially superfluid system, the traps for the $\uparrow$- and $\downarrow$ components are displaced in opposite directions. This displacement causes the pairs in the superfluid to break, thus creating two fully polarized clouds, in which the particle number steadily increases with d, while at the same time the superfluid diminishes. Note, that in this case the superfluid is always symmetric around $x = 0$. The authors find that differently from the noninteracting case, where the dipole polarization is constant $D = d$, the dipole polarization changes significantly as shown in Fig. 6.2 due to the interactions in the superfluid state.

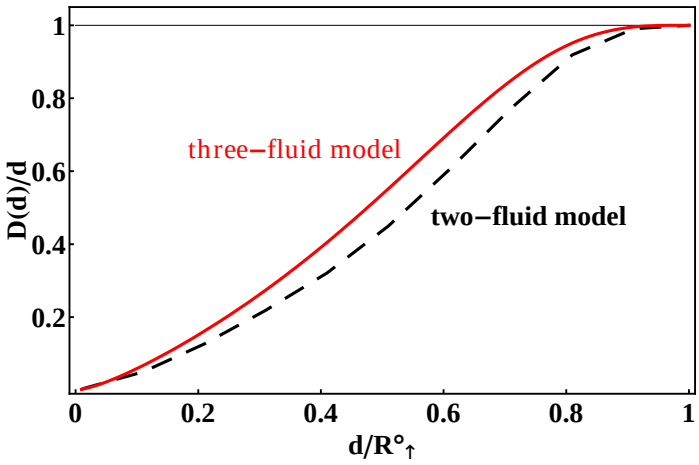

Figure 6.2: Normalized induced dipole polarizability $D(d)/d$ in the two-fluid (red line) and three-fluid (black dashed) model (see text below) vs displacement d of the trapping potentials together with the dipole polarizability for a noninteracting system (black line). The displacement d is given in units of the Thomas-Fermi radius $R^0_\uparrow$.

We want to extend the problem to a system with a finite polarization $P = (N_\uparrow - N_\downarrow)/(N_\uparrow + N_\downarrow)$. Moreover, we want to consider both the two-fluid picture, i.e. the phase separation between a superfluid and a fully polarized phase, as well as the three-fluid picture, where the system phase separates into a superfluid and a partially polarized gas. We furthermore assume as in [120] that the traps are displaced adiabatically and the system stays at equilibrium in the new potential.

6.1 Dipole Polarizability in the Two-Fluid Model

Phase Diagram

The two-fluid model is the simplest assumption for the phase separation at resonance and has been first discussed by Chevy [56] to explain the experimental density profiles of the resonant Fermi gas as observed by the Rice group [47, 49].

For a finite polarization, $N_\uparrow \neq N_\downarrow$, and no displacement $d = 0$, the initial configuration consists of a superfluid core and a fully polarized $\uparrow$ shell. The equation of state of the superfluid is given by

$$\mu_\mathrm{S} = \frac{\hbar^2}{2m}\xi_\mathrm{S}(6\pi^2 n_\mathrm{S})^{2/3}, \tag{6.2}$$

where the parameter ξ_S=0.42 [65] accounts for the interactions, m is the atomic mass, and n_S is the superfluid density. The equation of state for the fully polarized gas on the other hand is simply given by

$$\mu_\sigma = \frac{\hbar^2}{2m}(6\pi^2 n_\sigma)^{2/3}, \tag{6.3}$$

where $\sigma = \uparrow, \downarrow$ and n_σ is the density of the respective species. From the chemical potentials and the relation $\mu_\mathrm{S} = \frac{1}{2}(\mu_\uparrow + \mu_\downarrow)$ we can calculate the pressure of the superfluid phase via the Gibbs-Duhem identity $dP_\mathrm{S} = n_\uparrow d\mu_\uparrow + n_\downarrow d\mu_\downarrow$

$$P_\mathrm{S} = \frac{1}{15\pi^2}\left(\frac{m}{\xi_\mathrm{S}\hbar^2}\right)(\mu_\mathrm{S})^{5/2}, \tag{6.4}$$

while the pressure of the, say, $\uparrow$ component is given by

$$P_\uparrow = \frac{1}{15\pi^2}\left(\frac{m}{\hbar^2}\right)(\mu_\uparrow)^{5/2}. \tag{6.5}$$

The thermodynamic condition for the coexistence of two phases is that their pressure and the chemical potential be be the same, which for the superfluid and the $\uparrow$-gas yields

$$P_\mathrm{S} = P_\uparrow \Rightarrow \frac{\mu_\downarrow}{\mu_\uparrow} = (2\xi_\mathrm{S})^{3/5} - 1 \equiv \eta_\mathrm{c} \sim -0.099. \tag{6.6}$$

The different homogeneous phases can be represented employing the $\mu - h$ phase diagram, where $2\mu = \mu_\uparrow + \mu_\downarrow$ and $2h = \mu_\uparrow - \mu_\downarrow$. In this phase diagram, the transition line between the superfluid (S) and the fully polarized (FP) phase is given by

$$\mu_\mathrm{S}^{h>0} = \frac{1+\eta_\mathrm{c}}{1-\eta_\mathrm{c}}h \equiv \frac{(2\xi_\mathrm{S})^{3/5}}{2-(2\xi_\mathrm{S})^{3/5}}h, \tag{6.7}$$

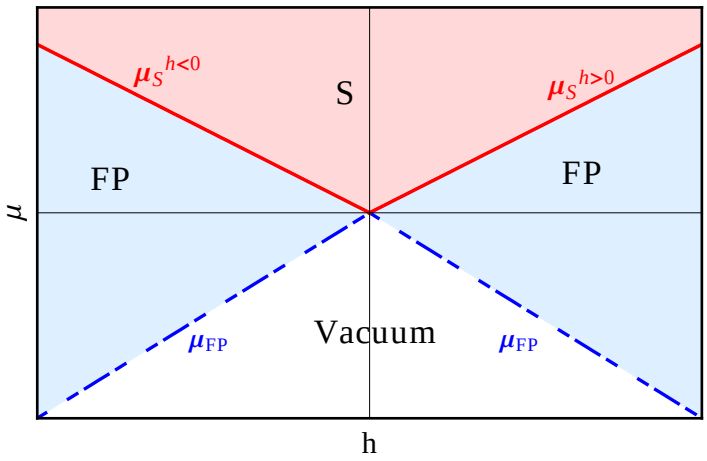

Figure 6.3: $\mu - h$ phase diagram of the system in the two-fluid model. Shown are the superfluid region (S, red), and the fully polarized (FP, blue) phase.

$$\mu_S^{h<0} = -\frac{1+\eta_c}{1-\eta_c}h \equiv -\frac{(2\xi_S)^{3/5}}{2-(2\xi_S)^{3/5}}h, \tag{6.8}$$

while the transition line between the fully polarized and the vacuum is given by the simple relation

$$\mu_{FP} = -|h| \tag{6.9}$$

as shown in Fig. 6.3.

The trapping induces position-dependent chemical potentials for the two atomic species. Using the local density expression for the chemical potentials

$$\mu_{\uparrow\downarrow}(\mathbf{r}) = \mu^0_{\uparrow\downarrow} - V_{\uparrow\downarrow}(\mathbf{r}), \tag{6.10}$$

where

$$V_{\uparrow\downarrow}(\mathbf{r}) = \frac{1}{2}m\left[\omega_\perp^2 r_\perp^2 + \omega_x^2(x \mp d)^2\right], \tag{6.11}$$

with $r_\perp = \sqrt{y^2+z^2}$, one can explore the phase diagram for different values of the central imbalance η_0 and displacement d. Combining Eqs.(6.10) and (6.11) together with the relations for μ and h, we find

$$\begin{aligned} \mu &= \mu^0_\uparrow\left[\frac{1+\eta_0}{2} - \frac{(x^2+d^2+r_\perp^2)}{(R^0_\uparrow)^2}\right], \\ h &= \mu^0_\uparrow\left[\frac{1-\eta_0}{2} + \frac{2xd}{(R^0_\uparrow)^2}\right], \end{aligned} \tag{6.12}$$

where $\eta_0 = \mu_\uparrow^0/\mu_\downarrow^0$ is the central imbalance of the system, $(R_\uparrow^0)^2 = (2\mu_\uparrow^0/m\omega^2)$ and we have set $\omega_x = \omega_\perp \equiv \omega$. If the central imbalance $\mu_\downarrow^0/\mu_\uparrow^0 \equiv \eta_0 < \eta_c$, the system is fully polarized, while for $\eta_0 > \eta_c$ the system phase separates into a superfluid and a polarized phase, where the fraction of the superfluid is determined by the value of η_0. Eventually, for $\mu_\uparrow^0 = \mu_\downarrow^0$ and hence $\eta_0 = 1$, the system is fully superfluid as in [120].

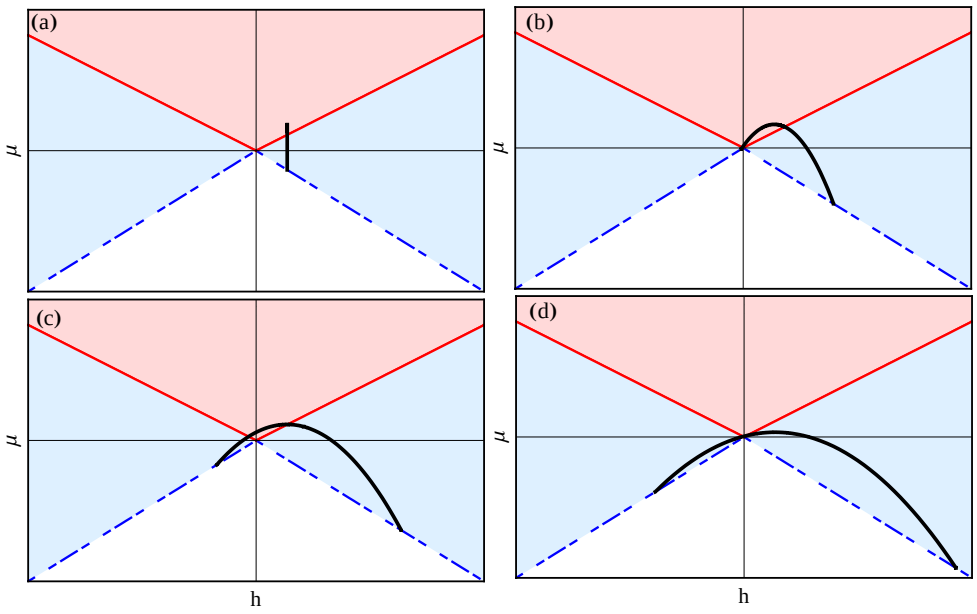

Figure 6.4: μ-h phase diagram of the system in the two-fluid model,where the LDA line (black) is shown for different values of the displacement (a) $d = 0$, (b) $d = d_{\mathrm{crit}}$, (c) $d > d_{\mathrm{crit}}$, and (d) $d = d_{\mathrm{sep}}$ and an arbitrary value of the central imbalance $\eta_0 < \eta_c$.

To explore the $\mu - h$ phase diagram, we set $r_\perp = 0$ in Eq.(6.12), fix the value of the imbalance η_0 and vary x and d as shown in Fig. 6.4. For $d = 0$ and $\eta_0 > \eta_c$, the system consists of a superfluid core and a fully polarized external shell (Fig. 6.4 (a)). Changing the values of d and x, we then explore the phase diagram along a parabolic trajectory as shown in Fig. 6.4 (b)-(d). Importantly, for $d = 0$ the two external potentials are the same and the effective magnetic field h is constant and depends only on the central imbalance η_0.

Complementary to this is Fig. 6.5, which shows a sketch of the 2D cut of the system in the $x - y$ plane. For $d = 0$, we have the initial symmetric configuration of a superfluid centered inside a fully polarized gas (Figs. 6.4 (a) and 6.5 (a)). By changing the value of d, the superfluid moves to the left side according to the effective potential $V^{\mathrm{S}}(\mathbf{r}) = \frac{1}{2}[V_\uparrow(\mathbf{r}) + V_\downarrow(\mathbf{r})]$ it feels, while the fully polarized $\uparrow$-gas moves to the right according to $V_\uparrow(\mathbf{r})$. For a critical value $d = d_{\mathrm{crit}}$ (Figs. 6.4 (b) and 6.5 (b)), the superfluid and the fully polarized border coincide. Only for $d > d_{\mathrm{crit}}$ (Figs. 6.4 (c) and 6.5 (c)), we eventually start to break the pairs in the

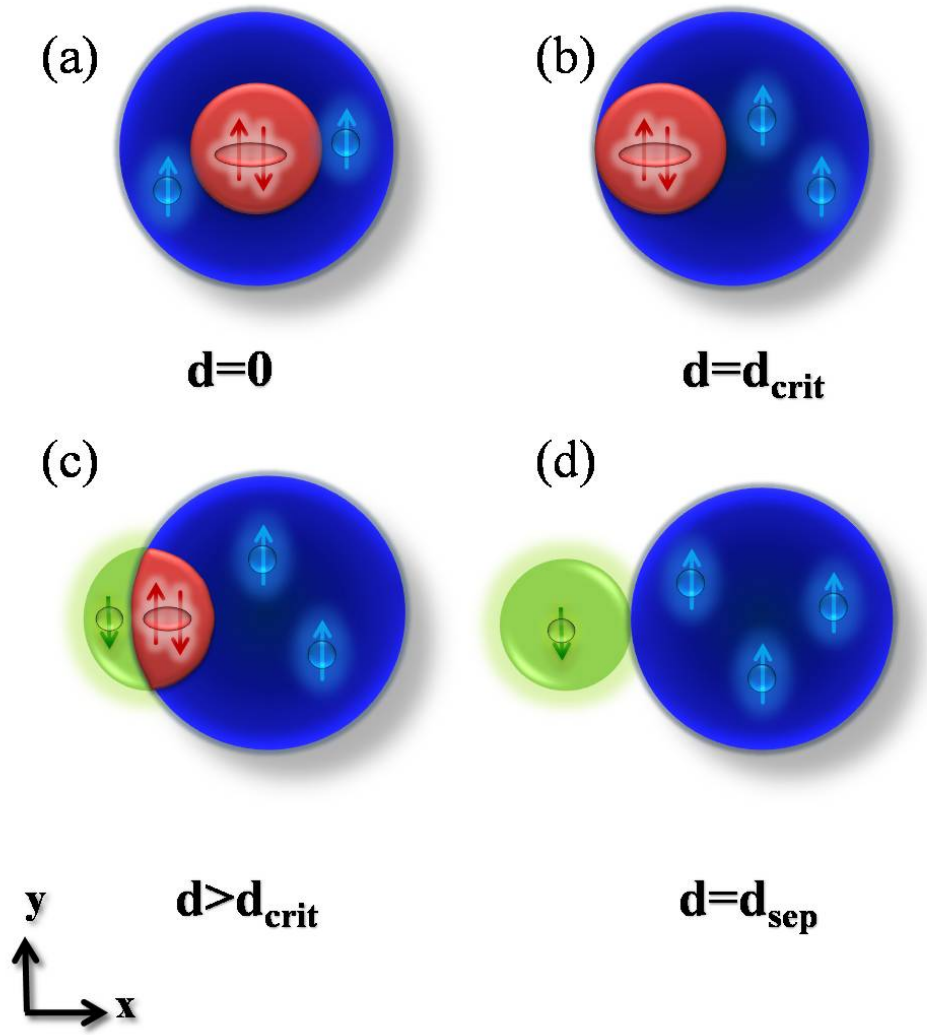

Figure 6.5: Sketch of the four different states of the dipole polarization process in the two-fluid model in a 2D cut: For $d = 0$, the initial configuration is a centered superfluid (red) surrounded by a fully polarized spin-↑ (blue) shell. For $d \neq 0 < d_{\mathrm{crit}}$, the superfluid moves in opposite direction with respect to the ↑-cloud. For $d > d_{\mathrm{crit}}$, a polarized ↓-cloud (green) is created by breaking the pairs in the superfluid which consequently diminishes, until for $d = d_{\mathrm{sep}}$ we have two separate fully polarized spin-↑ and spin-↓ clouds.

superfluid and create a fully ↓-polarized fraction on the left side of the superfluid. This process continues until we eventually reach the value $d = d_{\mathrm{sep}}$, where the superfluid has completely vanished, and we are left with two entirely separated, fully ↑- and ↓ polarized clouds (Figs. 6.4 (d) and 6.5 (d)). The value d_{crit} and d_{sep} are not universal, but depend on the central imbalance η_0 of the system as

$$\begin{aligned} \frac{d_{\mathrm{crit}}}{R_\uparrow^0} &= \frac{\left(1-\sqrt{\eta_0}\right)}{2}, \\ \frac{d_{\mathrm{sep}}}{R_\uparrow^0} &= \frac{\left(1+\sqrt{\eta_0}\right)}{2}. \end{aligned} \tag{6.13}$$

To derive the expression for the critical distance d_{crit}, the condition is $\mu = 0$ and $h = 0$ (see Fig. 6.4 (b)). This means that in the $\mu - h$ phase diagram the LDA line is just about to enter into the fully polarized phase for $h < 0$. The condition for d_{sep} on the other hand is given by the distance needed to create two separate fully polarized clouds, whose midpoints are $d = \frac{1}{2}(R_\uparrow^0 + R_\downarrow^0)$ away from each other. It is important to note, that in the case of a finite particle imbalance P, the superfluid is not symmetric around $x = 0$, and the fully polarized clouds, albeit their minima at $x \pm d$, have different sizes according to the initial central imbalance.

6.2 Results

In order to calculate the dipole polarization $D(d)$ and the dipole polarizability $D(d)/d$, we need the expressions for densities of the superfluid, the spin-↑ and spin-↓ components, as well as the borders separating the superfluid from the fully polarized components. The superfluid feels the effective potential $V^{\mathrm{S}}(\mathbf{r}) = \frac{1}{2}[V_\uparrow(\mathbf{r}) + V_\downarrow(\mathbf{r})]$, which gives rise to a density profile according to

$$n_{\mathrm{S}} = \frac{1}{6\pi^2}\left(\frac{2m}{\xi_{\mathrm{S}}\hbar^2}\right)^{3/2}\left(\mu_{\mathrm{S}}^0 - \frac{1}{2}m\omega^2(x^2+d^2+r_\perp^2)\right)^{3/2}, \tag{6.14}$$

while the densities of the spin-↑ and ↓ components are given by

$$n_{\uparrow\downarrow} = \frac{1}{6\pi^2}\left(\frac{2m}{\hbar^2}\right)^{3/2}\left(\mu_{\uparrow\downarrow}^0 - \frac{1}{2}m\omega^2 r_\perp^2 - \frac{1}{2}m\omega^2(x\mp d)^2\right)^{3/2}. \tag{6.15}$$

For $x > 0$ the border between the superfluid and the spin-up component is derived from the condition $\mu_\downarrow(\mathbf{r})/\mu_\uparrow(\mathbf{r}) = \eta_{\mathrm{c}}$ and yields

$$(x+\alpha d)^2 + r_\perp^2 = (R_\uparrow^0)^2 (R_{\mathrm{S},\uparrow})^2 + \gamma d^2 \tag{6.16}$$

with

$$\begin{aligned} \alpha &= \frac{1+\eta_\mathrm{c}}{1-\eta_\mathrm{c}}, \\ \gamma &= \alpha^2 - 1, \\ (R_\uparrow^0)^2 &= \frac{2\mu_\uparrow^0}{m\omega^2}, \\ (R_{\mathrm{S},\uparrow})^2 &= \frac{2}{m\omega^2}\left(\frac{\mu_\downarrow^0 - \eta_\mathrm{c}\mu_\uparrow^0}{1-\eta_\mathrm{c}}\right). \end{aligned} \tag{6.17}$$

and $\eta_c \sim -0.099$.

For $x < 0$ we have $\mu_\uparrow(\mathbf{r})/\mu_\downarrow(\mathbf{r}) = \eta_\mathrm{c}$, so that the border between the superfluid and the spin-down component is fixed by

$$(x-\alpha d)^2 + r_\perp^2 = (R_\uparrow^0)^2 (R_{\mathrm{S},\downarrow})^2 + \gamma d^2, \tag{6.18}$$

where the only difference to Eq.(6.16) is

$$(R_{\mathrm{S},\downarrow})^2 = \frac{2}{m\omega^2}\left(\frac{\mu_\uparrow^0 - \eta_\mathrm{c}\mu_\downarrow^0}{1-\eta_\mathrm{c}}\right). \tag{6.19}$$

Note, that this boundary emerges only for $d > d_{\mathrm{crit}}$.

In Fig. 6.6 we plot the dipole polarization $D(d)$ as a function the displacement of the traps for different values of the particle imbalance P. The black dashed line corresponds to a noninteracting system ($P = 1$), while the solid black line corresponds to the superfluid Fermi gas ($P = 0$) [120]. The black dots correspond to the critical value of the displacement d_{crit}, and as already mentioned they depend on the imbalance of the system.

The dipole polarizability $D(d)/d$ on the other hand is shown in Fig. 6.7, where again the black dashed line corresponds to the noninteracting system ($P = 1$), while the solid black line stands for the unpolarized superfluid ($P = 0$) as in [120]. Also here we indicate d_{crit} by black dots in the figure.

The behaviour of $D(d)/d$ for $0 < P < 1$ is somehow counterintuitive, since one would expect that for $P \neq 0$ the slope of the dipole polarizability is smaller with respect to the $P = 0$ case, and has a nonzero initial value due to the initial finite particle imbalance.

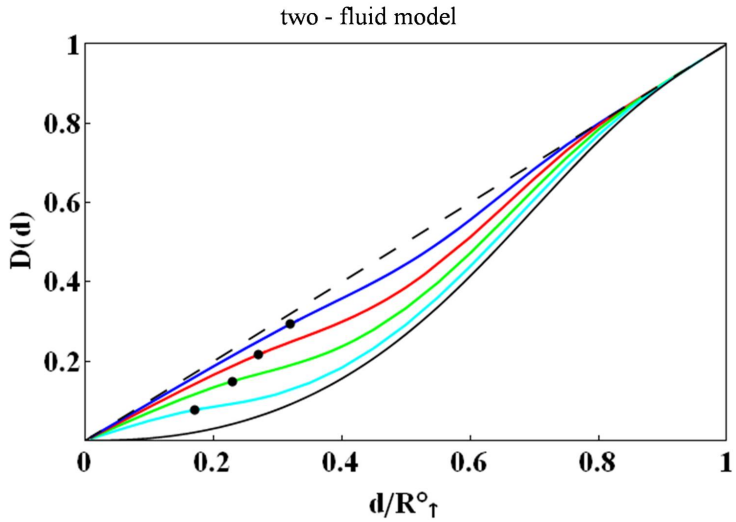

Figure 6.6: Dipole polarization $D(d)$ vs the displacement $d/R^0_\uparrow$ of a polarized Fermi gas in the two-fluid model [56]. The displacement is given in units of the Thomas-Fermi radius $R^0_\uparrow$. $D(d)$ is shown for different values of the polarization: $P = 1$ (black dashed), $P = 0.8$ (blue), $P = 0.6$ (red), $P = 0.4$ (green), $P = 0.2$ (turquoise), and $P = 0$ (black solid). The black dots indicate the critical displacement d_{crit} (see Eq.(6.13)).

We find that the dipole polarizability first decreases until it reaches a minimum (see Fig. 6.7), and then increases until it saturates to the noninteracting value. This can be explained by energetic arguments. The natural and hence energetically favourable configuration of the system for $d = 0$ is a superfluid core centered in the trap, surrounded by a polarized shell. Since the superfluid feels the effective external potential $V^{\mathrm{S}}(\mathbf{r}) = \frac{1}{2}[V_\uparrow(\mathbf{r}) + V_\downarrow(\mathbf{r})]$, the displacement of the traps causes the superfluid to move as a whole, and hence to adopt a higher "unfavourable"energetic level, to which the superfluid is naturally reluctant. The dipole polarizability does not increase until pairs are being broken at the border of the superfluid, which coincides with the onset of a nonvanishing $\downarrow$-particle number.

In Fig. 6.8 we plot the dipole polarizability (black solid), the $\downarrow$- and $\uparrow$ (green long dashed and blue short dashed, respectively), and the superfluid particle number (red short dashed), respectively, for a polarization $P = 0.2$. The minimum of the dipole polarization coincides with the onset of a nonvanishing fraction of $\downarrow$-particles. After this minimum, $D(d)/d$ increases and eventually saturates to the noninteracting value, while the $\downarrow$-particle number saturates. Complementary to this is the evolution of the particle number in the superfluid N_{S}, whose decrease is inversely proportional to the increase of the $\downarrow$-particle number.

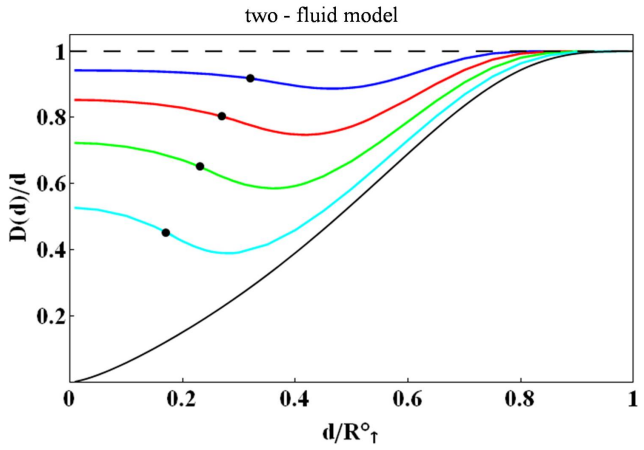

Figure 6.7: Dipole polarizability $D(d)/d$ as a function of the displacement d of a polarized Fermi gas in the two-fluid model [56]. $D(d)/d$ is shown for different values of the polarization: $P = 1$ (black dashed), $P = 0.8$ (blue), $P = 0.6$ (red), $P = 0.4$ (green), $P = 0.2$ (turquoise), and $P = 0$ (black solid).

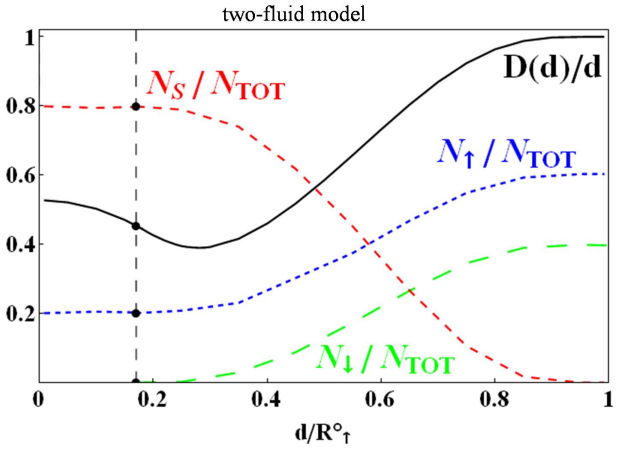

Figure 6.8: The dipole polarizability $D(d)/d$ (black solid), ↓-particle number (green long dashed), ↑-particle number (blue short dashed), and the particle number in the superfluid N_S (red short dashed), respectively, vs d for $P = 0.2$.

6.3 Dipole Polarizability in the Three-Fluid Model

Since we know that the equation of state

$$\frac{E_N(x)}{N_\uparrow} = \frac{3}{5}E_{F\uparrow}\left(1 - Ax + \frac{m}{m^*}x^{5/3} + Bx^2\right) = \frac{3}{5}E_{F\uparrow}g(x) \equiv \epsilon_N(x) \tag{6.20}$$

introduced in [59] agrees very well with the experiments at unitarity carried out so far [46, 63], it is convenient to compare the dipole polarizability obtained for

a system in the two-fluid model with dipole polarizability of a system described with the equation of state Eq.(6.20), the three-fluid model.

The phase diagram for the normal state has been already introduced in chapter 5, and we can use all expressions for the chemical potentials and the transition lines as for a mass ratio $\kappa = 1$. We repeat that to have a superfluid phase the critical concentration needs to be $x_c = 0.44$, corresponding to $(\mu_\downarrow/\mu_\uparrow)\,|_{x_c} \sim 0.0171$, while the transition from the mixed phase to the fully polarized occurs at $x = 0$ where $(\mu_\downarrow/\mu_\uparrow)\,|_{x=0} = -3/5A$.

To study the trapped system, we make again use of Eqs.(6.10), (6.11), and (6.12), with the only difference being that now the LDA line crosses three instead of two phases, namely the superfluid (S), the partially polarized (PP), and the fully polarized (FP) phase as shown in Fig. 6.9.

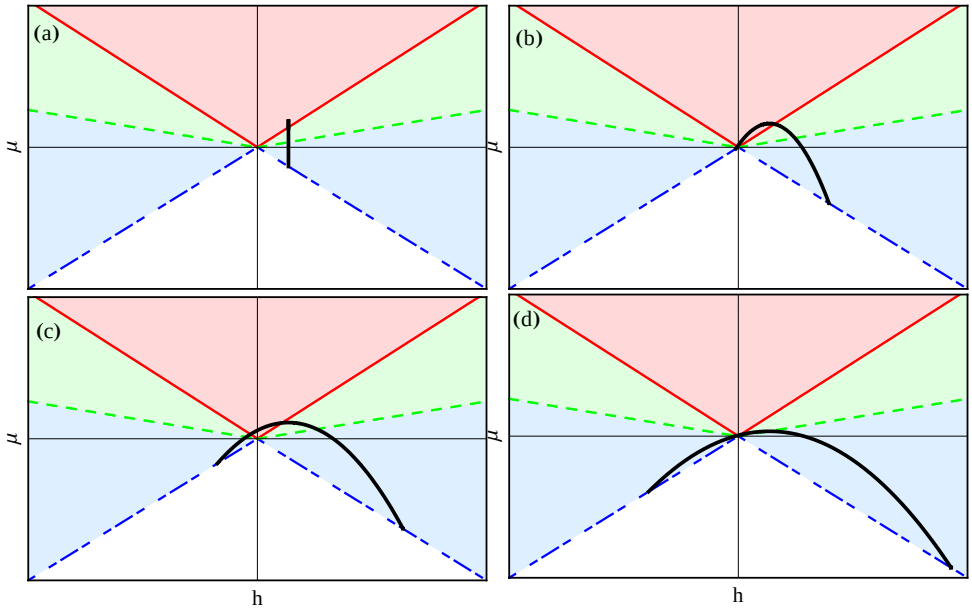

Figure 6.9: μ-h phase diagram of the system in the three-fluid model,where the LDA line (black) is shown for different values of the displacement (a) $d = 0$, (b) $d = d_{\rm crit}$, (c) $d > d_{\rm crit}$, and (d) $d = d_{\rm sep}$ and an arbitrary value of the central imbalance $\eta_0 > \eta_c$.

To explore the $\mu - h$ phase diagram, we set $r_\perp = 0$ in Eq.(6.12), fix the value of η_0 and vary x and d as shown in Fig. 6.9 (a)-(d).

In Fig. 6.10 we show a sketch of the 2D cut of the system in the $x - y$ plane. For $d = 0$ and $\eta_0 > \eta_c$, the system consists of a superfluid core embedded in a mixed shell surrounded by a fully polarized gas (Figs. 6.9 (a) and 6.10 (a)). By changing the value of d, the superfluid and the mixed phase move effectively to the left side, while the fully polarized phase moves effectively to the right. For a critical value $d = d_{\rm crit}$ (Figs. 6.9 (b) and 6.10 (b)), the border of the superfluid

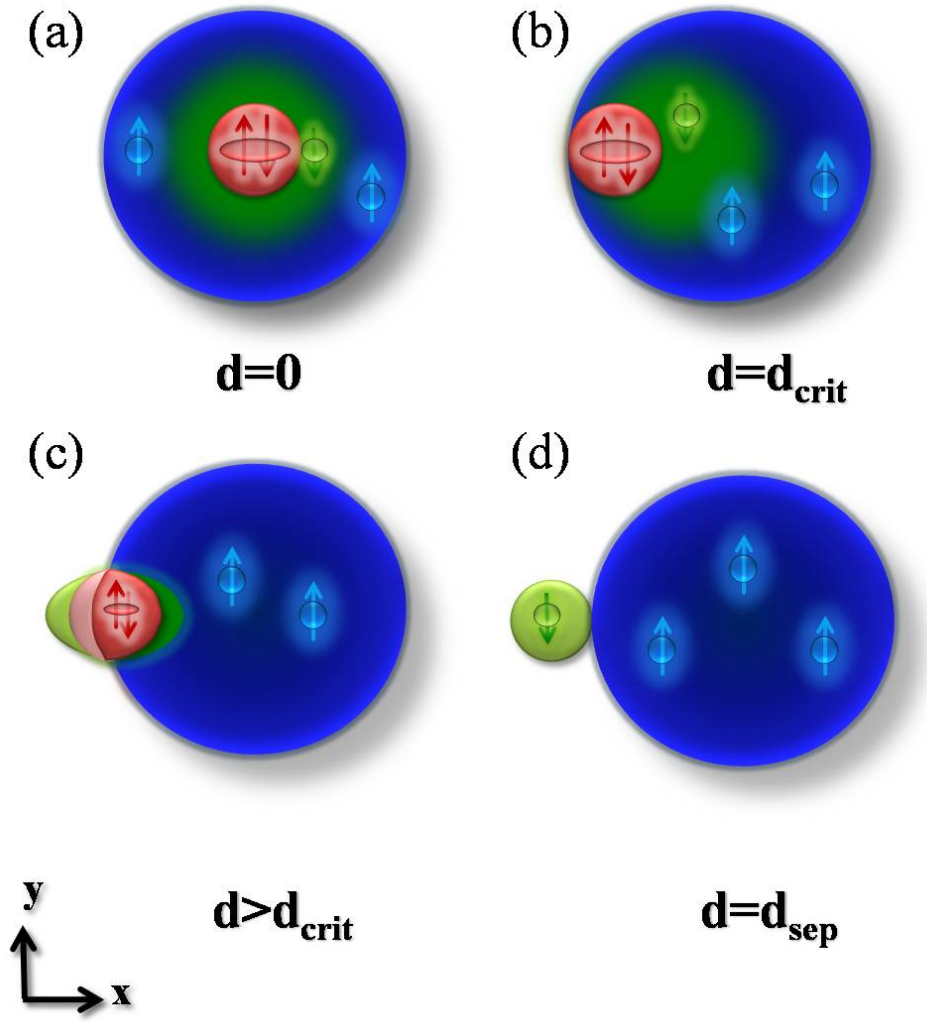

Figure 6.10: Sketch of the four different states of the dipole polarization process in the three-fluid model in a 2D cut: For $d = 0$, the initial configuration is a centered superfluid (red) embedded in a mixed cloud (dark green) with $N_\uparrow > N_\downarrow$, which is surrounded by a polarized spin-$\uparrow$ (blue) corona. For $d \neq 0 < d_{\mathrm{crit}}$, the superfluid and the mixed phase move in the opposite direction with respect to the fully polarized $\uparrow$-cloud. For $d > d_{\mathrm{crit}}$, we start creating a normal phase on the left hand side of the superfluid, where $N_\downarrow > N_\uparrow$ (pink), which eventually touches the fully polarized $\downarrow$-cloud (green). For $d = d_{\mathrm{sep}}$ we have two separate, fully polarized spin-$\uparrow$ and spin-$\downarrow$ clouds.

and of the mixed phase touch, and for $d > d_{\rm crit}$ (Figs. 6.9 (c) and 6.10 (c)) we eventually start to break the pairs in the superfluid as well as in the mixed phase.

Unlike in the two-fluid model, where immediately the ↓-polarized phase is created, here the breaking of pairs leads to an intermediate normal phase with $N_\downarrow > N_\uparrow$, to which the fully ↓-polarized cloud adjoints. This process continues until we have reached the value $d = d_{\rm sep}$, where the superfluid and the mixed phases have completely vanished, and we are left with two entirely separated, fully ↑- and ↓ polarized clouds (Figs. 6.9 and 6.10 (d)). As before, the values $d_{\rm crit}$ and $d_{\rm sep}$ are not universal but show the same dependency on the central balance as given in Eq.(6.13).

6.4 Results

In order to calculate the dipole polarization $D(d)$ and the dipole polarizability $D(d)/d$, we need the expressions for densities of the superfluid, the spin-↑ and spin-↓ components, as well as the borders separating the superfluid from the partially polarized components. The superfluid has a density profile according to

$$n_{\rm S} = \frac{1}{6\pi^2}\left(\frac{2m}{\xi_{\rm S}\hbar^2}\right)^{3/2}\left(\mu_{\rm S}^0 - \frac{1}{2}m\omega^2(x^2+d^2+r_\perp^2)\right)^{3/2}, \tag{6.21}$$

while the densities of the spin-↑ and ↓ components are given by

$$n_\uparrow = \frac{1}{6\pi^2}\left(\frac{2m}{\hbar^2}\right)^{3/2}\left(\frac{\mu_\uparrow^0 - V_\uparrow(\mathbf{r})}{g(x_{\rm c}) - \frac{3}{5}x_{\rm c}g'(x_{\rm c})}\right)^{3/2}, \tag{6.22}$$

$$n_\downarrow = x_{\rm c}\; n_\uparrow, \tag{6.23}$$

where $x_{\rm c}$ is the local critical concentration.

The border between the superfluid and the spin-up component is formally the same as Eqs. (6.16) and (6.18), only that in the three-fluid model the value for η_c is different, $\eta_c = 0.0171$.

In Fig. 6.11 we show the dipole polarization $D(d)$ vs the displacement d for different values of the particle imbalance P. The black dashed line corresponds to a noninteracting system ($P = 1$), while the solid black line corresponds to the superfluid Fermi gas ($P = 0$). The black dots correspond to the critical value of the displacement $d_{\rm crit}$ (see Eq.(6.13)). The behaviour of the dipole polarization is quite similar to the one calculated in the two-fluid model (see also Fig. 6.2), but as expected the three-fluid model has a larger dipole polarizability.

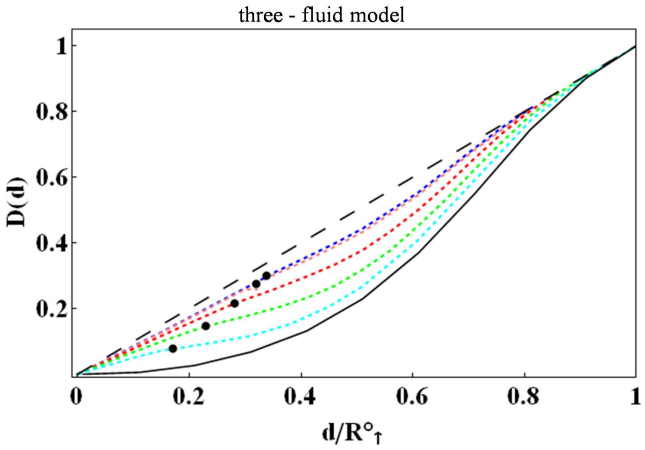

Figure 6.11: Dipole polarization $D(d)$ as a function of the displacement d in the three-fluid model. $D(d)$ is shown for different values of the polarization: $P = 0.8$ (blue dashed), $P = 0.6$ (red dashed), $P = 0.4$ (green dashed), $P = 0.2$ (turquoise dashed), and $P = 0$ (black).

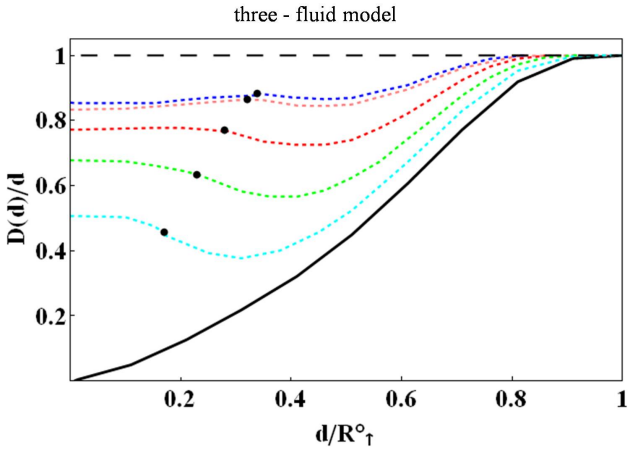

Figure 6.12: Dipole polarizability $D(d)/d$ as a function of the displacement d in the three-fluid model. $D(d)/d$ is shown for different values of the polarization: $P = 0.8$ (blue dashed), $P = P_c$ (pink dashed), $P = 0.6$ (red dashed), $P = 0.4$ (green dashed), $P = 0.2$ (turquoise dashed), and $P = 0$ (black solid).

The same is valid for the dipole polarizability for values of the imbalance $P = 0$, $P = 0.2$, $P = 0.4$, and $P = 0.6$ as can be seen in Fig. 6.12.

The dipole polarizability first decreases until it reaches a minimum, after which it increases again, eventually saturating to the noninteracting value. Also the comparison of the spin-↑, spin-↓, the superfluid particle number and the dipole polarizability for a fixed imbalance (we choose $P = 0.2$) shows practically the same behaviour as in the two-fluid case, only that the ↓ particle number is finite at the beginning due to the presence of the mixed phase (see Fig. 6.13).

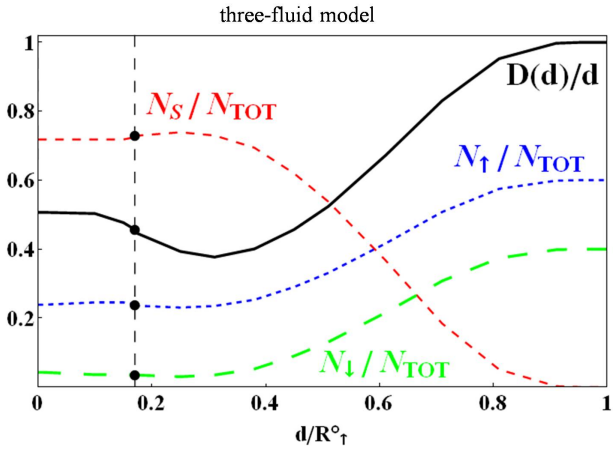

Figure 6.13: The dipole polarizability $D(d)/d$ (black solid), $\downarrow$-particle number (green long dashed), $\uparrow$-particle number (blue short dashed), and particle number in the superfluid (red short dashed), respectively, vs d for $P = 0.2$.

A major difference arises when we consider particle imbalances P above the critical polarization $P_c = 0.77$, represented by the pink ($P = P_c$) and blue line ($P = 0.8$) respectively, in Fig. 6.11. One would expect that since there is no superfluid, the slope of $D(d)/d$ is just linear as for $P = 1$. This however is not the case, as due to the mixed phase a superfluid can be nucleated as a secondary effect of the displacement of the potentials.

Consider the situation of $d = 0$ and the imbalance $P_c = 0.77$, hence only the normal state is present (Fig. 6.14 (a)). As soon as we start changing the value of the displacement $d \neq 0$, the $\downarrow$-particles move to the left side, while the $\uparrow$-particles are displaced effectively to the right side as sketched in Fig. 6.14 (b).

At the border, this causes an increase of the local critical concentration $x_{c,loc}$, so that for $x_{c,loc} \equiv x_c = 0.44$ the conditions to nucleate a superfluid is given (Fig. 6.14 (c)).

In Fig. 6.15 we plot $D(d)/d$, the up- and down particle number and the particle number in the superfluid as a function of the displacement d for the critical imbalance P_c. One can nicely see, that although there is no superfluid at the beginning, $N_S = 0$, the displacement gives rise to the nucleation of a superfluid due to a increase of the local concentration. In this case we expect the density profiles to exhibit some special features. While N_S increases, $N_\downarrow$ and $N_\uparrow$ decrease simultaneously and so does the dipole polarizability. At a certain value of d however, the pairs in the superfluid start being broken, $N_\downarrow$ and $N_\uparrow$ increase, eventually saturating to their initial values.

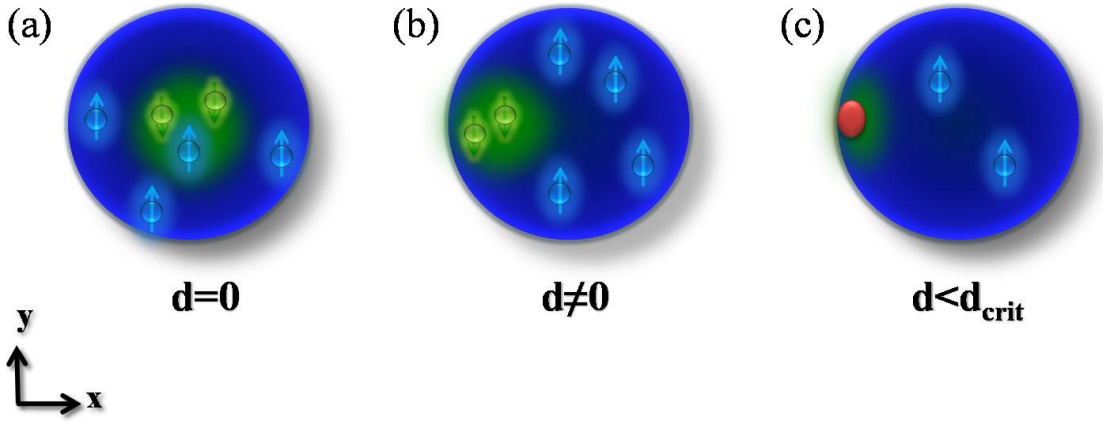

Figure 6.14: Sketch of the effect of displacement for $P \geq P_c$. (a) Initially, the system is fully normal. As soon as the traps are displaced in opposite directions, the $\downarrow$ particles are effectively dragged to the left, while the $\uparrow$ particles are shifted to the right (b). This causes an increase in the local concentration $x_c = n_\downarrow/n_\uparrow$, so that eventually a superfluid is nucleated near the border (c).

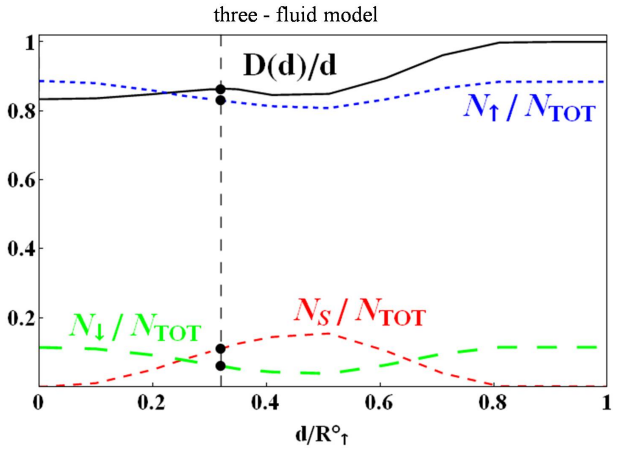

Figure 6.15: The dipole polarizability $D(d)/d$ (black solid), $\downarrow$-particle number (green long dashed), $\uparrow$-particle number (blue short dashed), and particle number in the superfluid (red short dashed), respectively, vs d for $P = P_c = 0.77$.

6.5 Conclusions

We have analyzed a dipole configuration in the two-fluid and in the three-fluid model for various particle imbalances P. We find that the inclusion of the partially polarized phase does not alter significantly the results obtained in the two-fluid model for imbalances $P < P_c$. For $0 < P < P_c$, the dipole polarizability exhibits a minimum due to the presence of the superfluid core. The superfluid prefers to be at the center of the trap and is reluctant to me moved out of it.

Hence more energy is needed to dipole polarize the configuration.

The major difference occurs in the three-fluid model for polarizations larger than P_c. There, a superfluid can be created also for values $P \geq 0.77$ by the displacement of the traps, which gives rise to an increase in the local value of the local concentration.

We have assumed that the external potential can be tuned separately, so that spin-dependent trapping potentials can be engineered. In mixtures of same atomic species in different hyperfine levels this could be done by profiting of the different polarization of the electronic spin [121]. Experimentally, the separate tuning of the trapping potentials should be easier if the system mixtures consists of different atomic species, e.g. ^{6}Li and ^{40}K. As we have shown in chapter 5 such mixtures with a mass ratio of, e.g., $\kappa = 6.7$ can moreover give rise to a sandwiched superfluid configuration in the trap, and it would be interesting to study the static response of these exotic configurations to a spin-dependent external field.

7 Summary

In this thesis we have analyzed the behaviour of unitary Fermi gases at zero temperature in engineered external confinements and consisting of different atomic species. Since we have provided a detailed discussion of our results at the end of each chapter, we will conclude the thesis with a concise summary of our major findings.

We have first analyzed the effect of adiabatic rotation on a polarized Fermi gas. We find that the normal phase is energetically favoured by the rotation in the rotating frame, and thus the superfluid is further depleted with respect to the nonrotating configuration. The normal region exhibits the typical bulge effect due to the centrifugal force, while the superfluid is squeezed due to the depletion of the superfluid density in the plane of rotation. This has clear observable effects on the density profiles which can be addressed experimentally. A striking feature is that although the global polarization is not affected by the rotation, the concentration $n_\downarrow/n_\uparrow$ at the border increases from the non-rotating value on the z-axis to a maximum value in the xy-plane.

A special case of the system discussed above is the unpolarized Fermi superfluid. While at small angular velocities the superfluid is unaffected by the rotation of the trap, at higher angular velocities the rotation results in a phase separation between a non rotating superfluid core and a rigidly rotating normal component due to pair breaking near the border of the cloud. The realization of the phase separation would open the unique possibility of exploring the Fermi liquid behaviour of a strongly interacting gas at zero temperature. Important effects to investigate are, for example, the zero sound nature of the collective oscillations and the behaviour of viscosity.

Concerning the rotating configuration we have also addressed the question of quadrupole instability of the superfluid core, which produces a spontaneous breaking of axial symmetry of the cloud. The critical frequency for the onset of the instability turns out to be smaller than in the BEC case. Its measurement would provide a further crucial test of the mechanism of phase separation and of the equation of state of the normal phase.

We have studied the unitary Fermi gas consisting of two different atomic species,

assuming phase separation between an unpolarized superfluid and a polarized normal phase. The latter is described by an equation of state which, unlike in the BCS mean-field treatment, takes into account the effect of the strong interaction at unitarity. As we have shown, in a homogeneous system this has a dramatic impact on the results such as the Chandrasekhar-Clogston limit needed to start nucleating a superfluid. Using the local density approximation we have determined how the trapped configuration depends on the trapping potential, the mass ratio, and the polarization. Many different configurations are possible. Among them it is worth mentioning the three-shell configuration, where the superfluid is sandwiched between a "heavy"normal phase at the center and a "light"normal phase towards the edges of the trap. We can also have non-trivial configurations even if one of the two components is not trapped, but still remains confined due to the interaction induced trapping. This interaction-induced trapping is not possible within the BCS theory since interactions are absent in the normal phase.

At last we have addressed the problem of dipole polarizability by relative trapping displacement in the two- and three-fluid model for various particle imbalances P. We find that the inclusion of the partially polarized phase does not alter significantly the results obtained in the two-fluid model for imbalances $P < P_c$. The major difference occurs in the three-fluid model for polarizations larger than P_c, where a superfluid is created by the displacement of the traps, which locally increases the concentration.

8 Acknowledgements

I have the honor to thank Sandro Stringari for giving me the unique opportunity of doing my PhD in his group. I am grateful for his guidance not only concerning physics, but also from the human point of view, during my time as his PhD student.

I am much indebted to my second supervisor Alessio Recati, who introduced me to the Trento group in the first place. He unfailingly answered all my questions, anytime, and patiently helped me whenever I needed advice. I would like to thank him also for his guidance and support, not only as my supervisor, but also as a friend.

During my PhD Prof. Wilhelm Zwerger gave me the wonderful opportunity to work for several months in his group in Munich, where part of my work was done, and I want to thank him for his generous hospitality as well as Daniela Neufang for organizing my stay.

I want to thank Iacopo Carusotto, Franco Dalfovo, and Stefano Giorgini for reading parts of my thesis and making lots of useful suggestions. I am grateful to them as well as to Carlos Lobo, Francesco Piazza, Sebastiano Pilati, Lev Pitaevskii and Alberto Valli for fruitful discussions and ideas in the run of my PhD.

My stay in Trento was not only a wonderful experience and a pleasure because I could work on what I like and collaborate with great physicists, but also because of the friendly atmosphere and the great people I was allowed to make friends with. I owe a very big hug to Beatrice, without whom life in Trento would have been definitely less exciting, and also to Augusto, Chiara, Davide, Ed, Francesco Bariani, Franceso Piazza, Gentaro, Gianluca, Jan, Marco, Philipp, and Sebastiano for numerous dinners. Special thanks go to Luisa Rossi Doria, the mother of all PhD students.

Finally, I want to thank both my partner Daniel for always being there for me, his understanding and tireless encouragement, and my parents for their continuous support throughout the last years and for giving me the possibility to do what I like.

Bibliography

[1] M. H. Anderson, J. R. Ensher, M. R. Matthews, C. E. Wiemann, and E. A. Cornell, *Observation of Bose-Einstein Condensation in a Dilute Atomic Vapor*, Science **269**, 198 (1995).

[2] C. C. Bradley, C. A. Sackett, J. J. Tollett, and R. G. Hulet, *Evidence of Bose-Einstein Condensation in an Atomic Gas with Attractive Interactions*, Physical Review Letters **75**, 1687 (1995).

[3] K. B. Davis, M.-O. Mewes, M. R. Andrews, N. J. van Druten, D. S. Durfee, D. M. Stamper-Kurn, and W. Ketterle, *Bose-Einstein Condensation in a Gas of Sodium Atoms*, Physical Review Letters **75**, 3969 (1995).

[4] W. Ketterle, *Bose-Einstein Condensation.* For the 9th Edition of the McGraw-Hill Encyclopedia of Science & Technology. (2002), For the 9th Edition of the McGraw-Hill Encyclopedia of Science & Technology.

[5] M. Greiner, C. A. Regal, and D. S. Jin, *Emergence of a molecular Bose-Einstein condensate from a Fermi gas*, Nature **426**, 537 (2003).

[6] M. Greiner, C. A. Regal, and D. S. Jin, *Fermi Condensates*, Proceedings of ICAP-2004, Rio de Janeiro (2005).

[7] H. Feshbach, *A Unified Theory of Nuclear Reactions*, Annals of Physics **5**, 357 (1958).

[8] H. Feshbach, *A Unified Theory of Nuclear Reactions II*, Annals of Physics **19**, 287 (1962).

[9] U. Fano, *Resonant Configuration Interaction*, Physical Review **124**, 1866 (1961).

[10] F. Dalfovo, S. Giorgini, L. P. Pitaevskii, and S. Stringari, *Theory of Bose-Einstein condensation in trapped gases*, Review of Modern Physics **71**, 463 (1999).

[11] S. Stringari and L. P. Pitaevskii, *Bose-Einstein Condensation* (International Series of Monographs on Physics Vol. 116, Oxford University Press, 2003).

[12] C. J. Pethick and H. Smith, *Bose-Einstein Condensation in Dilute Gases* (Cambridge University Press, 2008).

[13] M. Inguscio, S. Stringari, and C. E. Wiemann, eds., *Bose-Einstein Condensation in Atomic Gases*, Proceedings of the International School of Physics "Enrico Fermi", Course CXL, Varenna, July 7 - 17 1998 (IOS Amsterdam, 1999).

[14] M. R. Matthews, B. P. Anderson, P. C. Haljan, D. S. Hall, C. E. Wiemann, and E. A. Cornell, *Vortices in a Bose-Einstein Condensate*, Physical Review Letters **83**, 2498 (1999).

[15] K. W. Madison, F. Chevy, W. Wohlleben, and J. Dalibard, *Vortex Formation in a Stirred Bose-Einstein Condensate*, Physical Review Letters **84**, 806 (2000).

[16] J. R. Abo-Shaeer, C. Raman, J. M. Vogels, and W. Ketterle, *Observation of Vortex Lattices in Bose-Einstein Condensates*, Science **292**, 476 (2001).

[17] D. S. Jin, J. R. Ensher, M. R. Matthews, C. E. Wiemann, and E. A. Cornell, *Collective Excitations of a Bose-Einstein Condensate in a Dilute Gas*, Physical Review Letters **77**, 420 (1996).

[18] M.-O. Mewes, M. R. Andrews, N. J. van Druten, D. M. Stamper-Kurn, D. S. Durfee, C. G. Townsend, and W. Ketterle, *Collective Excitations of a Bose-Einstein Condensate in a Magnetic Trap*, Physical Review Letters **77**, 988 (1996).

[19] F. S. Cataliotti, S. Burger, C. Fort, P. Maddaloni, F. Minardi, A. Trombettoni, A. Smerzi, and M. Inguscio, *Josephson Junction Arrays with Bose-Einstein Condensates*, Science **293**, 843 (2001).

[20] M. Albiez, M. R. Gati, J. Fölling, S. Hunsmann, M. Cristiani, and M. K. Oberthaler, *Direct Observation of Tunneling and Nonlinear Self-Trapping in a Single Bosonic Josephson Junction*, Physical Review Letters **95**, 010402 (2005).

[21] M. H. Andrews, C. G. Townsend, H.-J. Miesner, D. S. Durfee, D. M. Stamper-Kurn, and W. Ketterle, *Observation of Interference Between Two Bose Condensates*, Science **275**, 637 (1997).

[22] M. Greiner, O. Mandel, T. Esslinger, T. W. Hänsch, and I. Bloch, *Quantum phase transition from a superfluid to a Mott insulator in a gas of ultracold atoms*, Nature **415**, 39 (2002).

[23] B. De Marco and D. S. Jin, *Onset of Fermi Degeneracy in a Trapped Atomic Gas*, Science **285**, 1703 (1999).

[24] L. D. Landau and E. M. Lifshitz, *Quantum Mechanics* (Pergamon, Oxford, 1987).

[25] I. Bloch, J. Dalibard, and W. Zwerger, *Many-body physics with ultracold gases*, Review of Modern Physics **80**, 885 (2008).

[26] S. Giorgini, L. P. Pitaevskii, and S. Stringari, *Theory of ultracold atomic Fermi gases*, Review of Modern Physics **80**, 1215 (2008).

[27] I. Bloch, *Ultracold quantum gases in optical lattices*, Nature Physics **1**, 23 (2005).

[28] M. Köhl, H. Moritz, T. Stöferle, K. Günter, and T. Esslinger, *Fermionic Atoms in a Three Dimensional Optical Lattice: Observing Fermi Surfaces, Dynamics, and Interactions*, Applied Physics Letters **94**, 080403 (2005).

[29] F. Bloch, *Über die Quantenmechanik der Elektronen in Kristallgittern*, Zeitschrift für Physik A **52**, 555 (1928).

[30] G. Roati, E. de Mirandes, F. Ferlaino, H. Ott, G. Mondungno, and M. Inguscio, *Atom Interferometry with Trapped Fermi Gases*, Applied Physics Letters **92**, 230402 (2004).

[31] S. Inouye, M. R. Andrews, J. Stenger, H.-J. Miesner, D. M. Stamper-Kurn, and W. Ketterle, *Observation of Feshbach resonances in a Bose-Einstein condensate*, Nature **392**, 151 (1998).

[32] J. Hubbard, *Electron Correlations in Narrow Energy Bands*, Proceedings of the Royal Society A **276**, 238 (1963).

[33] W. Hofstetter, J. I. Cirac, P. Zoller, E. Demler, and M. D. Lukin, *High-temperature superfluidity of fermionic systems in optical lattices*, Applied Physics Letters **89**, 220407 (2002).

[34] J. K. Chin, D. E. Miller, Y. Kiu, C. Stan, W. Setiawan, C. Sanner, K. Xu, and W. Ketterle, *Evidence for superfluidity of ultracold fermions in an optical lattice*, Nature **443**, 961 (2006).

[35] R. Jördens, N. Strohmaier, K. Günter, H. Moritz, and T. Esslinger, *A Mott insulator of fermionic atoms in an optical lattice*, Nature **455**, 204 (2008).

[36] N. F. Mott, *Metal-Insulator Transition*, Reviews of Modern Physics **40**, 677 (1968).

[37] S. Jochim, M. Bartenstein, A. Altmeyer, G. Hendl, C. Chin, J. Hecker-Denschlag, and R. Grimm, *Bose-Einstein Condensation of Molecules*, Science **302**, 2101 (2003).

[38] M. W. Zwierlein, C. A. Stan, C. H. Schunk, S. M. F. Raupach, S. Gupta, Z. Hadzibabic, and W. Ketterle, *Observation of Bose-Einstein Condensation of Molecules*, Physical Review Letters **91**, 250401 (2003).

[39] T. Bourdel, L. Khaykovich, J. Cubizolles, J. Zhang, F. Chevy, M. Teichmann, L. Tarruell, S. J. J. M. F. Kokkelmans, and C. Salomon, *Experimental Study of the BEC-BCS Crossover Region in Lithium 6*, Physical Review Letters **93**, 050401 (2004).

[40] G. B. Partidge, K. E. Stecker, R. I. Kamar, M. W. Jack, and R. G. Hulet, *Molecular Probe of Pairing in the BEC-BCS Crossover*, Physical Review Letters **95**, 020404 (2005).

[41] J. Bardeen, L. N. Cooper, and J. R. Schrieffer, *Theory of Superconductivity*, Physical Review **108**, 1175 (1957).

[42] L. N. Cooper, *Bound electron pairs in a degenerate Fermi gas*, Physical Review **104**, 1189 (1956).

[43] L. Onsager, *Statistical Hydrodynamics*, Il Nuovo Cimento, Supp. 2 **6**, 249 (1949).

[44] R. P. Feynman, *Application of quantum mechanics to liquid helium*, Progress in Low Temperature Physics **1**, 17 (1955).

[45] M. W. Zwierlein, J. R. Abo-Shaeer, A. Schirotzek, C. H. Schunck, and W. Ketterle, *Vortices and superfluidity in a strongly interacting Fermi gas*, Nature **435**, 1047 (2005).

[46] Y. Shin, M. W. Zwierlein, C. H. Schunk, A. Schirotzek, and W. Ketterle, *Observation of Phase Separation in a Strongly Interacting Imbalanced Fermi Gas*, Physical Review Letters **97**, 030401 (2006).

[47] G. B. Partridge, W. Li, R. I. Kamar, Y. A. Liao, and R. G. Hulet, *Pairing and Phase Separation in a Polarized Fermi Gas*, Science **311**, 503 (2006).

[48] G. B. Partridge, W. Li, Y. A. Liao, R. G. Hulet, M. Haque, and H. T. C. Stoof, *Deformation of a Trapped Fermi Gas with Unequal Spin Populations*, Physical Review Letters **97**, 190407 (2006).

[49] M. W. Zwierlein, A. Schirotzek, C. H. Schunck, and W. Ketterle, *Fermionic Superfluidity with Imbalanced Spin Populations*, Science **311**, 492 (2006).

[50] M. W. Zwierlein, C. H. Schuck, A. Schirotzek, and W. Ketterle, *Direct Observation of the Superfluid Phase Transition in Ultracold Fermi Gases*, Nature **442**, 54 (2006).

[51] A. M. Clogston, *Upper Limit for the Critical Field in Hard Superconductors*, Physical Review Letters **9**, 266 (1962).

[52] B. S. Chandrasekhar, *A note on the maximum critical field of high-field superconductors*, Applied Physics Letters **1**, 7 (1962).

[53] D. M. Eagles, *Possible Pairing without Superconductivity at Low Carrier Concentrations in Bulk and Thin-Film Superconducting Semiconductor*, Physical Review **186**, 456 (1969).

[54] A. Leggett, In *Modern Trends in the Theory of Condensed Matter,* edited by A. Pekalski and J. Przystawa (Springer, Berlin, 1980).

[55] D. S. Petrov, C. Salomon, and G. V. Shlyapnikov, *Weakly Bound Dimers of Fermionic Atoms*, Physical Review Letters **93**, 090404 (2004).

[56] F. Chevy, *Universal phase diagram of a strongly interacting Fermi gas with unbalanced spin populations*, Physical Review A **74**, 063628 (2006).

[57] T. N. De Silva and E. J. Mueller, *Profiles of near-resonant population-imbalanced trapped Fermi gases*, Physical Review A **73**, 051602 (2006).

[58] M. Haque and H. T. C. Stoof, *Pairing of a trapped resonantly interacting fermion mixture with unequal spin populations*, Physical Review A **74**, 011602 (2006).

[59] C. Lobo, A. Recati, S. Giorgini, and S. Stringari, *Normal State of a Polarized Fermi Gas at Unitarity*, Physical Review Letters **97**, 200403 (2006).

[60] A. Recati, C. Lobo, and S. Stringari, *Role of interactions in spin-polarized atomic Fermi gases at unitarity*, Physical Review A **78**, 023633 (2008).

[61] A. Bulgac and M. McNeil Forbes, *Unitary Fermi Supersolid: The Larkin-Ovchinnikov Phase*, Physical Review Letters **101**, 215301 (2008).

[62] F. Chevy, *Density Profile of a Trapped Strongly Interacting Fermi Gas with Unbalanced Spin Populations*, Physical Review Letters **96**, 130401 (2006).

[63] Y. Shin, C. H. Schunck, A. Schirotzek, and W. Ketterle, *Phase diagram of a two-component Fermi gas with resonant interactions*, Nature **451**, 689 (2008).

[64] C. H. Schunck, Y. Shin, A. Schirotzek, M. W. Zwierlein, and W. Ketterle, *Pairing Without Superfluidity: The Ground State of an Imbalanced Fermi Mixture*, Science **316**, 867 (2007).

[65] S. Pilati and S. Giorgini, *Phase Separation in a Polarized Fermi Gas at Zero Temperature*, Physical Review Letters **100**, 030401 (2008).

[66] E. Wille, F. M. Spiegelhalder, G. Kerner, D. Naik, A. Trenkwalder, G. Hendl, F. Schreck, R. Grimm, T. G. Tiecke, J. T. M. Walraven, *et al.*, *Exploring an Ultracold Fermi-Fermi Mixture: Interspecies Feshbach Resonances and Scattering Properties of ^6Li and ^{40}K*, Physical Review Letters **100**, 053201 (2008).

[67] M. Taglieber, A.-C. Voigt, T. Aoki, T. W. Hänsch, and K. Dieckmann, *Quantum degenerate Two-Species Fermi-Fermi Mixture Coexisting with a Bose-Einstein Condensate*, Physical Review Letters **100**, 010401 (2009).

[68] M. G. Alford, A. Schmitt, K. Rajagopal, and T. Schäfer, *Color superconductivity in dense quark matter*, Reviews of Modern Physics **80**, 1455 (2008).

[69] R. Casalbuoni and G. Nardulli, *Inhomogenous superconductivity in condensed matter and QCD*, Review of Modern Physics **76**, 263 (2004).

[70] M. Iskin and C. J. Williams, *Trapped fermion mixtures with unequal masses: a Bogoliubov-de Gennes approach*, arXiv:0810.5065 (2008).

[71] P. F. Bedaque, H. Caldas, and G. Rupak, *Phase Separation in Asymmetrical Fermion Superfluids*, Physical Review Letters **91**, 247002 (2003).

[72] S.-T. Wu, C.-H. Pao, and S.-K. Yip, *Resonant pairing between fermions with unequal masses*, Physical Review B **74**, 224504 (2006).

[73] C.-H. Pao, S.-T. Wu, and S.-K. Yip, *Asymmetric Fermi superfluid with different atomic species in a harmonic trap*, Physical Review A **76**, 053621 (2007).

[74] G.-D. Lin, W. Yi, and L.-M. Duan, *Superfluid shells for trapped fermions with mass and population imbalance*, Physical Review A **74**, 031604(R) (2006).

[75] M. M. Parish, F. M. Marchetti, A. Lamacraft, and B. D. Simons, *Polarized Fermi Condensates with Unequal Masses: Tuning the Tricritical Point*, Physical Review Letters **98**, 160402 (2007).

[76] M. Iskin and C. A. R. Sá de Melo, *Two-Species Fermion Mixtures with Population Imbalance*, Physical Review Letters **97**, 100404 (2006).

[77] M. Iskin and C. A. R. Sá de Melo, *Mixtures of ultracold fermions with unequal masses*, Physical Review A **76**, 013601 (2007).

[78] A. Gezerlis, S. Gandolfi, K. E. Schmidt, and J. Carlson, *Heavy-Light Fermion Mixtures at Unitarity*, Physical Review Letters **103**, 060403 (2009).

[79] I. Bausmerth, A. Recati, and S. Stringari, *Destroying Superfluidity by Rotating a Fermi Gas at Unitarity*, Physical Review Letters **100**, 070401 (2008).

[80] I. Bausmerth, A. Recati, and S. Stringari, *Unitary polarized Fermi gas under adiabatic rotation*, Physical Review A **78**, 063603 (2008).

[81] M. W. Zwierlein and W. Ketterle, *Making, probing and understanding ultracold Fermi gases*, Proceedings of the International School of Physics "Enrico Fermi", Course CLXIV, Varenna, June 20 - 30 2006, eds. M. Inguscio, W. Ketterle, and C. Salomon (IOS, Amsterdam, 2008).

[82] G. E. Astracharchik, J. Boronat, J. Casulleras, and S. Giorgini, *Equation of State of a Fermi Gas in the BEC-BCS Crossover: A Quantum Monte Carlo Study*, Physical Review Letters **93**, 200404 (2004).

[83] J. Carlson, S.-Y. Chang, V. R. Pandharipande, and K. E. Schmidt, *Superfluid Fermi Gases with Large Scattering Length*, Physical Review Letters **91**, 050401 (2003).

[84] L. Landau, Physikalische Zeitschrift der Sowjetunion **3**, 644 (1933).

[85] J. Kondo, *Resistance Minimum in Dilute Magnetic Alloys*, Progress of Theoretical Physics **32**, 37 (1964).

[86] A. Schirotzek, C.-H. Wu, A. Sommer, and M. W. Zwierlein, *Observation of Fermi Polarons in a Tunable Fermi Liquid of Ultracold Atoms*, Applied Physics Letters **102**, 230402 (2009).

[87] S. Nascimbène, N. Navon, K. J. Jiang, L. Tarruell, M. Teichmann, J. McKeever, F. Chevy, and C. Salomon, *Collective Oscillations of an Imbalanced Fermi Gas: Axial Compression Modes and the Polaron Effective Mass*, arXiv:0907.3032v1 (2009).

[88] R. Combescot, A. Recati, C. Lobo, and F. Chevy, *Normal State of Highly Polarized Fermi Gases: Simple Many-Body Approaches*, Physical Review Letters **98**, 180402 (2007).

[89] R. Combescot and S. Giraud, *Normal State of Highly Polarized Fermi Gases: Full Many-Body Treatment*, Physical Review Letters **101**, 050404 (2008).

[90] N. Prokof'ev and B. Svistunov, *Fermi-polaron problem: Diagrammatic Monte Carlo method for divergent sign-alternating series*, Physical Review B **77**, 020408(R) (2008).

[91] A. Bulgac and M. McNeil Forbes, *Zero-temperature thermodynamics of asymmetric Fermi gases at unitarity*, Physical Review A **75**, 031605(R) (2007).

[92] Y. Shin, *Determination of the equation of state of a polarized Fermi gas at unitarity*, Physical Review A **77**, 041603(R) (2008).

[93] H. E. Hall, *The rotation of liquid helium II*, Advances in Physics **9**, 89 (1960).

[94] R. J. Donnelly, *Quantized Vortices in Helium II* (Cambridge University Press, 1991).

[95] D. M. Brink and Broglia, *Nuclear Superfluidity: Pairing in Finite Systems* (Cambridge University Press, 2005).

[96] M. Antezza, M. Cozzini, and S. Stringari, *Breathing modes of a fast rotating Fermi gas*, Physical Review A **75**, 053609 (2007).

[97] H. Zhai and T.-L. Ho, *Critical rotational Frequency for Superfluid Fermionic Gases across a Feshbach Resonance*, Physical Review Letters **97**, 180414 (2006).

[98] G. Moller and N. R. Cooper, *Density Waves and Supersolidity in Rapidly Rotating Atomic Fermi Gases*, Physical Review Letters **99**, 190409 (2007).

[99] A. Recati, F. Zambelli, and S. Stringari, *Overcritical Rotation of a Trapped Bose-Einstein Condensate*, Physical Review Letters **86**, 377 (2001).

[100] S. Sinha and Y. Castin, *Dynamic Instability of a Rotating Bose-Einstein Condensate*, Physical Review Letters **87**, 190402 (2001).

[101] K. W. Madison, F. Chevy, V. Bretin, and J. Dalibard, *Stationary States of a Rotating Bose-Einstein Condensate: Routes to Vortex Nucleation*, Physical Review Letters **86**, 4443 (2001).

[102] M. Urban and P. Schuck, *Pair breaking in rotating Fermi gases*, Physical Review A **78**, 011601(R) (2008).

[103] F. Dalfovo, C. Minniti, and L. P. Pitaevskii, *Frequency shift and mode coupling in the nonlinear dynamics of a Bose-condensed gas*, Physical Review A **56**, 4855 (1997).

[104] F. Chevy, K. W. Madison, and J. Dalibard, *Measurement of the Angular Momentum of a Rotating Bose-Einstein Condensate*, Physical Review Letters **85**, 2223 (2000).

[105] M. Cozzini and S. Stringari, *Fermi Gases in Slowly Rotating Traps: Superfluid versus Collisional Hydrodynamics*, Physical Review Letters **91**, 070401 (2003).

[106] P. G. de Gennes, *Superconductivity of metals and alloys* (Westview Press, 1999).

[107] M. Iskin and E. Tiesinga, *Rotation-induced superfluid-normal phase separation in trapped Fermi gases*, Physical Review A **79**, 053621 (2009).

[108] P. Rosenbusch, D. S. Petrov, S. Sinha, F. Chevy, V. Bretin, Y. Castin, G. V. Shlyapnikov, and J. Dalibard, *Critical Rotation of a Harmonically Trapped Bose Gas*, Physical Review Letters **88**, 250403 (2002).

[109] F. Dalfovo and S. Stringari, *Shape deformations and angular-momentum transfer in trapped Bose-Einstein condensates*, Physical Review A **63**, 011601(R) (2001).

[110] G. Tonini, F. Werner, and Y. Castin, *Formation of a vortex lattice in a rotating BCS Fermi gas*, European Journal of Physics D **39**, 283 (2006).

[111] M. Abramowitz and I. A. Stegun, *Handbook of Mathematical Functions with Formulas, Graphs, and Mathematical Tables* (Dover, New York, 1965).

[112] L. D. Landau and E. M. Lifshitz, *Fluid Mechanics* (Butterworth-Heinemann, 2000).

[113] I. Bausmerth, A. Recati, and S. Stringari, *Chandrasekhar-Clogston limit and phase separtion in Fermi gases at unitarity*, Physical Review A **79**, 043622 (2009).

[114] D. S. Petrov, C. Salomon, and G. V. Shlyapnikov, *Diatomic molecules in ultracold Fermi gases - novel composite bosons*, Journal of Physics B: Atomic, Molecular and Optical Physics **38**, 645 (2005).

[115] G. E. Astracharchik, D. Blume and S. Giorgini, private communication. For a trapped system with equal oscillator lenghts the parameter ξ_S has been estimated for different mass ratios κ by J. von Stecher *et al.*, Physical Review A **76**, 053613 (2007).

[116] Current project of the Ultracold Atoms and Quantum Gases Group of the University of Innsbruck.

[117] G. Orso, L. P. Pitaevskii, and S. Stringari, *Equilibrium and dynamics of a trapped superfluid Fermi gas with unequal masses*, Physical Review A **77**, 033611 (2008).

[118] J. Carlson and S. Reddy, *Asymmetric Two-Component Fermion Systems in Strong Coupling*, Physical Review Letters **95**, 060401 (2005).

[119] M. A. Baranov, C. Lobo, and G. V. Shlyapnikov, *Superfluid pairing between fermions with unequal masses*, Physical Review A **78**, 033620 (2008).

[120] A. Recati, I. Carusotto, C. Lobo, and S. Stringari, *Dipole Polarizability of a Trapped Superfluid Fermi Gas*, Physical Review Letters **97**, 190403 (2006).

[121] I. Carusotto, *Bragg scattering and the spin structure factor of two-component atomic gases*, Journal of Physics B **39**, S211 (2006).